LIGHT TRAPPING IN THE POLYMER FRONT SHEET OF SOLARGE LIGHT-WEIGHT PHOTOVOLTAIC MODULES

SATHYA SHANKA VASUKI

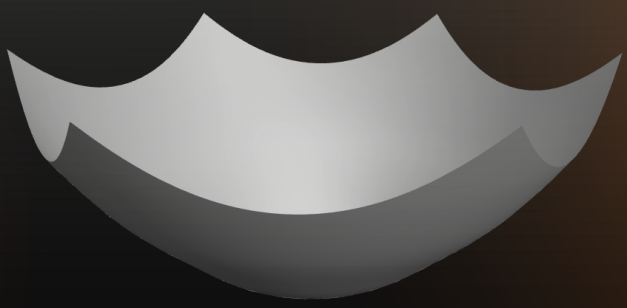

Light trapping in the polymer front sheet of solarge light-weight photovoltaic modules

Sathya Shanka Vasuki

Light trapping in the polymer front sheet of solarge light-weight photovoltaic modules

DISSERTATION

To obtain
the degree of Master of Science in,
Sustainable Energy Technology,
at the Delft University of Technology (TU Delft),
to be publicly defended
on Tuesday 25 July 2023 at 10:30 hours

by

Sathya Shanka Vasuki

Master of Science in Sustainable Energy Technology,
Technische Universiteit Delft, The Netherlands,
born on the 23rd of November, 1997
in Bangalore, Karnataka, India

This thesis has been approved by the

Supervisor
Dr. ir. Rudi Santbergen

Co-Supervisor
Lukáš Šimurka
Menno Van Den Donker

Composition of the graduation committee:

Prof. Dr. ir. Ivan Gordon,	Full professor Photovoltaic Materials and Devices group (PVMD), Technische Universiteit Delft
Dr. ir. Jianning Dong,	Assistant professor DCES/ESE, Technische Universiteit Delft
Dr. ir. Rudi Santbergen,	Assistant professor and supervisor ESE - PVMD Technische Universiteit Delft
Dr. ir. Lukáš Šimurka,	Research Project Manager and Co-supervisor Solarge
Dr. ir. Menno Van Den Donker,	R & D Manager and Co-supervisor Solarge

TU Delft Delft University of Technology

solarge

PVMD Delft University of Technology

कर्मण्येवाधिकारस्ते मा फलेषु कदाचन।
मा कर्मफलहेतुर्भूर्मा ते सङ्गोऽस्त्वकर्मणि॥

"Your right is to perform your duties only, but never to expect the fruits thereof. Do not let the fruit of your actions be the motive, nor be attached to inaction."
Bhagavad Gita

Contents

1

Introduction

Light management plays a crucial role in the field of photovoltaics. This chapter begins by providing a historical background of photovoltaics, highlighting its importance in the current global energy landscape. The significance of light trapping technology is discussed, providing a foundation for the concepts and theories explored in this thesis.

A thorough literature review is presented, encompassing the latest developments in light trapping techniques. This review serves as an overview of the advancements in the field, setting the stage for the subsequent chapters.

The chapter concludes by formulating the objectives and goals of the thesis, outlining the specific research questions that will be addressed. This roadmap provides a clear structure for the subsequent chapters, guiding the reader through the analysis and findings of the research.

Overall, this chapter serves as an introduction to the topic of light management in photovoltaics, establishing the context and setting the stage for the in-depth exploration that follows.

1

1.1 Origin of Photovoltaics

For 4.603 billion years, the Sun has been the ultimate source of energy to the Earth [1]. Solar energy has been, is and will continue to be one of the key sources of renewable energy. Rewinding time by 200 years, it is startling to know that the entire world's energy demand was completely fulfilled by solar energy. This trend however did not last long as people at the forefront of the industrial revolution realised that fossil fuels were cheap and efficient.

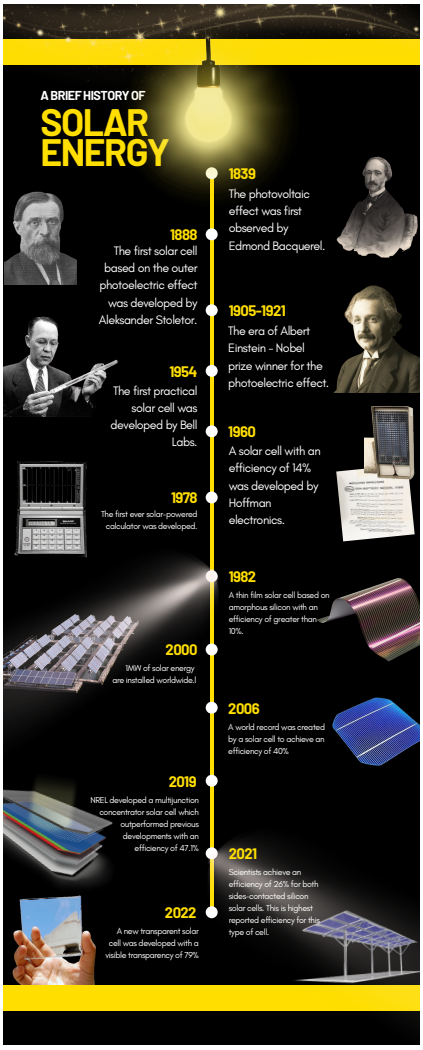

Figure 1.1: A brief history of photovoltaics

The sun's significance as a powerful energy source has been acknowledged since ancient times, with practical applications observed in Archimedes' use of reflective surfaces to ignite Roman ships. The idea of harnessing solar energy to generate electricity, known as photovoltaics (PV), originated with Alexandre Edmond Becquerel's creation of the first photovoltaic cell in 1839. This work paved the way for subsequent discoveries, including Willoughby Smith's demonstration of selenium's photoconductivity in 1873 and James Clerk Maxwell's confirmation of light's effect on selenium's conductivity in 1874. Charles Fritts further advanced the field by developing a solar cell using selenium in 1883, albeit with low efficiency. Albert Einstein's explanation of the photoelectric effect in 1905, for which he received the Nobel Prize in 1921, marked a significant milestone in the field of PV [2, 3, 4, 5, 6]. With Einstein's breakthrough in photovoltaics, the late 1900s experienced exponential growth in research and innovation. In 1954, Calvin Souther Fulleran an American physical chemist at AT&T Bell Laboratories invented the first practical solar cell with an efficiency of 6% [7]. Subsequently, Hoffman Electronics made significant contributions to the field, achieving a solar cell efficiency of 9% in 1958 and 14% in 1960 [8]. In the 1970s, the oil crisis prompted the exploration of renewable energy sources. dvancements continued in the following years, with the development of amorphous thin-film silicon solar cells in 1982 [9].

Current PV research emphasizes material science, as demonstrated by the development of transparent solar cells with high average transparency [10].Although solar energy currently accounts for only 13.5% of global energy consumption, there is growing recognition of its potential [11]. Efforts are underway to harness solar energy with modern technology and generate electricity from this abundant renewable source.

1.2 Significance of Photovoltaics

The previous section 1.1 provided an overview of the technological advancements in photovoltaics. In this section, the significance of photovoltaics is highlighted, considering the complexities of the global energy market. The recent strain on the energy market, exacerbated by the Russia-Ukraine conflict, emphasizes the interdependence of countries for meeting their energy demands. Similar to the oil crisis in 1970, the current situation is characterized by a reliance on natural gas and raises questions about the impact on the energy transition [12]. The world's target of achieving Net-zero emissions by 2050 further underlines the urgency of transitioning to renewable energy sources to limit global temperature rise to 1.5° [12]. To achieve net zero emissions, a significant increase in renewable energy sources (RES) for electricity production is necessary, considering various factors such as costs, market conditions, policies, and technological feasibility [12]. This thesis focuses on solar energy as a key component of the energy transition. Projection towards a net zero emissions scenario requires understanding the energy demand in 2050, which is closely linked to population growth. Figure 1.2 (a) illustrates a projected population growth rate of 23.69% (18757 million people) higher in 2050 compared to 2021.

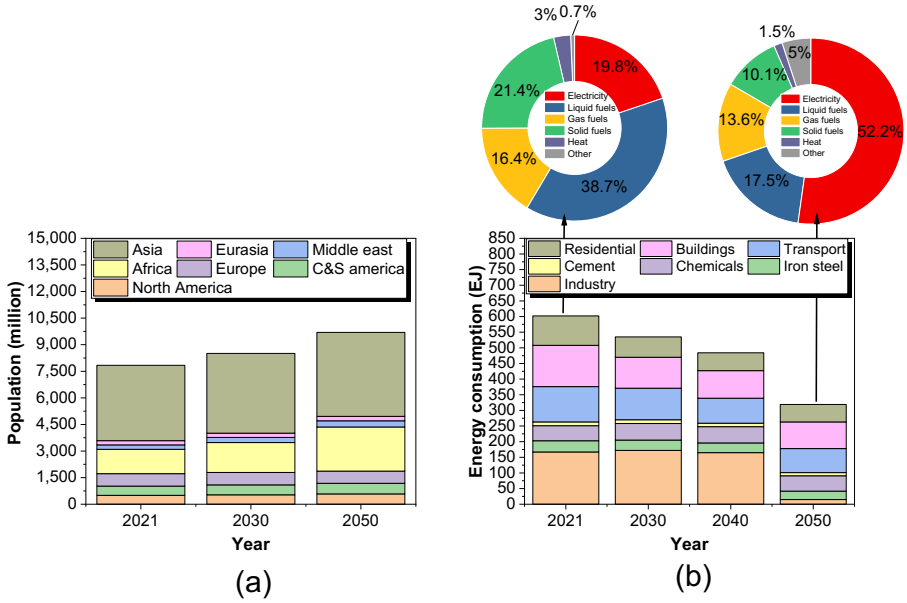

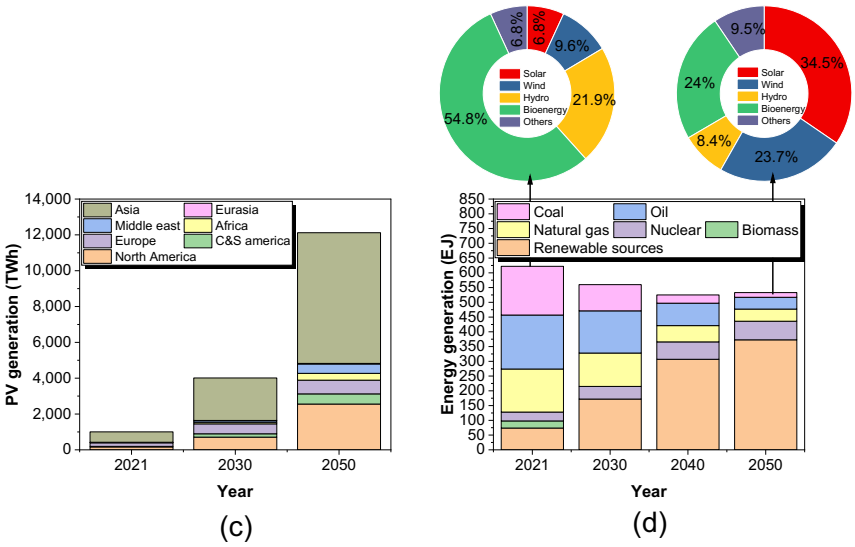

Figure 1.2: Required energy outlook. (a) Predicted population growth. (b) Energy demand trajectory for an NZE scenario. (c) Composition of renewable energy sources. (d) Energy generation in the NZE scenario. Data retrieved from https://www.iea.org/reports/world-energy-outlook-2022

Figure 1.2 (b) depicts the trajectory of energy demand towards achieving net zero emissions (NZE) by 2050, with electricity dominating at 51% compared to 20% in 2021. This highlights the transition towards electricity as the primary form of energy utilisation, emphasizing the importance of technologies that directly produce electricity without major energy conversions. Solar energy plays a pivotal role, with its contribution to the renewable energy mix increasing from 7% in 2021 to 35% in 2050, demonstrating its significance in achieving energy independence from fossil fuels. Solar energy production will see a remarkable 1100% increase worldwide (from 2021-2050), particularly in Asia, as shown in Figure 1.2 (c) and (d).

In conclusion, solar energy is leading the transition towards sustainable energy sources, making significant contributions among other renewables. This thesis aims to advance photovoltaics and promote the improved and accelerated utilization of solar energy globally.

1.3 Thesis Motivation

Up until this point, sections 1.1 and 1.2 have shown how the idea of photovoltaics came to be and how crucial it is to the world's energy security both today and in the future. This section will focus on the motivation behind this thesis and assess how this thesis provides valuable information and results to enhance the performance of a solar cell. It is widely known that the sun generates an enormous amount of energy but the question is *why is the efficiency of solar panels so low? (an average of 18-20 %)* The answer to this question can be given using three interpretations as shown below using figure 1.3 as reference.

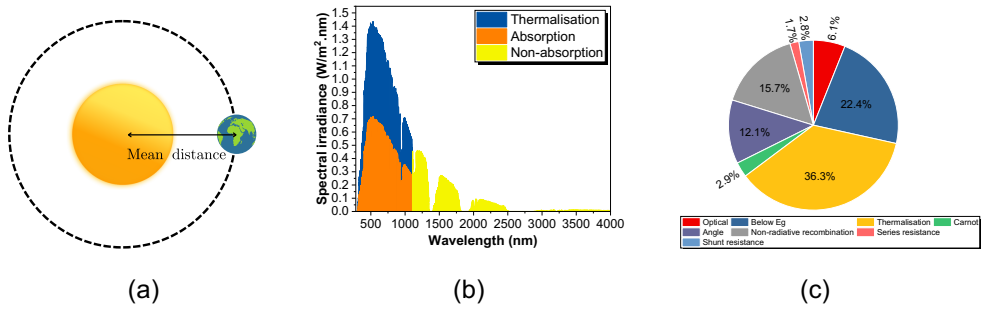

(a) (b) (c)

Figure 1.3: (a) Mean distance between Earth and Sun and power received by the solar panels on Earth. (b) The solar spectrum for a crystalline silicon solar cell with $E_g = 1.12eV$. (c) Loss mechanisms in a solar cell. Data for the spectrum and loss mechanism is retrieved from https://www.nrel.gov/grid/solar-resource/spectra-am1.5.html and [13] respectively.

1. The assessment of solar power generation starts with understanding the amount of power received from the Sun. Figure 1.3 (a) demonstrates the power received by panels on Earth on a clear day. The power generated by the Sun (P_{sun}) and the power received by the Earth's outer surface (P_{earth}) is calculated as shown in appendix A.1.1. Therefore, to estimate the irradiation received by solar panels on Earth, the albedo (α_{earth}) of the Earth's atmosphere is taken into account, considering a clear sky (P_{panels}) [14, 15].

$$P_{panels} = P_{earth} \times (1 - \alpha_{earth}) = 1370 \times (1 - 0.27) \cong 1000 \left(\frac{W}{m^2} \right) \tag{1.1}$$

2. In Figure 1.3 (b), the plot of spectral irradiation demonstrates the distribution of energy from the Sun, with the red region representing the fraction absorbed by solar panels. On average, solar panels absorb 50% of the spectrum, depending on the cell technology. The yellow region corresponds to unabsorbed wavelengths beyond the band-gap energy, while the blue region represents energy lost through thermalization [14].

3. Figure 1.3 (c) reveals the loss mechanisms that impede the performance of solar cells. Thermalization leads to a 30% loss as excess energy converts to heat instead of electricity. Below bandgap losses account for an 18% loss when photons lack sufficient energy for electron-hole pair generation. Optical losses, comprising 15% of the total loss, include reflective and angular losses. Reflective losses occur between cell layers, while angular losses result from varied angles of incidence. Minimizing these losses relies on material properties and can be addressed using technologies such as anti-reflection coatings and light trapping textures.

This thesis focuses on the quantification and reduction of optical losses in a polymer-based mono-crystalline silicon PERC solar cell. The aim is to propose methods that effectively mitigate these losses and enhance the cell's performance.

1

1.4 Light management in solar cells

In this section, a concise version of all the concepts and theories required to completely understand this thesis is given. Light management techniques are found to be instrumental in reducing optical losses. The principal motive behind the light management technique is to maximise the number of photons an absorber layer can absorb to ultimately increase the overall performance of the solar cell. In this section, a set of techniques and methods will be discussed which are used to increase the overall absorptance of the solar cell.

1.4.1 Losses due to Reflection

In optical characterisation, reflectance, transmittance, and absorptance are crucial parameters used for comparison. This section illustrates the significance of front interface reflection using the example of a crystalline silicon solar cell with the configuration - air/Si/air as shown in Figure 1.4.

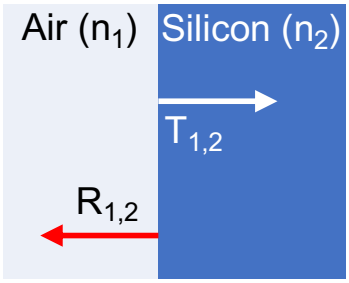

Figure 1.4: Determination of interface reflection losses

The total reflectance (R) and the Transmittance (T) are calculated at normal incidence ($\theta_i = 0^\circ$). Therefore, now by using the Fresnel equations, the total Reflectance and Transmittance and absorptance can be estimated as follows:

$$R = \left(\frac{n_{air} - n_{Si}}{n_{air} + n_{Si}}\right)^2 \times 100 = \underline{35.51\%} \tag{1.2}$$

$$T = \frac{4 \cdot n_{air} \cdot n_{Si}}{(n_{air} + n_{Si})^2} \times 100 = \underline{64.48\%} \tag{1.3}$$

Where, $n_1 = 1$ and $n_2 = 3.95$ are the real part of the refractive index for air and Silicon (at 600nm) used in the Fresnel equation (N = n+ik) [16]. It can be noted from the above calculation that the interfaces have significant losses due to reflection and absorption which accounts to a total of 7.84% which can induce significant losses in a solar cell stack with glass as the front layer. Hence, these losses have to be reduced and this thesis focuses on texturing and other optimisations to reduce this overall losses.

1.4.2 Anti-reflective coatings

In this section, a brief introduction is given to the working principle of anti-reflective coatings. As the name suggests, the primary role of using an ARC is to reduce the interface reflectance between air and the following material.

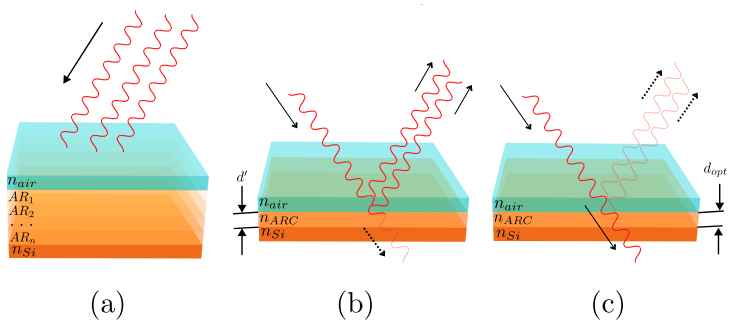

Figure 1.5: Anti-reflective coatings. (a) refractive index grading. (b) concept of constructive interference. (c) concept of destructive interference.

Implementing anti-reflective coatings can be done using two methods:

1. To mitigate the high reflection at the air-Si interface (as discussed in Section 1.4.1), a Rayleigh film is introduced as an intermediate layer with a refractive index of $n_{ARC} = \sqrt{n_{air} \cdot n_{Si}}$. Multiple Rayleigh films can be added between air and Si (Figure 1.5 (a)), significantly reducing reflection through refractive index grading. However, this method is not widely used due to the high cost associated with it. An example is provided in Appendix A.1.2 showing the influence of refractive grading.

2. **ARC based on interference:** The theory of interference can address the limitations of refractive index grading. By adjusting the thickness of the Anti-reflective coatings (ARC), constructive or destructive interference can be achieved. When the thickness is $d' = \frac{\lambda}{2 \cdot n_{ARC}}$, constructive interference occurs, resulting in total reflection of incoming light under ideal conditions (Figure 1.5 (b)). On the other hand, when the thickness is $d_{opt} = \frac{\lambda}{4 \cdot n_{ARC}}$, destructive interference occurs, leading to minimal reflection of light, making it ideal for the front sheet of the solar cell (Figure 1.5 (c)). An example illustrating this concept is provided in Appendix A.1.2.

1.4.3 Texturing

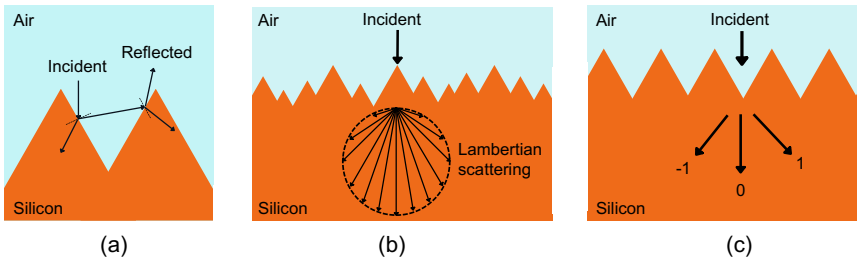

Figure 1.6: Influence of surface texturing. (a) Working principle of front texturing. (b) Lambertian scattering. (c) Diffraction gratings.

1

Surface texturing is another effective technique in reducing optical losses. Surface textures if optimised accordingly can exhibit traits such as anti-reflection and light trapping in combination. Certain important factors affecting the efficiency of surface textures can be enumerated as follows:

1. **Light trapping:** Light trapping combines the effects of light scattering and total internal reflection (TIR). Scattering occurs when light deviates from its original path due to changes in geometry, as depicted in Figure 1.4 (b) for Lambertian scattering. Lambertian scattering leads to uniform scattering in all directions with equal energy distribution. The absorption resulting from Lambertian scattering can be estimated using Equation 1.4 [17]. Meanwhile, TIR occurs at the rear-side of the solar cell, where all light rays are reflected back into the cell, increasing the optical path length. The critical angle for TIR can be calculated using Equation 1.5.

$$A_{Lamb} = \frac{4n^2 \alpha d}{1 + 4n^2 \alpha d} \tag{1.4}$$

$$\theta_{critical} = \sin^{-1}\left(\frac{n_2}{n_1}\right) \; where: \; n_2 > n_1 \tag{1.5}$$

2. **Random and periodic textures:** Texture type plays a crucial role in light scattering, but determining the superior type is challenging. Random textures, with a non-uniform lattice distribution, have shown remarkable performance improvements. They scatter light in all directions, similar to Lambertian scattering. When combined with an Anti-Reflective Coating (ARC), they can achieve a maximum absorption enhancement of $4n^2$, known as the Yablonovitch limit [18]. On the other hand, periodic textures scatter light into discrete angles, exciting a finite number of guided modes. Absorption is directly linked to the number of guided modes. While random textures have demonstrated superior performance, periodic textures can potentially surpass the Yablonovitch limit through specific optimizations and by avoiding light coupling.

3. **Texture sizing:** Texture sizing is crucial for light trapping, depending on the wavelength of light. Large textures, compared to the wavelength (λ), employ ray/geometrical optics to increase light absorption before reflection (Figure 1.6 (a)). Small textures, equal to or smaller than the wavelength, utilize wave optics and offer anti-reflective properties akin to ARC.

1.5 Cell stack configuration

Figure 1.7 illustrates the cell stack configuration of both conventional industry-standard solar modules and the Solarge cell stack. Figure 1.7 (b) presents the conventional solar module, featuring a glass front surface, followed by a layer of EVA (Ethylene vinyl acetate) as the encapsulant. Below the encapsulant, the solar cell is positioned, followed by another layer of encapsulant and the rear insulating backsheet. On the other hand, Figure 1.7 (a) showcases the Solarge cell stack, which shares a similar overall configuration but eliminates the use of an aluminum frame in its cell stack. Notably, the front glass, typically 3-3.2

mm thick, is replaced by a polymer film in the Solarge cell stack. Similarly, the EVA encapsulant is substituted with Solarge's proprietary recipe. Furthermore, the backsheet in the Solarge cell stack is polymer-based and incorporates layers of glass fibers with a honeycomb structure.

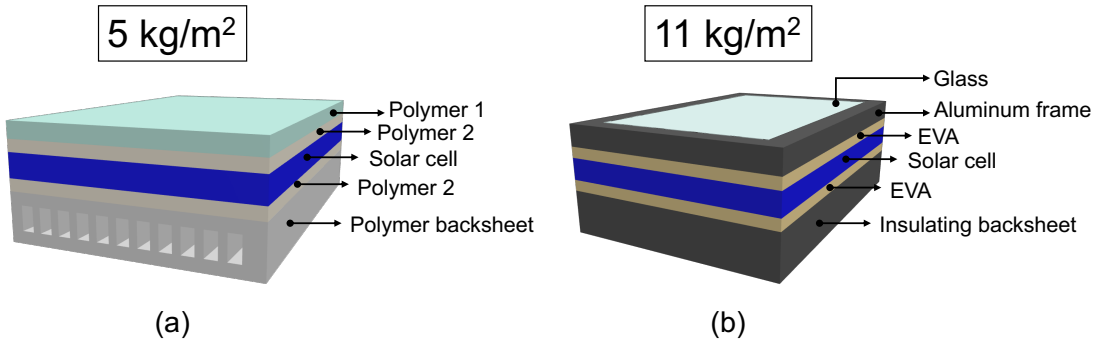

Figure 1.7: Cell stack layouts. (a) Solarge cell stack. (b) Convectional cell stack [19]

As a leading producer of innovative lightweight solar panels, Solarge achieves a significant reduction in weight per unit area compared to conventional glass modules, as evidenced in Figure 1.7. The weight reduction amounts to 54.4%, rendering Solarge modules exceptionally lightweight. Additionally, the polymer materials employed by Solarge to replace conventional methods are non-toxic and possess circular properties, ensuring that Solarge's modules are completely circular and sustainable [20].

For an in-depth understanding of the cell stack configuration, Table 1.1 provides a comparative analysis between the Solarge stack and conventional glass modules.

Table 1.1: Layer properties

Layers	Conventional modules	Solarge modules
Front sheet	Tempered glass	Polypropylene based polymer
Encapsulant	EVA	Solarge recipe
Solar cell	Mono PERC G1 cells	Mono PERC G1 cells
Backsheet	Insulating polymer backsheet	Combination of glass fibres

1.6 Literature review

A detailed literature survey was conducted in this section. Initially, a wide range of scientific articles (approximately 1000) were collected, from which the most relevant ones (approximately 100) focusing on light trapping and related aspects were further examined. For additional insights into the bibliometric landscape, Appendix A.1.3 provides more information.

1

A detailed literature review is enumerated below:

1. In Phase I of the literature review, the material properties of polypropylene (PP), which acts as the base polymer of the front sheet in the Solarge solar cell stack, were investigated. Boydag *et al.* conducted early studies in 1999, examining the reflectance, transmittance, and absorptance of PP-based polymer composites, such as PP/diamond and PP/fiber composites. The experiments involved varying the thickness between 8-29 μm in the wavelength range of 200-25000 nm. The highest absorption coefficient (α) was observed in the PP/20% PP Fiber composite compared to other composites [21, 22] where as it is important that the material used for the front sheet application in photovoltaics show low absorption.

   Mijangos *et al.* focused on thin PP films with a thickness of 12.7 μm to determine the refractive index in the infrared regime. D. Akbar *et al.* characterized PP using terahertz time-domain spectroscopy with dual-RF plasma treatment. PP sheets were tested under three conditions: untreated, treated for 30 minutes, and treated for 60 minutes. The results showed that samples treated for 60 minutes exhibited the highest refractive index (1.8-1.9), while untreated or 30 minutes treated samples had refractive index values ranging from 1.4-1.6 [23].

   Bhavsar *et al.* investigated the refractive index of undoped and PP-doped PVC films. The concentration of PP was varied from 6% to 20% in PVC, and the refractive index was found to increase with increasing PP concentration. The highest absorption coefficient was observed when the PP concentration was 16% [24, 25].

   Research gap

   The optical characterization of polypropylene (PP) primarily focuses on composites and blends with other materials/polymers. Consequently, there is a notable absence of optical property data, including reflectance (R), transmittance (T), absorptance (A), refractive index (n), and extinction coefficient (k), for PP as base polymers under normal and diffuse irradiation.

2. Phase II of this literature review focuses on investigating various types of textures on polymer substrates. Sprafke *et al.* discussed different light-trapping techniques, ranging from simple antireflection coatings (ARCs) to advanced technologies such as 3D photonic crystals, resonant structures, and angular selective structures [26]. Zheng Tang *et al.* and Raju Lampande *et al.* reviewed various textured geometries for polymer-based solar cells, including hemispheres, V-shaped structures, microlenses, and corner cubes [27, 28]. B.Lipovsek *et al.* investigated the performance of different textures on organic and perovskite solar cells, highlighting the importance of textures with flat facets for maximizing short-circuit current density (J_{sc}) [29]. R. Saive reviewed articles on various textures and emphasized the need to evaluate light-trapping methods in terms of parasitic absorption and angle acceptance [30].

   Engineered biomimicry has gained attention in recent years. J. Martín-Palma *et al.* highlighted the significance of biomimetic textured surfaces in reducing front reflection across a broad range of the solar spectrum [31]. E. Tatsi *et al.* and M.

Kim *et al.* summarized photon management technologies using polymer materials, including the use of polymethyl methacrylate (PMMA) as an antireflection coating and the replication of natural textures [32, 33].

Researchers have also explored textures inspired by insects and flowers. S.A. Boden *et al.* created nanonipples inspired by moth-eye structures, achieving low reflectance values [34, 35]. D. Yoo *et al.* replicated the lotus leaf structure, demonstrating improved performance and functionalities [36].

Research gap

An ideal texture with the ability to provide anti-reflection is yet to be optimised by adjusting structural properties such as height, period and diameter. New suitable thin-film materials with high optical properties and mechanical strength are limited which hold the potential to provide anti-reflection.

3 Phase III of the literature review focuses on the performance criteria of textures, particularly angular performance. Non-standard operating conditions, such as angle-dependent losses, significantly impact solar panel performance [37]. The challenges and need for further investigation regarding angular losses have been highlighted in [38]. Optimization of texture morphology is essential for improving performance at higher angles of incidence [39]. Soiling, a complex issue, can be addressed through self-cleaning approaches using textured front surfaces [40]. Material selection for the front sheet must balance transparency, durability, and superhydrophobicity [41]. A Comprehensive analysis considering various factors is necessary to understand financial losses caused by dust/soil accumulation [42]. Further research is needed to address gaps in material selection, angle dependency, aging, and other mechanisms [43].

Research gap

In depth investigations pertaining to angular dependent studies with different textured geometries on a polymer front sheet needs to be studied. Additionally, analysis of soiling in PV technologies lacks a clear comparison in current literature and the degradation of textures under prolonged soiling is not well established. However, the issue of soiling is out of scope of this thesis.

4 Phase IV of the literature review addresses the fabrication techniques for manufacturing textures on polymer substrates. Various methods have been explored, including hot embossing, replica molding, roller extrusion, photofabrication, lithography, and thermoforming. These techniques have been employed with thermoplastic polymers and offer flexibility and the ability to generate intricate structures [44, 45, 46, 47, 48, 49].

Hot embossing is the most commonly used technique on a laboratory scale, while injection molding is preferred for industrial micro molding due to fast cycle times.

However, conventional hot embossing techniques require periodic heating and cooling, resulting in increased cycle times [50]. To overcome this, rapid thermal response (RTR) embossing tools with rapid heating and cooling capabilities have been investigated, showing promising results in thermal fatigue tests [51].

Other innovative techniques include hybrid extrusion rolling embossing, ultrasonic embossing, and pneumatically diaphragm-driven drop-on-demand inkjet systems. These methods have shown potential for continuous mass production of textured surfaces, such as microlens arrays, with high quality and low cost [52, 53, 54].

Nano-imprint lithography is an economical technique used for imprinting nanotextures on various surfaces, including plastics and polymers [55, 56]. Exploring the implementation of surface topologies into 3D scaffolds is an area of interest for future research [57, 58].

However, working with polymers and plastics presents challenges, including the melting of polymers during the embossing process and the demolding of molds from the polymer, which requires improvement in heat-dependent methods [59].

Research gap

With all the above mentioned techniques, fabrication of textures on a polymer substrate is a relatively difficult process when compared to glass. There are several research gaps in this field of study such as optimising the hot embossing technique with respect to cycle time, mold creation, cost effectiveness and scalability. More experimentation should be performed with the teflon sheets which act as a release agent in the lamination process.

1.7 Research questions

In this section, a set of research questions are defined which will be systematically addressed over the course of this thesis. These research questions have been formulated from the research gaps found in the literature review as mentioned in section 1.6. Hence, the following research questions will be addressed in the same periodic order in this thesis.

1. What are some of the latest trends, techniques, and methodologies being utilized in polymer texturization?
2. How to optically characterise polymer materials and determine optical losses without the presence of textures?
   (a) What techniques are available for measuring the thickness of individual polymer layers?
   (b) What methods can be used to accurately determine the optical constants of polymer materials?
   (c) How can the current optical performance of a Solarge stack be comprehended?
   (d) What approaches can be used to determine the overall optical losses in terms of electrical parameters?

3. What is the process for developing textures on polymer surfaces and their effect on optical losses?
   (a) How can textures be constructed and analyzed on polymer surfaces?
   (b) What are the typical methods used for fabricating these textures?
   (c) Which texture is the most practical and efficient?
   (d) How do these textures perform when exposed to different angles of incident light?
   (e) How do these textures influence the power output of solar modules?
4. In what ways can the company benefit financially from this thesis research?

1.8 Thesis Outline

This section provides an overview of the thesis layout. Each chapter focuses on a specific research question and provides the answer at the end. The structure of the thesis is as follows:

Chapter 2 focuses on the characterization of polymer materials used in the Solarge solar stack, with a particular emphasis on determining their optical properties. These characterized optical properties serve as input parameters for constructing an optical model using Genpro4, which is then validated through experimental approaches. The chapter concludes by calculating the overall optical losses in the Solarge stack without the presence of any front sheet texturing.

Chapter 3 is the centerpiece of this thesis, addressing the texturing aspect of the front sheet. This chapter consists of five phases, each exploring different aspects of front sheet texturing. Experimental and computational approaches are employed to evaluate the most viable and ideal texture morphology for the Solarge cell stack. Finally, two prominent optimized cell stack recommendations are provided, and the optical and electrical performance of these optimizations are evaluated.

Chapter 4 gives provides a brief summary of the thesis, encompassing all significant observations made, and concludes by highlighting potential areas for future research.

2

Optical characterisation

The objective of this chapter is to address the second research question of the thesis, focusing on the optical characterization of the polymer front sheet and the encapsulant. The characterization process begins by measuring the thickness of each layer after lamination. Subsequently, both computational and experimental techniques are employed to predict the optical constants (n, k) for both layers. Once the optical constants are determined, an optical model using GenPro4 is developed for the mono-PERC cell. The individual models are then combined and validated against measurements to simulate the performance of the Solarge cell stack. With the validated cell stack optical model, the electrical performance is evaluated using a flat front sheet without any textures. Both computational and experimental techniques are employed, including a cell-to-module analysis conducted with the Fraunhofer smartCalc.CTM software. Based on the results obtained from the electrical simulation, the current optical losses in the Solarge cell stack are assessed, establishing the base case for comparison in the chapter 3.

2.1 Introduction to optical characterisation

The objective of this chapter is to optically characterize each polymer layer of the Solarge cell stack. Optical characterization plays a crucial role in understanding the interaction between light and matter and is essential for developing an accurate optical model using GenPro4. This chapter serves as the foundation for evaluating the performance of the Solarge stack with different textures, as studied in Chapter 3.

In photovoltaic applications, the key layer optical properties are reflectance (R), transmittance (T) and absorptance (A) which are usually derived from material properties such as refractive index (n), and the extinction coefficient (k). These material properties are vital for assessing the optical behavior and losses in the system. The following sections will discuss the methodology employed to determine these optical properties, analyze their significance, and ultimately provide an evaluation of the overall optical losses in the system.

2.2 Roadmap

In this section, a roadmap is provided consisting of five phases as shown in figure 2.1.

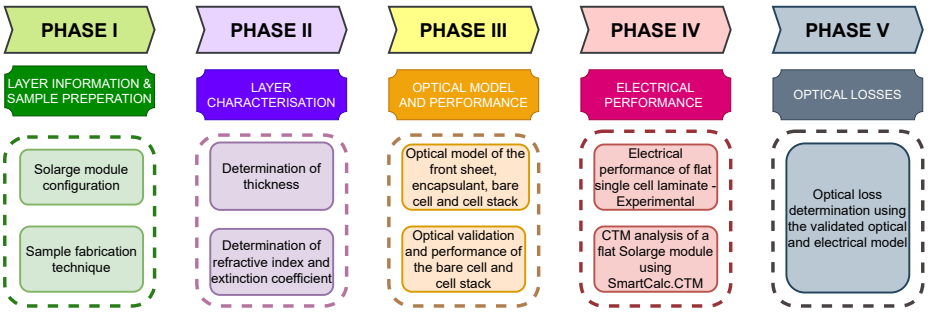

Figure 2.1: Roadmap for Chapter 2

Each phase of this chapter serves as an incremental step towards achieving the ultimate goal of quantifying the current optical losses in the system. The topics addressed in each of the five phases is as follows:

1. **Phase I:** In the initial phase, a thorough understanding of the materials used in the Solarge solar module is described as shown in 1. By discerning the arrangement of layers within the cell stack, the focus is then shifted to fabricating small-scale polymer samples tailored for optical characterizations.
2. **Phase II:** Building upon the previous phase, emphasis is placed on determining vital properties, such as layer thickness, refractive index (n) and extinction coefficient (k) for the Solarge materials. However, the determination of these parameters for polymers presents unique challenges, which are concretely explored within this phase.
3. **Phase III:** In this phase, a transition is made towards computational analysis, leveraging the optical parameters obtained in Phase II as inputs for constructing optical

models using GenPro4. Initially, individual models are developed for the front sheet, encapsulant, and the mono PERC cell, with each model subjected to individual validation. Subsequently, an optical model of the entire Solarge stack is constructed utilising the individual models. The validity of the optical simulation results is then established by meticulously comparing them with experimental data derived from the fabrication of flat single cell laminates. Through this iterative process of model development and validation, the accuracy and reliability of the optical simulation are ensured.

4. **Phase IV:** Electrical characterization takes center stage in this phase, with a focus on the cell-to-module ratio analysis using the Fraunhofer SmartCalc.CTM (cell-to-module analysis) software. The software's accuracy and reliability are assessed through experimental validation ensuring reliable results.

5. **Phase V:** The final phase is dedicated to estimating the overall optical losses in the Solarge solar modules featuring a flat front sheet, serving as a vital baseline for Chapter 3. This phase sets the stage for exploring the impact of texturing on optical performance.

2.3 Phase I: Layer information and Sample preparation

This section presents an overview of the manufacturing technique employed by Solarge, highlighting the distinct fabrication processes for the front sheet and the encapsulant. Additionally, it explains how polymer samples are fabricated specifically for optical characterization purposes.

2.3.1 Method of sample fabrication

This section explains the fabrication process of the samples used for optical characterization. The focus is on the front sheet and encapsulant, which are the primary layers that interact with light before reaching the solar cell. Flatness is a crucial aspect to maintain as it might influence the optical properties, hence all polymer samples are fabricated between two glass slabs to ensure level flatness.

Figure 2.2 provides a detailed overview of the sample fabrication process for optical characterisation. The following steps are involved:

1. **Layering process:** As depicted in Figure 2.2 (a), the layering process begins by placing a front sheet and an encapsulant between two glass slabs to ensure flat surfaces post lamination.

2. **Lamination process:** Figure 2.2 (b) illustrates the lamination process, where both samples are placed together in a vaccum laminator which operates at particular temperature, pressure and time. The samples are placed between two sheets of Teflon as depicted by the orange layer in figure 2.2 (b) to ensure that the samples do not adhere to the laminator.

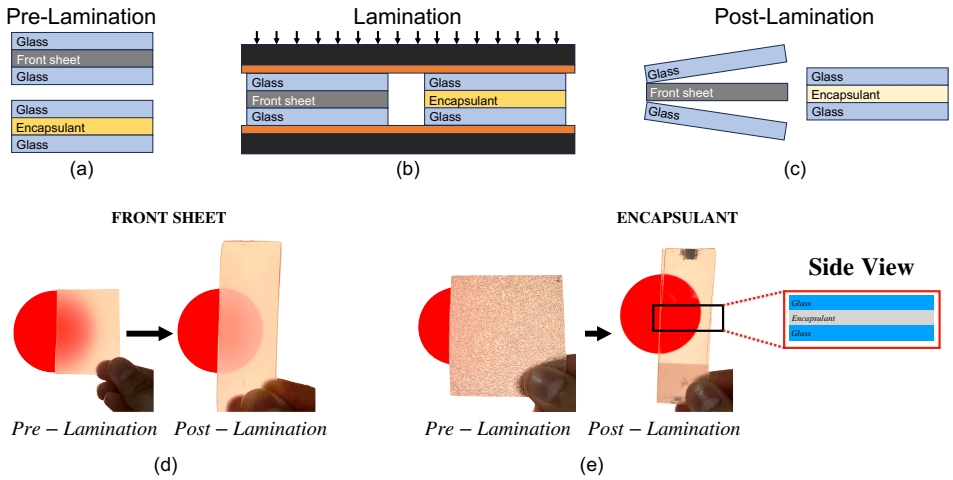

Figure 2.2: Samples fabrication process. (a) Layering samples between two glass slabs prior to lamination. (b) Process of vacuum lamination. (c) samples post lamination. (d) Front sheet pre/post lamination difference. (e) Encapsulant pre/post lamination difference. *NOTE: The slight tint of yellowness in the image is due to the ambient lighting conditions and camera settings and is not an inherent property of the sample.*

3. **Post lamination observation:** Figure 2.2 (c) showcases the samples after the lamination process, revealing an intriguing observation. The front sheet easily detaches itself from the glass slabs, indicating its potential suitability as a substrate for texturing. This implies that texturing the front sheet using different master mold materials could be a viable option. Conversely the encapsulant adheres to the glass slabs during lamination. Consequently, the layer stack for optical characterization of the front sheet consists of air | Front sheet | air, whereas for the encapsulant, it is air | glass | encapsulant | glass | air.

4. **Pre and post lamination images:** Figures 2.2 (d) and (e) depict visual representations of the front sheet and the encapsulant, showcasing their appearance before and after the lamination process. The red circle, which serves as a visual aid in the background of the samples, highlights the disparity in transparency between the front sheet and the encapsulant pre- and post-lamination. It is essential to acknowledge that the material properties undergo significant changes, particularly for the encapsulant, after the lamination process. Since this thesis focuses on the post-lamination scenario, the optical characterization is conducted on samples from both the front sheet and the encapsulant after the lamination process.

2.4 Phase II: Layer Optical characterisation

In this section, optical properties of the front sheet and encapsulant is discussed as shown in figure 2.1. Firstly, the method of determining the layer thickness is discussed followed by the methodology used to determine the optical constants i.e. the refractive index (n) and the extinction coefficient (k).

2.4.1 Determination of thickness

The materials used in thesis are in the order of hundreds of microns thick. Hence, the method to determine the thickness is relatively simple. To evaluate the thickness of each polymer layer, the American Society for Testing and Materials (ASTM) standard guide for "determination of thickness of plastic film test specimens" is used [60].

(a) (b)

Figure 2.3: ASTM procedure to measure thickness of polymer films. (a) HBM Digital Outdoor Micrometer. (b) Thickness measuring technique. Image of the micrometer retrieved from https://www.hbm-machines.com/nl/

The methodology as per the ASTM standard is as follows:

1. A micrometer capable of reading repeatable values with a least count of ±0.001 mm can be used as a reliable indicator as shown in figure 2.3 (a).
2. The final value of the thickness is analysed by measuring multiple individual readings on the sample as shown in figure 2.3 (b) and to ensure that each individual value does not exceed 10% of the average value.

The accurate determination of the thickness of the polymer layers was carried out following the prescribed methodology by ASTM. The measurements were performed both pre and post lamination to examine the influence of lamination on the thickness values. As mentioned earlier, the polymer layers undergo a transition state during the lamination process which then leads to a change in the thickness of the polymer layers post lamination, as observed in the table below.

Table 2.1: Layer thickness

Sample	Thickness (μm)
Front sheet prior lamination	t_f
Front sheet post lamination	T_f ($< t_f$)
Encapsulant prior lamination	t_e
Encapsulant post lamination	T_e ($< t_e$)
Backsheet	T_b

2.4.2 Process of determining refractive index (n) and extinction coefficient (k)

Measurement tools

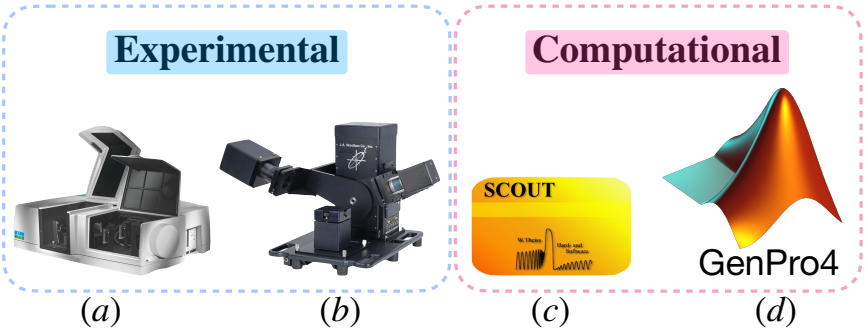

Figure 2.4: Measuring tools used to estimate optical constants. (a) Perkin-elmer UV/Vis/Nir 950/1050 Spectrophotometer. (b) Woollam Ellipsometry. (c) SCOUT. (d) GenPro4

Firstly, understanding the measuring tools that is used to evaluate optical properties is important. Hence, 2.4 shows the experimental and computational tools used in this work whose functions are briefly elaborated as follows:

1. **Spectrophotometer:** Measures the total normal Reflectance (R) and transmittance (T) of the sample. It can also used to measure the diffuse transmittance of the samples (T_d).

2. **Ellipsometry:** Measures and fits a model to evaluate the $n\&k$ for the sample required.

3. **SCOUT:** A solftware platform capable of determining the optical constants (n,k) based or optical performance (R,T) based on the given input. [61].

4. **GenPro4:** Performs optical simulation based on the given input interms of refractive index and extinction coefficient [62].

For this chapter, the sectrophotometer and the SCOUT software play a pivotal role in determining the optical constants. Hence, the next upcoming sections give a brief outlook on the working modes of the SCOUT software.

Computational tool: SCOUT

Figure 2.5 illustrates three different methods available in SCOUT for optical characterization. The first method involves using a user-defined dielectric model, where inputs of refractive index (n) and extinction coefficient (k) are provided to obtain reflectance (R), transmittance (T), and absorptance (A), as depicted in Figure 2.5 (a). The second method utilizes predefined models from the SCOUT database where the software tries to fit a model to the measured R, T, and A resulting in the prediction of the n and k, as shown in Figure 2.5 (b). The third method employs the inbuilt "pane wizard" or "foil wizard," enabling the direct determination of n and k from R, T, and A measurements, as demonstrated in Figure 2.5 (c). As the aim of this chapter is to deduce the optical constants of the Solarge's layers. The focus is primarily fixated on using/understanding the pane wizard and the foil wizard.

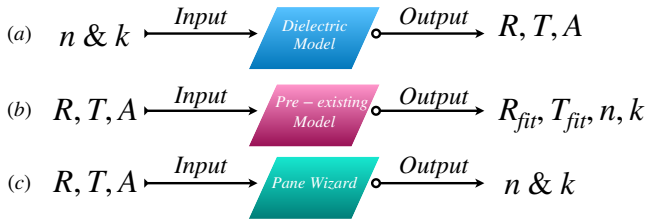

Figure 2.5: Working principle of SCOUT. (a) The dielectric model. (b) Pre-exisiting model in the SCOUT database. (c) The pane and foil wizard.

Challenges & possibilities in evaluating the optical constants for polymers

The last section presented method/techniques used to evaluate the optical constants for any material in general. However, from experimental attempts and computational trials, certain limitations and challenges were observed for the case of transparent polymers such as front sheet and encapsulant. The challenges observed are enumerated as follows:

1. **Spectroscopic ellipsometry:** Is usually a straightforward method for measuring n and k. however, this method cannot be applied to thick transparent polymers such as the front sheet and encapsulant. This limitation arises because the thickness range measurable by spectroscopic ellipsometry typically does not exceed tens of microns. As film thickness exceeds this limit, resolving interference oscillations becomes increasingly challenging [63].

2. **The dielectric model:** The dielectric model in SCOUT cannot be employed in this case since the determination of n and k values is the primary focus of this chapter and the dieletric model requires n,k as the input as shown in figure 2.5(a).

3. **Pre-existing models:** There are no pre-existing models available in the SCOUT database for the polymers used in the front sheet and encapsulant. These models are necessary for fitting n and k data based on the total reflectance, transmittance, and absorptance (R, T, A) measurements. Therefore this method also cannot be used in this case.

4. **Pane wizard:** The pane wizard is primarily used for the sample configuration - Air/polymer sample/Air. This tool takes the total reflectance and transmittance measurements of the sample as input and uses certain equations to predict the optical constants of the sample.

5. **Foil wizard:** The foil wizard is a similar tool as the pane wizard which predicts the optical constants of the sample with the configuration - air/glass/polymer sample/-glass/air.

Hence, from the above possibilities, the spectrophotometer, SCOUT and GenPro4 play a pivotal role in extracting and validating the optical constants.

Optical constant of the front sheet

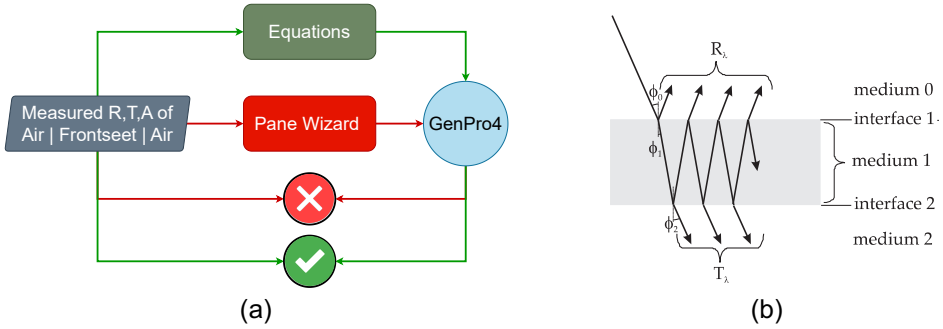

Figure 2.6: Determination of front sheet optical constants. (a) Methodology utilised to determine front sheet optical constants. (b) concept of multiple interface reflections.

The overall methodology for determining the optical constants of the front sheet, with the interface configuration of air/front sheet/air, is illustrated in Figure 2.6. The pane wizard from SCOUT is initially used, accurately determining the refractive index but not the extinction coefficient as shown in figure 2.7 (a). This limitation became evident when the optical constants obtained from the pane wizard were inputted into GenPro4, which failed to predict the loss in photocurrent density due to reflective and absorptive losses. To address this, equations A.8 and A.9, based on ray tracing of a simple multiple layer system with two interfaces (Figure 2.6 (b)), are employed to accurately predict the extinction coefficient [64]. Detailed expressions of these equations can be found in Appendix A.2.2.

$$n(\lambda) = \frac{1 + \sqrt{R_2}}{1 - \sqrt{R_2}} \tag{2.1}$$

$$\alpha(\lambda) = \frac{|ln(1 - A_2)|}{W} \Rightarrow k(\lambda) = \frac{\alpha(\lambda) \cdot \lambda}{4 \cdot \pi} \tag{2.2}$$

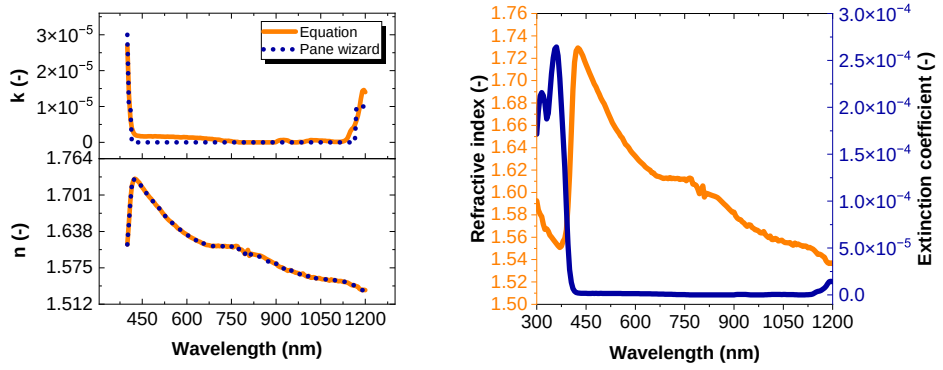

Figure 2.7: Optical constants. (a) Refractive index and extinction coefficient of front sheet using pane wizard and equation. (b) Final optical properties of the Solarge front sheet using the equation.

Figure 2.7 (a) highlights the disparity between the optical constants obtained from the pane wizard and equation. While the extinction coefficients are comparable, the pane wizard significantly underestimates the extinction coefficient in the 400nm-600nm wavelength range, causing the discrepancy. As a result, for subsequent simulations, the optical constants derived from the equation are utilized for the front sheet.

Optical constant of the encapsulant

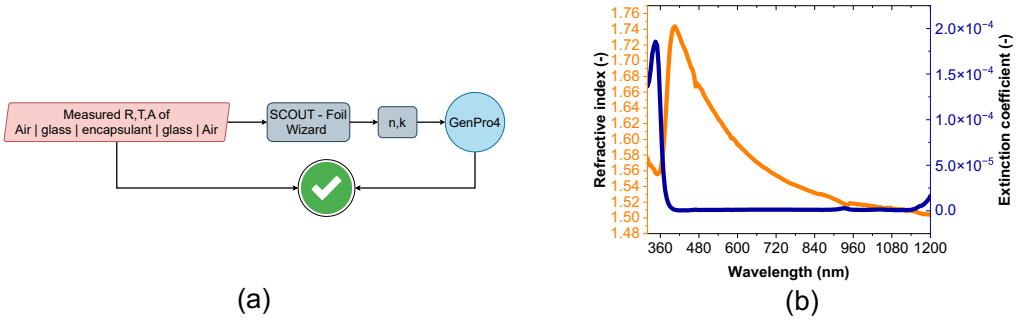

Figure 2.8: (a) Methodology to determine the optical constant for encapsulant. (b) Optical constants extracted from foil wizard for encapsulants.

Figure 2.8 (a) and (b) illustrate the methodology and the optical constants for the encapsulant. The determination of the optical constants for the encapsulant differs from that of the front sheet due to the air/glass/encapsulant/glass/air interface configuration. In this case, the foil wizard tool is employed, which follows the same principle as the front sheet with multiple light interactions calculated, considering additional glass interfaces. Unlike the pane wizard, the foil wizard yielded consistent results, and the subsequent simulations using GenPro4 provided accurate predictions compared to measurements, as demonstrated in the upcoming sections with the optical models.

2.5 Phase III: Optical model and performance

In this section, the optical models for the front sheet, encapsulant, and solar cell are established. Each individual optical model is validated against experimental measurements to ensure accuracy and reliability. Subsequently, these models are combined to form the optical model of the Solarge cell stack. The methodology used to create the optical model for the polymer layers follows the approach outlined earlier using the glass sample. However, the optical model for the cell requires a slightly different method, which will be elaborated upon in this section.

Finally, the performance of the cell stack is calculated using the established optical models. The obtained results are then compared with real-time measurements to evaluate the closeness between the simulation and experimental data. This comparison serves as a means to assess the accuracy and validity of the optical model in predicting the performance of the Solarge cell stack.

2.5.1 Front sheet and encapsulant

In this subsection, individual optical models are created for the front sheet and the encapsulant, as shown in Figure 2.9 (a) and (b) respectively. The optical constants derived in the previous section are used as input for the simulations. The front sheet simulation is conducted for the air/frontsheet/air configuration, while the encapsulant simulation considers the air/glass/encapsulant/glass/air configuration. The results of the simulations are compared to the measured values, and the mean squared error (MSE) for each component (R, T, and A) is presented in Table 2.2. The low MSE values indicate a good agreement between the simulations and experiments.

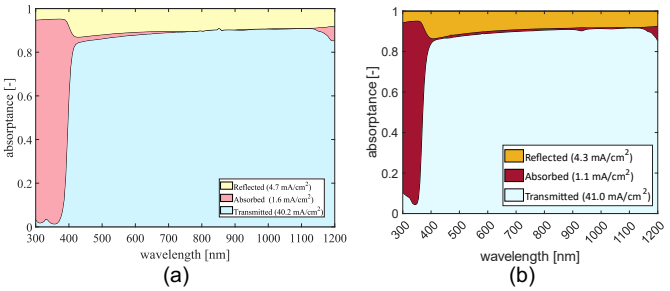

Figure 2.9: (a) Optical model of the front sheet. (b) Optical model of the encapsulant.

Table 2.2: Electrical performance of a flat single cell laminate

Samples	$R_{avg}(\%)$	$T_{avg}(\%)$	$A_{avg}(\%)$	n_{avg}	$R_{MSE}(\%)$	$T_{MSE}(\%)$	$A_{MSE}(\%)$
Front sheet	9.55	79.48	10.98	1.60	1.86×10^{-11}	4.33×10^{-9}	4.8×10^{-9}
Encapsulant	8.88	82.93	8.19	1.57	2.21×10^{-6}	6.14×10^{-4}	6.30×10^{-6}

2.5.2 Bare Mono PERC Solar cell

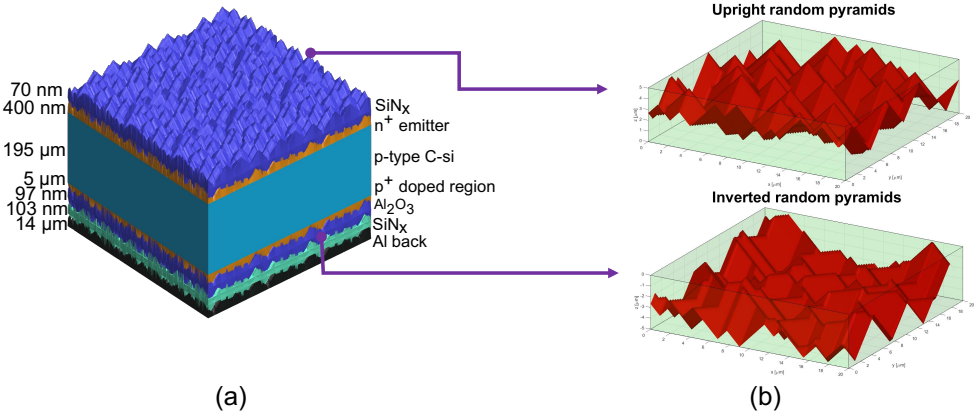

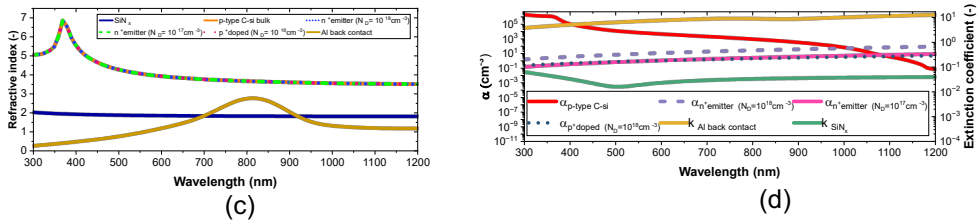

Figure 2.10: Optical model a bare PERC cell. (a) Layer stack of an industrial mono-PERC G1 solar cell. (b) Types of textures used in the front and the rear sides of the cell. (c) Refractive index of the layers comprising the cell. (d) Extinction coefficient and absorption coefficient of the layers comprising the cell.

In this section, an optical model is constructed for an industrial mono- Passivated Emitter and Rear Contact (PERC) cell. Figure 2.10 showcases the optical layers of the G1 PERC cells. It can be noted from the figure that the cell has random upright pyramidal textures on top of which a SiN_x anti-reflective coating is deposited. A n+ emitter layer is followed next to facilitate efficient electron-hole collection and transfer. The n+ emitter layer is described using two seperate layers each 200 nm thick with carrier concentrations decreasing logarithmically from 10^{18}-10^{17} cm^{-3} with depth from the front surface [65]. The cell has a p-type crystalline silicon bulk layer which is 195 μ m thick. On the rear side of the absorber layer, there is a p+ doped layer with carrier concentration of 10^{18} cm^{-3} followed by a layer of Al_2O_3, SiN_x and an aluminium back surface field.

The optical properties of layers comprising the cell is shown in figure 2.11 (b). The refractive index and the extinction coefficients of SiN_x, Al_2O_3 and Aluminium back contact was utilised from the default database of GenPro4. In order to include the effects of the doped regions, the concept of free carrier absorption has been used in this work [66].

$$\alpha_{FCA,n^+} = 1.68 \times 10^{-6} \times N_D \times \lambda^{2.88} \; ; \; (N_D = 10^{18}, 10^{17} cm^{-3}) \tag{2.3}$$

$$\alpha_{FCA,p^+} = 1.82 \times 10^{-9} \times N_D \times \lambda^{2.18} \; ; \; (N_D = 10^{18} cm^{-3}) \tag{2.4}$$

To determine the optical properties of the n^+ and p^+ doped region, equations 2.3 and 2.4 are used respectively. The refractive index of the layers are kept the same as for an intrinsic c-Si layer but the coefficient of absorption is altered according to the free carrier absorption theory. Similarly, to estimate the optical properties of a p-type c-Si layer, equation 2.5 is used where again the refractive index of the layer is kept the same as for an intrinsic c-Si layer but the absorption profile is changes as per the equation.

$$\alpha_{FCA,p-Si} = \alpha_{intrinsic} + \alpha_{FCA,p^+} \tag{2.5}$$

Once the optical properties of all the layers have been determined, this is given as an input to GenPro4 to simulate the optical performance of the cell.

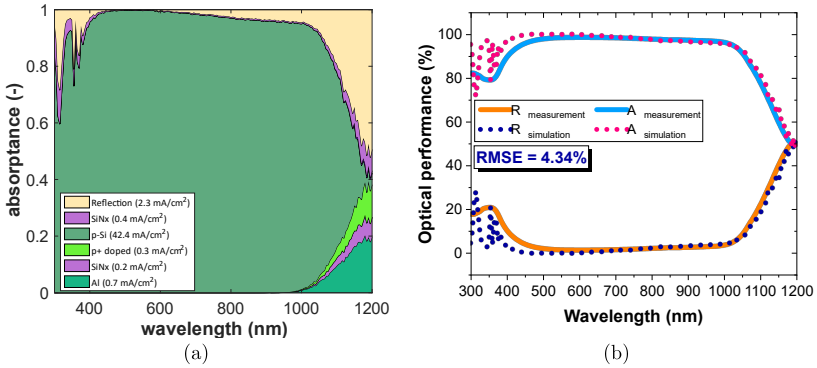

(a) (b)

Figure 2.11: Optical simulation of the PERC cell. (a) Results of the optical model. (b) Comparision of optical properties with measurements.

Firgures, 2.11 depicts the result of the optical model. Figure 2.11 (a) shows the optical performance of the cell interms of reflectance (R), absorptance (A) and transmittance (T). The model also gives the value of the photocurrent density (J_{ph}) of the active layers in the stack. The cell performs ideally (A_{c-Si} = 98.42%) in the wavelength region of 400nm-800nm where most of the incoming light is absorbed by the active layers hence leading to a photocurrent density of $42.4 mA/cm^2$. Figure 2.11 (b) shows the results of the optical model in comparison to the measurements. This plot shows the deviation of R and A with respect to the values obtained using experiments. The value of transmittance is not highlighted here as it a very small portion of the components. The optical model predicts a good match to measurements in the visible region with slight deviations in the infrared and UV regions. The RMSE of the optical model in the wavelength range of 300nm - 1200nm is 4.34% but this reduces to 2.5% in wavelength range of 400nm - 1000nm.

2.5.3 Solarge cell stack

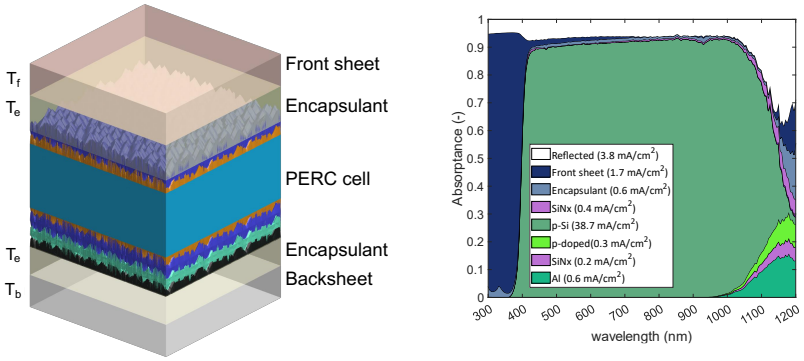

(a) (b)

Figure 2.12: Optical model of the solarge stack. (a) Layer stack of Solarge's standard laminate. (b) Optical performance of the stack.

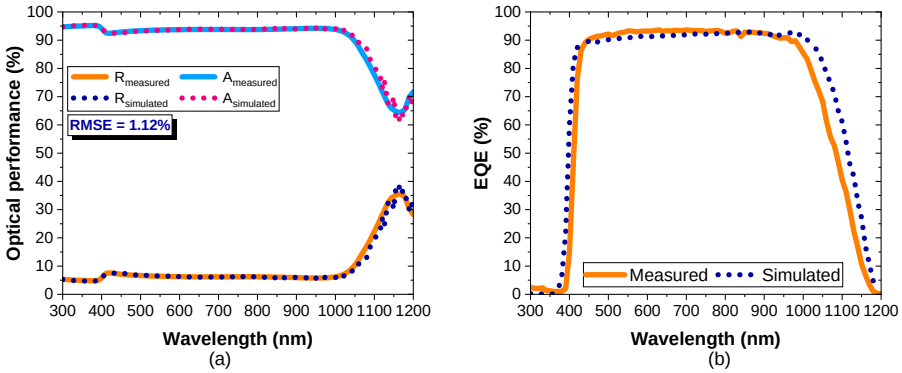

Figure 2.13: Optical simulation of the solarge stack. (a) Comparison of optical properties with measurements (b) EQE comparison between measurement and simulation.

In this section, the optical model and performance of the flat Solarge stack are discussed by combining the previously established optical model. Figure 2.13 (a) and (b) provide an overview of the stack and the results obtained from the optical simulation using GenPro4. Notably, a photocurrent density loss of 2.3 mA/cm^2 is observed due to front sheet reflection. Figure 2.13 (a) illustrates a comparison between simulations and measurements in terms of optical properties, revealing a reduced root mean square error (RMSE) of 1.12% within the wavelength range of 300nm-1200nm. Figure 2.13 (b) presents the difference in external quantum efficiency (*EQE*) between the measured and simulated cell. It is evident that there is good agreement between the measured and simulated results up to 1000nm, with a slight mismatch in the long wavelength regime. This discrepancy can be attributed to GenPro4 providing *EQE* values for c-Si without considering recombination losses, whereas the actual measurements account for these losses. Furthermore, the measured short-circuit current (J_{sc}) of the stack is slightly lower than the photocurrent density (J_{ph}) obtained from simulations, as per convection ($J_{ph} \geq J_{sc}$).

2.6 Phase IV: Electrical performance

This section provides an in-depth analysis of the electrical performance of the Solarge cell stack using the sophisticated Fraunhofer SmartCalc.CTM software. This software is specifically designed for industrial-based module designs and enables accurate simulation of cell-to-module (CTM) performance.

To obtain reliable and precise results, it is essential to input specific parameters into the software. These parameters include various characteristics of the cell stack, such as material properties, dimensions, and electrical behavior. By providing these inputs, the software can generate valuable insights into the electrical performance of the Solarge cell stack.

Furthermore, to ensure the reliability of the simulation results, a validation is performed by comparing the simulated values with real-time measurements. This validation process serves as a verification to the accuracy and credibility of the software's predictions.

By utilizing the advanced capabilities of the Fraunhofer SmartCalc.CTM software and performing thorough validation, an assessment of the electrical performance of the Solarge

cell stack is obtained. This analysis aids in gaining a deeper understanding of the system's behavior and facilitates the identification of potential areas for improvement.

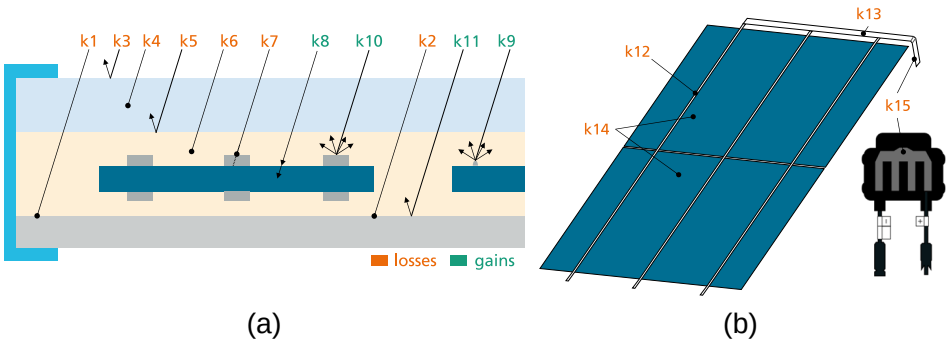

Figure 2.14: Losses and gains computed to obtain the cell-to-module performance. (a) loss-gain k factors for cell and module layers. (b) loss-gain k-factors for module and junction box. [67]

The software tool utilizes input parameters as shown in table A.2.3, A.2.4 and A.2.5 to calculate specific loss and gain factors known as k-factors, as depicted in Figure 2.14(a) and (b). These k-factors play a crucial role in estimating the cell-to-module performance of the given cell.

2.6.1 Roadmap

Figure 2.15 shows the procedure to conduct a cell-to-module analysis. As seen from the figure, six input parameters are required to run a successful CTM simulation. These input parameters can be segregated into three main portions such as the module layout, cell and interconnection information and optical information. The method of determining these input parameters are as follows:

1. **Cell and interconnection information:** The cell information is acquired by the supplier of the cells via the datasheet. In this study, two types of cells have been used: one a full G1 mono PERC cell and a half cut G1 mono PERC cell. The reason for this will be elaborated in the further upcoming sections. The interconnections used for the cells and strings are standard 1×0.25 rectangular ribbon and 5×0.4 rectangular serial connection respectively.

2. **Module layout:** This information is obtained from Solarge to simulate their standard 72 cell G1 modules.

3. **Optical information:** The optical information such as the layer optical properties and the layer thickness are obtained by using measurements and GenPro4 simulations as explained in the previous sections.

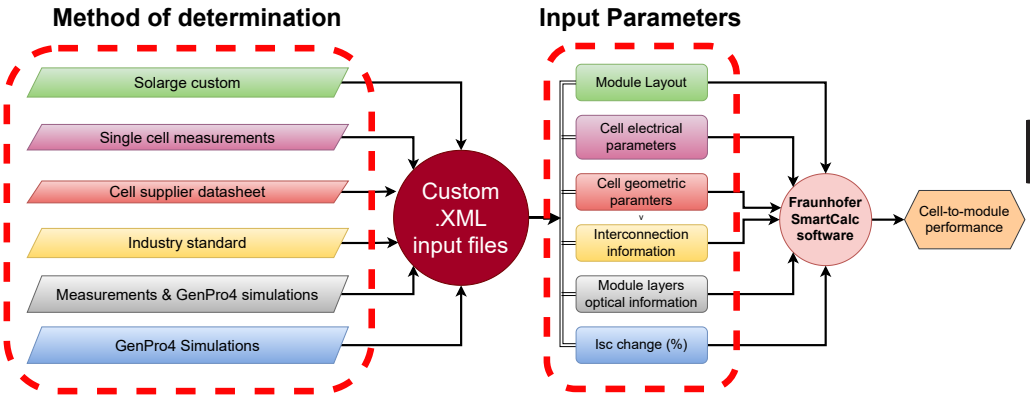

Figure 2.15: Input parameters for the Fraunhofer SmartCalc.CTM analysis

All input parameters described in Figure 2.15 are estimated and simulated using experimental and computational methods, as detailed in Appendix A.2.4 and A.2.5.

2.6.2 Electrical performance of a flat Solarge cell stack - Measurements

In this section, the Fraunhofer SmartCalc.CTM software is validated against a single cell laminate via electrical measurements. A half-cut cell is used with a flat front sheet and the electrical performance of the cell laminate is enumerated by figure 2.16 and by table 2.3. In order to assess the impact of optical losses on the overall losses in the cell laminate, precise measurements are crucial. Analyzing Figure 2.16 (b), we can calculate that the power output from a flat single cell laminate is 2.55W, representing a 9.57% reduction compared to the bare cell power output under STC conditions. This power drop can be attributed to two primary factors: optical losses and interconnection losses. While both are significant, this thesis focuses primarily on optical performance and therefore emphasizes the identification of the portion of loss caused by the optical polymer layers. To facilitate this analysis, the Fraunhofer SmartCalc.CTM tool proves invaluable as it provides a convenient means to determine the contribution of optical losses within the overall system losses.

Table 2.3: Electrical performance of a flat single cell laminate

Electrical parameters	Values
J_{sc} (mA/cm^2)	38.17
V_{oc} (V)	0.67
P_{max} (W)	2.55
Fill Factor (%)	78
Efficiency (%)	20.05

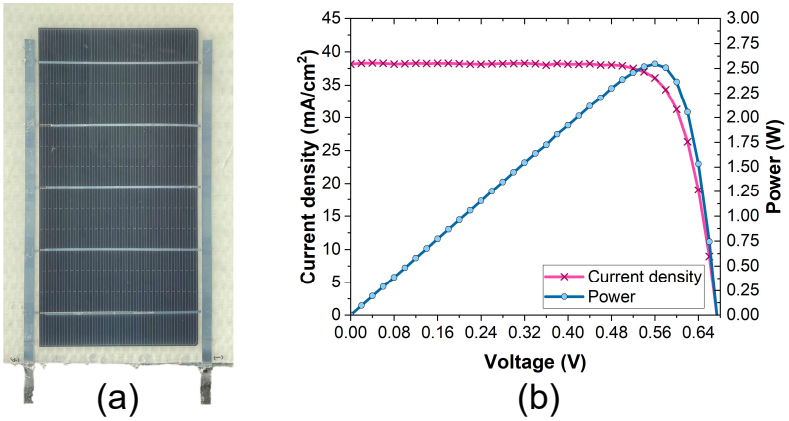

Figure 2.16: (a) Halfcut single cell flat laminate (b) Variation of power and current density as a function of voltage.

2.7 Phase V: Current Optical Losses

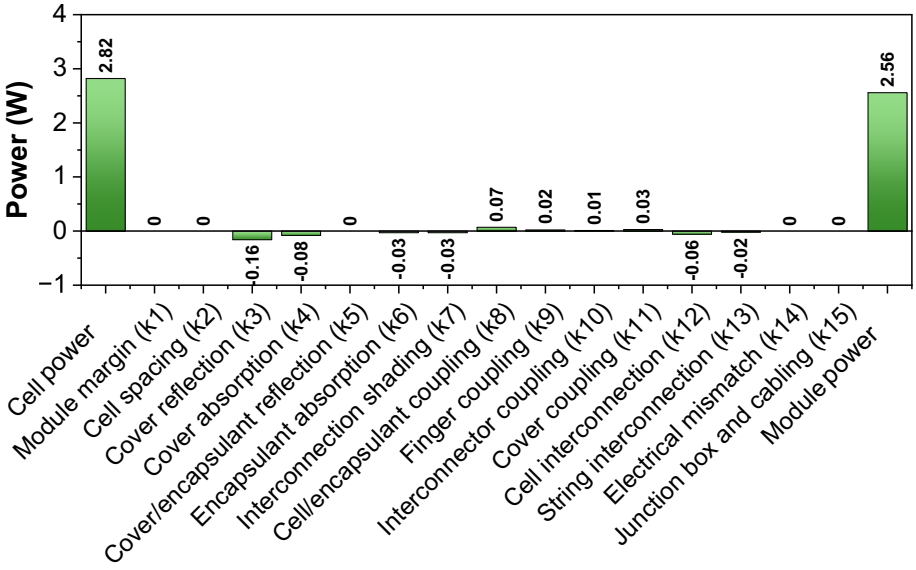

Figure 2.17: Cell-to-module analysis of a flat single cell laminate.

In this section, the simulation from the Fraunhofer smartcalc.CTM is explained. The validation of the simulation is done with respect to the power output of an experimentally measured single cell laminate as shown in the previous section. Figure 2.17 shows the CTM analysis for a flat single cell laminate. This analysis provides a clear overview of the losses in the system ultimately leading to the laminated power output. Firstly, it can be noted that the power output predicted by the software (P = 2.56W) is only 0.4% higher than

the measured result which showed the power of the flat cell stack to be P = 2.55W. This hence ensures that the simulations are in good agreements with the measurements and the results from the software is reliable.

Now, the next step is to estimate the contribution of optical losses in the module. Equation 2.6 is used to estimate the total optical losses in the system.

$$\textbf{Optical power loss} = \left|(k_3 + k_4 + k_5 + k_6 + k_7)_{optical\ loss} - (k_8 + k_9 + k_{10} + k_{11})_{optical\ gain}\right| = \underline{\mathbf{0.17W}} \quad (2.6)$$

$$\%\ Optical\ loss = \frac{optical\ power\ loss}{Cell\ power} = \frac{0.17}{2.82} = \underline{\mathbf{6.03\%}} \quad (2.7)$$

2.8 Conclusions

This chapter effectively addresses the second research question related to the characterization of polymer materials and the understanding of the optical performance of the Solarge stack.

Addressing the research question

(a) **What techniques are available for measuring the thickness of individual polymer layers?**
The technique used to evaluate the thickness of the polymer layers is derived from the ASTM standard guide for "Determination of Thickness of Plastic Film Test Specimens." In this approach, a micrometer with a least count of ±0.001 mm is employed as a reliable indicator to measure repeatable thickness values. This technique ensures accurate determination of individual polymer layer thickness, contributing to the overall understanding of the structure and optical performance of the Solarge stack.

(b) **What methods can be used to accurately determine the optical properties of polymer materials?**
To effectively characterize polymer materials, various methods and instruments are employed. One commonly used tool is the spectrophotometer, which enables accurate measurement of the optical properties such as reflectance, transmittance, and absorptance. Additionally, SCOUT and Genpro4 software are utilized to analyze and extract key optical parameters from the measured data. These instruments and software provide valuable insights into the optical behavior of polymer materials and aid in their characterization.

Addressing the research question (continued)

(c) **How can the current optical performance of a Solarge stack be comprehended?** The optical performance of the Solarge stack is analyzed using integrated optical models. By considering the properties of the front sheet, encapsulant, and solar cell, various parameters such as reflectance, transmittance, absorptance and photocurrent density are evaluated. This holistic approach provides a deep understanding of the stack's optical performance and enables optimization strategies for improved efficiency.

(d) **What approaches can be used to determine the overall optical losses in terms of electrical parameters?** The evaluation of overall optical losses in the Solarge cell stack involves a combination of experimental and computational results. The optical model generated by Genpro4 is utilized to calculate an essential factor, the I_{sc} change, which is required for the electrical simulation using the Fraunhofer SmartCalc.CTM software. By incorporating this value along with other input parameters, the SmartCalc.CTM software predicts the cell-to-module performance and identifies the mechanisms causing power losses in the module. These mechanisms contribute to a reduction in module power compared to the cell power. Through this simulation, the overall optical losses in the Solarge cell stack are determined.

In this chapter, several research questions pertaining to the characterization of polymer materials, accurate determination of optical properties, measurement of layer thickness, understanding the current optical performance of the Solarge stack, and evaluation of overall optical losses in terms of electrical parameters have been addressed. The optical and electrical models presented in this chapter have been validated using experimental data, providing valuable insights and methodologies for optimizing Solarge module designs and improving their power generation efficiency. These findings lay the foundation for Chapter 3, where the incorporation of textures will be discussed in further detail. By building upon the knowledge gained in this chapter, Chapter 3 aims to enhance the performance of Solarge modules through texture optimization where the ultimate goal is to reduce the overall optical losses from 6.03%.

3

Textures

This chapter addresses the third research question of the thesis, which focuses on methods of fabricating textures on the Solarge front sheet. Two fabrication methods namely, release papers and Teflon sheets, are explored. Experimental testing is conducted on various texture morphologies applied to the front sheet, and the textures are filtered based on the peel test results. From the selected textures sourced from company [A] and company [B], five options are chosen for imprinting on single cell laminates. These textures then undergo optical and electrical characterization to evaluate their performance. Building on the findings from the initial texture analysis, a set of requirements is defined to guide further investigations to explore the best performing texture for the Solarge cell stack. A computational study is then conducted to simulate scaled-up bio-inspired textures, as well as other textures such as random pyramids and corner cubes. By employing GenPro4, the optical properties of these textures are accurately simulated and analyzed. Based on the results of the initial texture analysis and simulations, two texture geometries are recommended to Solarge. Further optimization is performed on these textures, with one recommendation being fabricated on a single cell level, while the other is based solely on simulation results. The implementation of the first recommended texture leads to a significant increase of 2.65% in power output when compared to current Solarge cell stack. To provide a holistic perspective, a simple financial analysis is performed to assess the potential profitability of implementing the recommendations provided in this thesis. This analysis helps evaluate the economic feasibility and potential benefits for Solarge. By systematically investigating different fabrication methods, evaluating various texture morphologies, and conducting simulations and optimizations, this chapter presents extensive findings that contribute to the overall goal of enhancing the performance and thereby reducing the overall optical losses in the Solarge cell stack.

3.1 Introduction

This chapter is dedicated to addressing the issue of front surface reflection in Solarge's PV module through the implementation of texturing on the front sheet. Extensive measurements and simulations have revealed significant optical losses resulting from this phenomenon. To mitigate these losses, the incorporation of a light trapping texture is considered the most effective approach.

The main objective of this chapter is to minimize overall stack reflection in the Solarge cell stack by introducing appropriate textures. The performance analysis is conducted at various angles of incidence to assess the effectiveness of different textures. The ultimate goal is to provide Solarge with recommendations and suggestions to optimize their current cell stack, leading to enhanced power output and reduced optical losses.

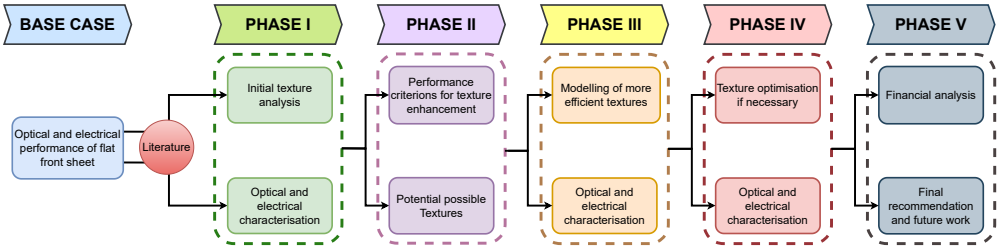

Figure 3.1: Roadmap to Chapter 3

To achieve the goal of optimizing the overall cell stack structure of Solarge, a systematic flow process is followed in this chapter. The chapter is divided into six distinct phases, each serving as a stepping stone towards the ultimate objective. The organization of the chapter is as follows, as depicted in Figure 3.1:

1. **Base Case:** In this phase, an initial analysis is conducted using a flat front sheet as a base case. The objective is to perform an angle-dependent study to evaluate the current optical losses in the Solarge cell stack. This analysis serves as a reference point for comparison with subsequent phases.

   The optical and electrical simulations for the flat cell stack have been validated in Chapter 2, ensuring the accuracy and reliability of the computational results. In this section, the simulations are performed using Genpro4 and the Fraunhofer Smartcalc.CTM software. The computational results provide valuable insights into the optical behavior and electrical performance of the flat cell stack configuration.

2. **Phase I:** In this phase, subsequent to establishing the base case, a rigorous examination is conducted on specific textures sourced from the organisation company [A], aimed at assessing their impact on both optical and electrical properties.

3. **Phase II:** In this phase, the performance criteria for efficient textures are established based on the results obtained in Phase I. These criteria serve as benchmarks for evaluating potential textures that demonstrate improved optical performance compared to the previously tested company [A] textures. An extensive review of relevant

literature is conducted to identify textures that exhibit promising characteristics. The selected textures are further analyzed and evaluated based on their ability to meet the established performance criteria.

4. **Phase III:** The selected textures are modeled using GenPro4 to the desired scale, generating heightmap matrices that represent their surface topography. These heightmap matrices are utilized as input in GenPro4 to perform precise optical simulations. By conducting angle-dependent optical simulations, the performance of the textures is thoroughly evaluated, considering various incident angles. This assessment provides insights into the optical behavior of the textures and their effectiveness in reducing front surface reflection.

5. **Phase IV:** In this phase, the most promising texture identified from Phase II and Phase III is selected as the basis for further optimization. The objective is to fine-tune the selected texture to align it with the desired operational requirements, aiming for an overall improved performance of the Solarge cell stack.

   The optimization process involves several aspects, including optimizing the layer thickness and enhancing the reflectance of the backsheet. By carefully adjusting these parameters, the aim is to maximize the light-trapping efficiency of the texture and minimize overall optical losses in the system. This fine-tuning process plays a crucial role in achieving an optimized and efficient cell stack configuration.

6. **Phase V:** The final phase of this chapter entails conducting a financial analysis for Solarge to assess the overall impact of the power increase in terms of monetary gains. This analysis aims to provide an overview of the financial implications and benefits that can be derived from implementing the recommended optimizations.

Through the systematic roadmap presented in this chapter, the primary objective is to provide Solarge with valuable recommendations and optimized solutions to enhance the optical and electrical performance of their cell stack. The focus is on reducing the overall optical losses in the system. By addressing key aspects such as texture design, material properties, and performance analysis, this chapter aims to provide actionable insights to improve the efficiency and power output of Solarge's PV modules.

3.2 Base Case: Angular dependent study of flat Solarge stack

In this section, the base case is subjected to a thorough analysis encompassing both optical and electrical characterization. The objective is to examine the influence of the incidence angle on various properties, which will be visually depicted and extensively discussed. This examination will provide valuable insights into the behavior and performance of the system under different angles of incidence. The GenPro4 software was used to conduct angle-dependent studies, providing optical performance data across a range of angles rather than a single angle. In the GenPro4 settings, (S.nai = 18), each value from 0 to 18 corresponds to an increment of 5°. To validate the results, singular angles were simulated using the GenPro4 settings (S.nai = 90), where each value from 0 to 90 represents an increment of

1°. Upon comparing the results obtained from these two settings, it was observed that the difference in optical outcomes was minimal. Considering the computational time involved, the angle settings with a 5° increment were adopted for the remaining simulations. A more detailed explanation can be seen in appendix A.3.1.

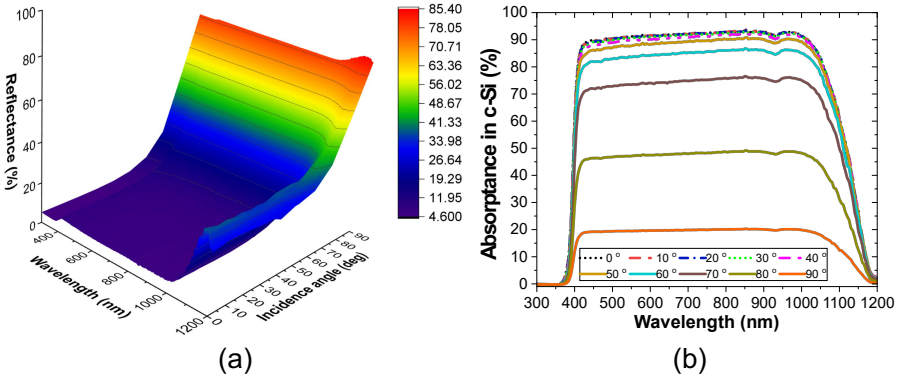

Figure 3.2: Optical performance - I. (a) Variation of total reflectance with incidence angle. (b) Influence of incidence angle on the external quantum efficiency (EQE).

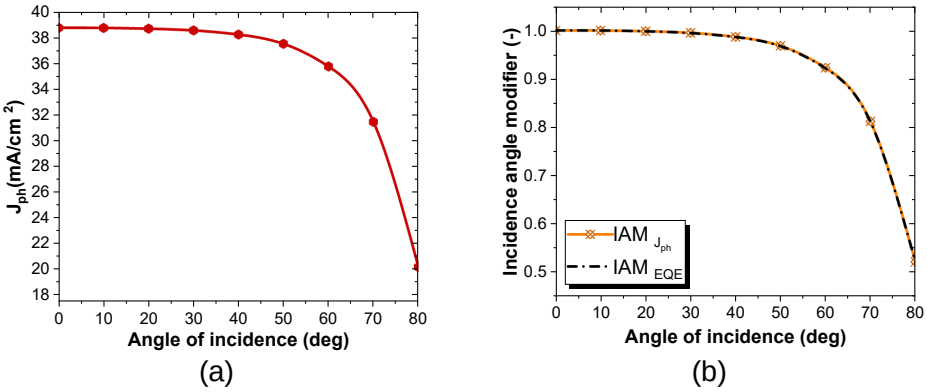

Figure 3.3: Optical performance - II. (a) Variation of photocurrent density with incidence angle. (b) Influence of incidence angle on Incidence angle modifier.

The initial analysis focuses on examining the impact of the angle of incidence (AOI) on both the total reflectance and the absorptance in the absorber layer of the flat stack. Figure 3.2 (a) illustrates the trend in total reflectance, indicating a substantial increase with AOI. This rise in reflectance adversely affects the efficiency of the flat stack. Meanwhile, Figure 3.2 (b) demonstrates the variation of the c-Si absorptance. Notably, the EQE remains relatively stable until an AOI of 30°, after which it exhibits a significant decrease from 40° to 90°.

The next parameter to look into is the variation of the photocurrent density (J_{ph}) at different angles of incidence as shown in figure 3.3 (a). The trend follows the EQE as per definition and the maximum value of (J_{ph}) is at normal irradiance ($AOI = 0^{\circ}$) and it reduces slightly until 30° after which the decrease is significant. Another parameter which provides a good insight into the angle dependency is the incidence angle modifier as shown in figure 3.3 (b), also known as the angle of incidence correction factor. This is a parameter used to describe the reduction in light intensity as the angle of incidence deviates from the perpendicular.

The significance of the incidence angle modifier lies in its ability to accurately assess the impact of the angle of incidence on the performance of solar cells or other optical devices [68]. In this study, the concept of *IAM* is used to check the dependence of two parameters with respect to incidence angle - *EQE* and J_{ph}. Equation 3.1 is used to calculate the required parameters [69].

$$IAM(\theta_i) = \frac{EQE\ (\theta_i)}{EQE\ (\theta_i = 0)} = \frac{J_{ph}\ (\theta_i)}{J_{ph}\ (\theta_i = 0)} \tag{3.1}$$

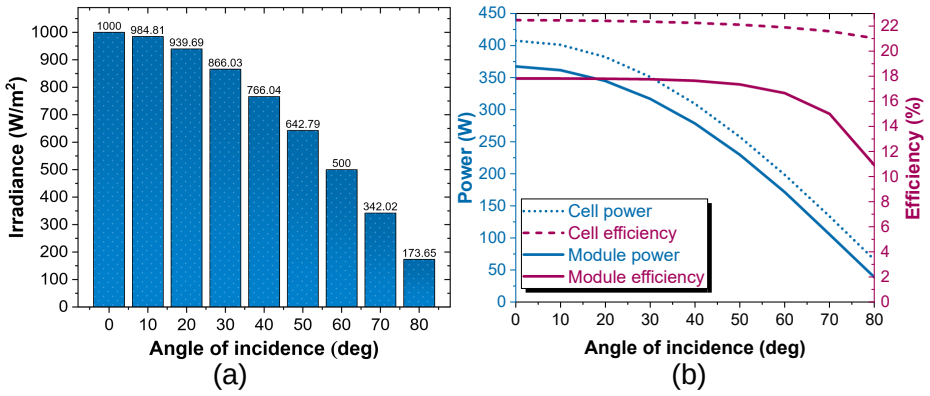

Figure 3.4: Electrical performance - I. (a) Variation of direct normal irradiance with incidence angle. (b) Influence of cell-module power and efficiency on incidence angle.

Using the above optical performance, a better understanding of a flat Solarge module can be understood by performing an electrical characterisation at a module level. To note, these results are obtained via electrical simulation using the Fraunhofer Smartcalc.CTM software. Figure 3.4 (a) shows a plot with direct normal irradiance at different angles of incidence. In this case a diffuse component is not considered to compare two different computational platforms. Figure 3.4 (b) showcases the results of the cell-to-module analysis. It can be noted that firstly the module efficiency drastically drops after 60° due to high reflective losses of the flat front sheet.

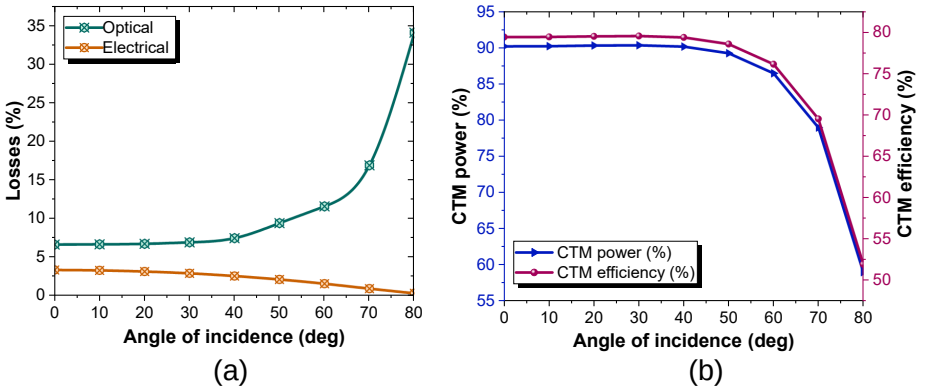

Figure 3.5: Electrical performance - II. (a) Variation of overall losses with incidence angle. (b) Influence of cell-module power and efficiency on incidence angle.

The evaluation of losses in the system is crucial to gain a vast understanding of the performance. Figure 3.5 (a) provides insights into the overall losses in the system, specifically in terms of CTM power output. Optical losses play a significant role in the total losses, especially at higher angles of incidence, compared to electrical losses. It is evident that the optical losses increase significantly beyond $\theta_i = 30^\circ$ when a flat front surface is used in the Solarge cell stack. This indicates that the system exhibits angle in-dependency only up to $\theta_i = 30^\circ$, highlighting the need for implementing textures that can delay the rise in optical losses at higher angles of incidence, thereby improving the overall performance across a wide range of incidence angles. The primary cause of these losses is total reflection occurring at the air/front sheet interface of the solar module. By implementing front surface texturing, these effects can be mitigated effectively.

Figure 3.5 (b) presents the cell-to-module ratio (CTM), which elucidates the relationship between the power or efficiency of an individual solar cell and the overall power or efficiency of the module. This ratio provides valuable insights into the overall performance and efficiency of the module.

The distinction between CTM power (%) and CTM efficiency (%) arises from multiple factors. CTM power (%) considers the total power output of the module, accounting for losses during the conversion process such as resistive losses, shading effects, electrical mismatch between cells, and other electrical losses within the module. Consequently, variations in CTM power (%) occur due to these losses at different angles of incidence.

In contrast, CTM efficiency (%) quantifies the module's conversion efficiency by comparing the electrical power output to the incident solar power. It focuses specifically on the efficiency of converting solar energy into usable electrical power. Factors like non-uniformity in cell performance, cell mismatch, and optical losses due to the angle of incidence can influence the efficiency.

Therefore, from figure 3.5 (b) it can be concluded that the optical losses overpower other losses at higher angles of incidence and hence this calls the need to improve the overall optical performance of the Solarge cell stack.

3.3 Phase I: Initial texture analysis

In this section, an extensive assessment is undertaken to evaluate the optical and electrical enhancements achievable by incorporating a variety of textures obtained through a mutual collaboration with the companies [A] and [B]. A meticulous selection process identified 10 potential textures for thorough analysis. Notably, 8 of these textures are procured from company [A], a reputable supplier renowned for their specialized offerings in textured casting and release papers. Additionally, two textures are acquired from company [B], a trusted provider of high-quality PTFE-products, specifically two grades of Teflon. In this section, the focus is on the experimental characterization of the textures, as the availability of accurate 3D heightmaps for the textures used limits the inclusion of simulation aspects. Instead, experimental techniques have been employed to assess the overall performance of the textures. This approach ensures that both experimental and computational results are compared on the same basis, despite the absence of simulation data. The experimental characterization provides valuable insights and reliable data for evaluating the effectiveness of the textures in enhancing the optical and electrical performance of the Solarge cell stack, thereby compensating for the unavailability of simulation results.

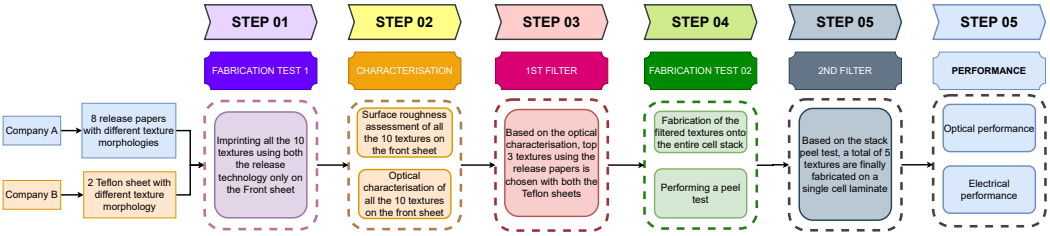

Figure 3.6: Overall methodology used to characterise textures used in phase I

In this phase, the methodology employed for texture selection, fabrication, and characterization is illustrated in Figure 3.6. Initially, a total of 10 textures (8 from company [A] and 2 from company [B]) were considered. The company [A] textures are applied on release papers, with each texture having a separate coating, while the textures from company [B] are hosted on a Teflon sheet. The first step involves imprinting the textures solely on the front sheet to evaluate their impact on optical and surface properties. Based on the characterization results, the top three performing textures from the company [A]'s repository and the two textures from company [B] were selected, reducing the number of textures for further analysis to five.

Subsequently, these five selected textures were fabricated with all the layers comprising the Solarge cell stack. An important observation was made during the peel test conducted after the lamination and imprinting processes. Based on the peel test results, a second round of filtering was performed, further refining the selection of textures. Finally, a set of five different textures (three other texures from company [A] and two same from company [B]) were fabricated as single-cell laminates, and their optical and electrical properties were evaluated.

This rigorous process ensures a systematic approach to texture selection, taking into account both the optical and electrical performance of the textures at each stage of the

evaluation. The final set of textures chosen for further analysis is based on their overall performance and suitability for integration into the Solarge cell stack.

3.3.1 Step 01: Fabrication test - I

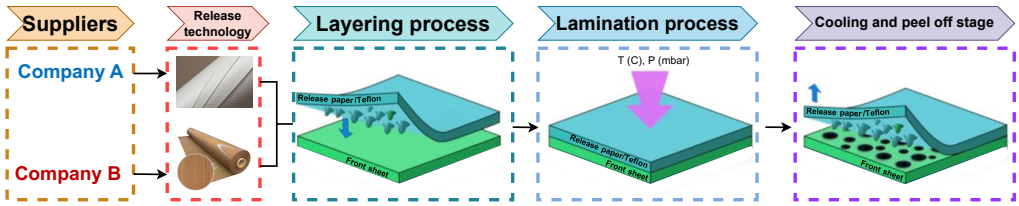

Figure 3.7: Process of imprinting textures on the front sheet of Solarge modules [70].

Figure 3.7 illustrates the process of imprinting textures onto a polymer surface. Initially, the master molds hosting the textures are obtained in the form of release papers from Company [A] and Teflon sheets from Company [B]. The subsequent step involves layering all the stack components in the prescribed order, with the release paper or Teflon sheet positioned atop the front sheet. Once the layering process is complete, the entire stack undergoes lamination in a vacuum laminator as explained in figure 2.2. This process applies a pressure of P_{lam} (mbar) while maintaining a temperature of T_{lam} (°C), causing the front sheet polymer to acquire the texture from the release paper or Teflon sheet. Following this, a cooling period of 10-25 minutes is provided which allows for the solidification of the polymers. Then, the peel-off process is then executed, whereby the positive textures on the release paper/Teflon sheet are transferred on the front sheet with the negative imprint (the release paper or Teflon sheet serves as a master mold, housing the positive impressions of the textures to be imprinted onto the front sheet).

Figure 3.8 showcases the textures that were successfully imprinted on the Solarge front sheet using the release paper or Teflon sheet provided by the respective suppliers. An important observation worth noting is that after the completion of the imprinting process, both the release paper and Teflon sheet could be peeled off smoothly from the front sheet, leaving behind a well-defined texture. This optimal peel-off process can be attributed to the non-adhesive nature of the front sheet, as explained in Chapter 2. However, it should be noted that this smooth peel-off may not be the case when all the layers of the stack are present during the imprinting process, as will be discussed in the subsequent sections.

With the front sheet samples containing the textures, the next step involves characterizing these textures in terms of surface roughness and optical properties. The surface roughness analysis provides insights into the topography and morphology of the textures, while the optical properties analysis allows for the evaluation of their impact on light scattering, reflection, and transmission. By closely examining these properties, a thorough understanding of the textures' physical and optical characteristics can be achieved.

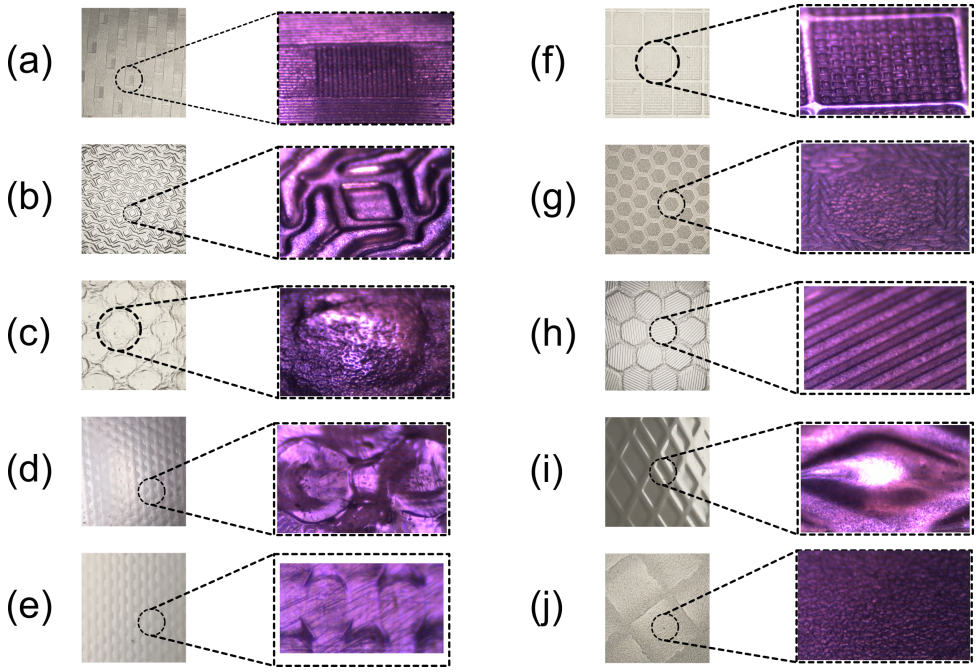

Figure 3.8: Textures imprinted on the Solarge front sheet. (a) texture-1. (b) texture-2. (c) texture-3. (d) Coarse Teflon. (e) Fine Teflon. (f) texture-4 . (g) texture-5. (h) texture-6. (i) texture-7. (j) texture-8

3.3.2 Step 02 & 03: Characterisation and first filter

Surface profile and roughness

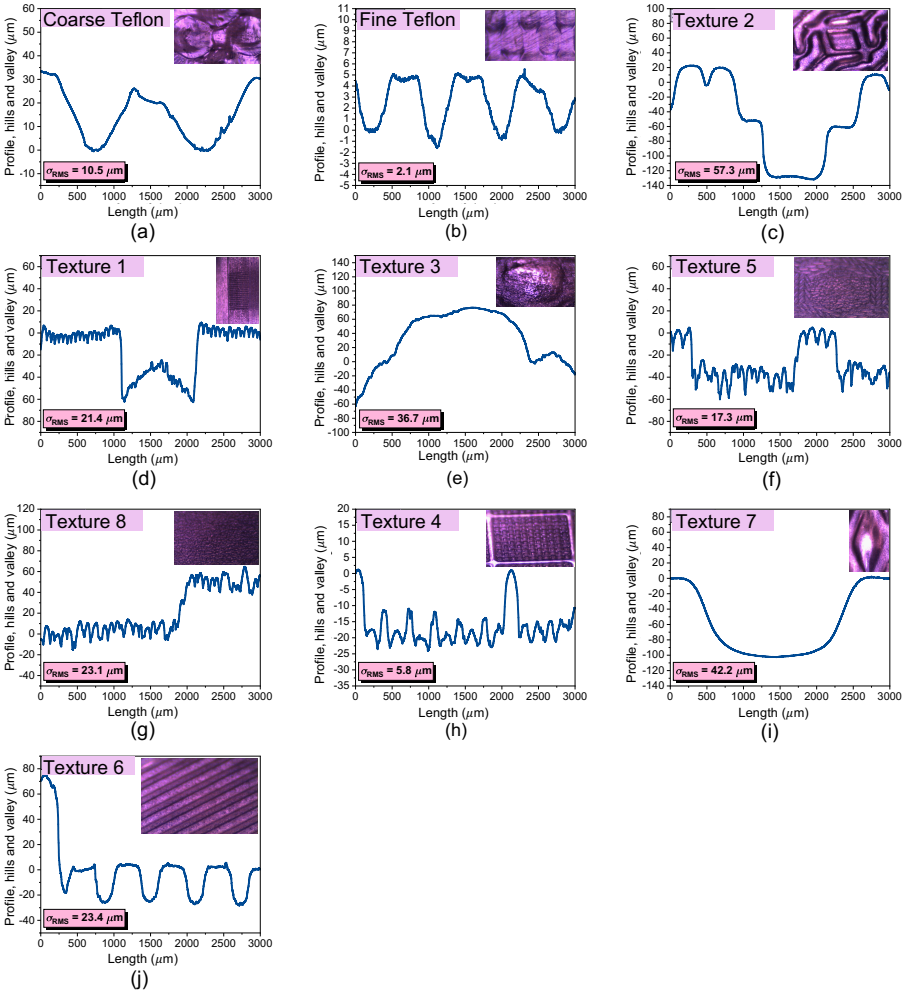

Figure 3.9: Surface roughness. (a) Coarse Teflon, (b) Fine Teflon, (c) texture-2, (d) texture-1, (e) texture-3, (f) texture-5. (g) texture-8, (h) texture-4, (i) texture-7, (j) texture-6.

This section aims to analyze and visualize the geometrical profiles of the selected textures using a Dektak surface profilometer. Figure 3.9 (a)-(f) illustrates the roughness profiles for each texture imprinted using the Company [A]'s release papers. Figures 3.9 (a) and (b) present the surface profiles of the coarse Teflon and fine Teflon textures on the Solarge front sheet, respectively. It is evident that the textures imprinted from the Teflon sheet exhibit a smooth inverted parabolic structures with varying aspect ratios. The aspect ratio plays a crucial role in the optical performance of the textures, as elaborated in the forthcoming

sections. Figure 3.9 (c) displays the profile of the texture-2 texture morphology, which exhibits a combination of upright and inverted geometries. On the other hand, Figure 3.9 (e) showcases texture-3, characterized by upright structures with varying low aspect ratios. It is important to note that the texture-3 hosts a randomised lattice distribution and the depicted structure selection is selected based on scanning viability of the equipment. Lastly, Figure 3.9 (d) illustrates the texture-1, where the hierarchical arrangement of nano-scale and micron-scale textures can be observed. This combination has the potential to facilitate efficient light scattering as discussed in the literature review in chapter 1, resulting in an enhanced optical properties. However, it should be noted that not all hierarchical textures yield improved optical performance, as it depends on the geometrical morphology of the micron-scale texture and its placement within the lattice.

Optical characterisation

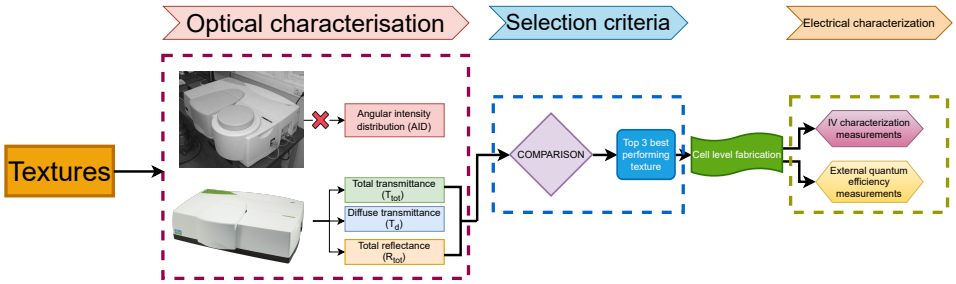

Figure 3.10: Selection methodology for the imprinted textures.

The selection methodology for determining the optimal texture for Solarge modules in terms of optical performance is presented in Figure 3.10. Initially, the textures are exclusively imprinted on the front sheet, excluding the other layers of the stack. Subsequently, the textured samples undergo characterization using the Perkin Elmer Lambda 950/1050 UV-Vis spectrophotometer. This characterization assesses the total transmittance, total reflectance, and diffuse transmittance. The evaluation of diffuse transmittance is particularly crucial for textured surfaces as it provides an estimate of extent of light scattering at normal incidence. Based on the measurements of diffuse transmittance, the top three textures with the best performance are selected and are tried to fabricate on a single cell level. Once the textures are successfully imprinted on the entire solar cell stack, the *EQE* (External Quantum Efficiency) and electrical performance of the stack are measured and analyzed.

Figure 3.11 presents the optical performance of the textured surfaces under normal incidence. Of particular interest is Figure 3.11 (a), which displays the diffuse transmittance of the textured surfaces. It is evident that the flat interface exhibits consistently low diffuse transmittance across the entire wavelength range, indicating minimal scattering from the flat surface. On the other hand, the measured textures demonstrate varying degrees of light scattering. Notably, the textures-8,1 and 5 exhibit the highest levels of diffuse transmittance, indicating their effective light scattering capabilities.

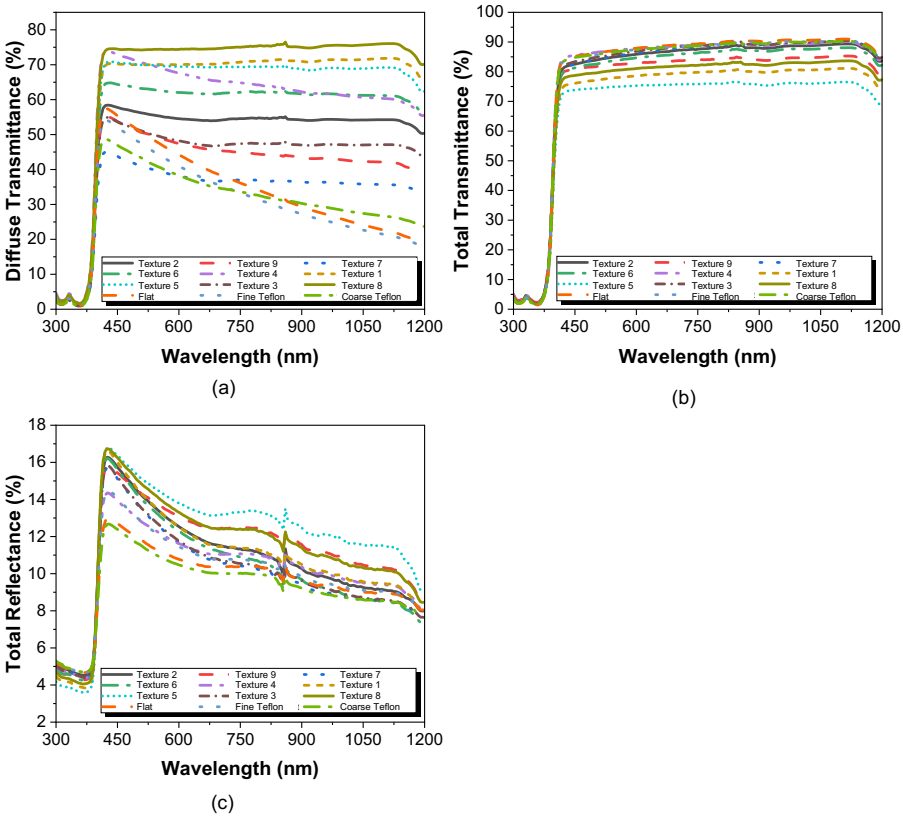

Figure 3.11: Optical performance of the front sheet with the textures imprinted using release paper technology. (a) Diffuse transmittance, (b) Total transmittance, (c) Total reflectance.

Figures 3.11 (b) and (c) illustrate the total transmittance and total reflectance of the textured surfaces. It is worth noting that textures with high diffuse transmittance also exhibit high total reflectance. This can be attributed to the layer structure (air/front sheet/air), which promotes multiple light bounces and scattering which is accounted as extra components of reflectane by the measuring equipment. However, when the complete layer stack is present, a portion of the scattered light and the rays bouncing off the textures reach the absorber layer instead of being solely reflected. Consequently, the total transmittance values indicate that the textures-8, 1 and 5 have lower total transmittance compared to, for instance, the fine and coarse Teflon sheets. This is because the total tramsmittance measures transmittance into air. This is different from, and therefore not a good measure for estimating the transmittance of textured samples in to the cell stack with all the layers.

Currently, Solarge utilizes the coarse Teflon sheet as the front surface texture for their modules, serving two purposes: (i) texturing the front sheet of the cell stack and (ii) ensuring no adherence of the modules to the laminator, as explained in Chapter 2. Notably, from the first plot, it is evident that both the fine and coarse Teflon sheets scatter less light compared to the textures from company [A]. Consequently, a preliminary conclusion drawn from

this section is that, without angular-dependent measurements, total transmittance and reflectance alone do not provide complete understanding of texture performance. Instead, measurements of diffuse transmittance offer valuable insights into the behavior of textured surfaces in terms of scattering.

Based on the results obtained from the diffuse transmittance measurements, the top three textures from the company [A]'s repository (textures-8, 1, and 5) and both the coarse and fine Teflon textures from company [B] are selected for further analysis. The next objective is to fabricate single cell laminates with these textures imprinted on the front sheet.

3.3.3 Step 04 & 05: Fabrication test - II and second filtering

This section provides an explanation of the second fabrication test, focusing on the impact of additional layers on texture imprinting quality. Initially, textures were exclusively imprinted on the front sheet, excluding the encapsulant, cell, and backsheet. However, this test aims to investigate the influence of these additional layers. The fabrication process follows the procedure depicted in Figure 3.7, with the inclusion of all stack layers during the imprinting process. During the test, two significant observations were made regarding the release technology employed:

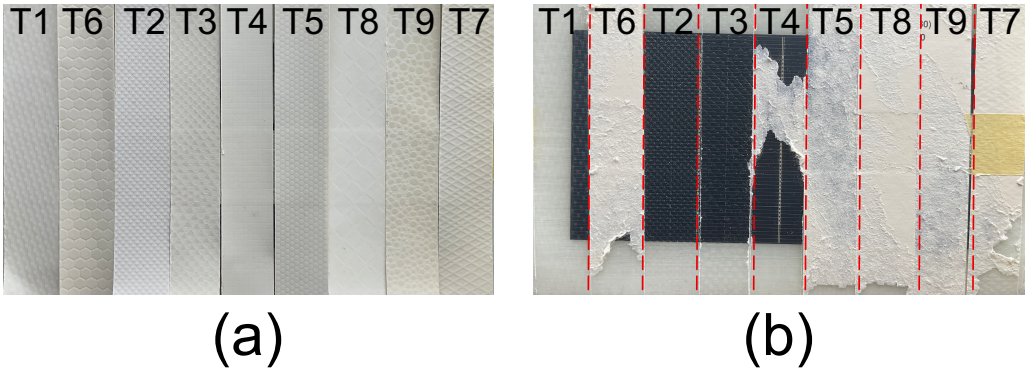

Figure 3.12: Peel test of release papers. (a) Release paper (master mold) with different textures. (b) Result of the respective peel off test.

1. **Observation 1:** Teflon sheets were identified as the most suitable release mechanism for the polymer materials in the Solarge stack. However, their limited texture features present challenges in achieving the desired optical and electrical performance.

2. **Observation 2:** Company [A]'s release papers utilize a coating process, wherein thin layers of a specific coating are deposited on a sheet of paper to create the required textures. Each texture geometry corresponds to a unique coating recipe. The presence of the encapsulant, cell and the backsheet during the imprinting process affects the behavior of this coating, leading to increased complexity in peeling off these textures compared to cases involving only the front sheet.

These observations provide valuable insights into the performance and behavior of different release mechanisms when integrated into the Solarge stack, thus contributing to the understanding of texture fabrication and selection.

Figure 3.12 illustrates the peel off test conducted to evaluate the suitability of different coating types for the current application. Figure 3.12 (a) displays the release paper with various texture coatings, while (b) showcases the resulting product after the peel off test post the imprinting process. It is evident that the type of coating on the release paper plays a crucial role in the imprinting process. Among the 8 textures tested, only three can be easily imprinted and peeled off. Specifically, texture-1,2 and 3 exhibit the most favorable characteristics in terms of ease of imprinting and peel off.

Additionally, an interesting observation was made during the experimentation phase. Release papers with texture-3 can be utilized for imprinting only once, as the peel off process becomes more challenging thereafter. On the other hand, the coating used in texture-2 and 1 enables multiple imprints without the need for replacement due to its exceptionally easy peel off process. Consequently, due to the limitations associated with peeling the release sheets from the cell stack, the optical and electrical performance evaluation was carried out solely for these three textures, in addition to two textures obtained from company [B] in the form of Telfon sheets.

As a result of the second filtering process, a total of five textures have been selected based on both their fabrication feasibility and the optical characterization performed in the previous section which are different from the initial selection. The five selected textures are as follows: texture-1, texture-2, texture-3, coarse Teflon, and fine Teflon textures. These textures have demonstrated promising performance and exhibit potential for improving the optical properties of the Solarge cell stack.

3.3.4 Step 05: Optical and electrical performance

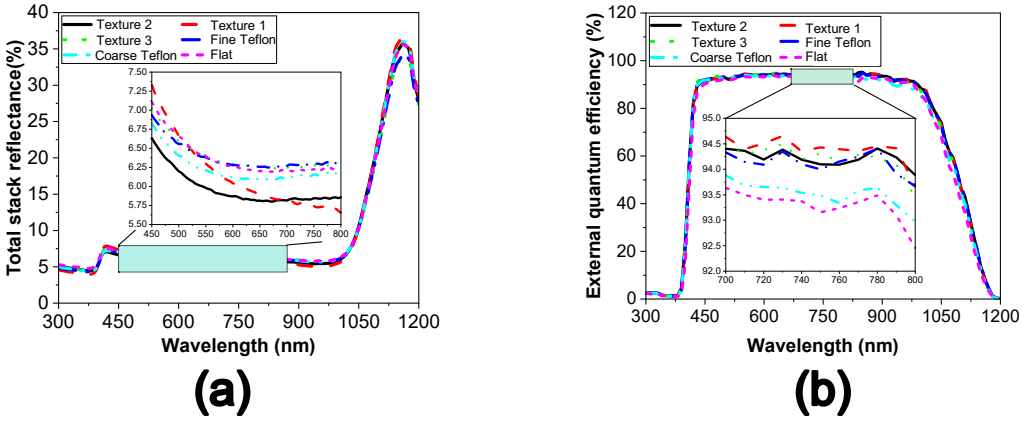

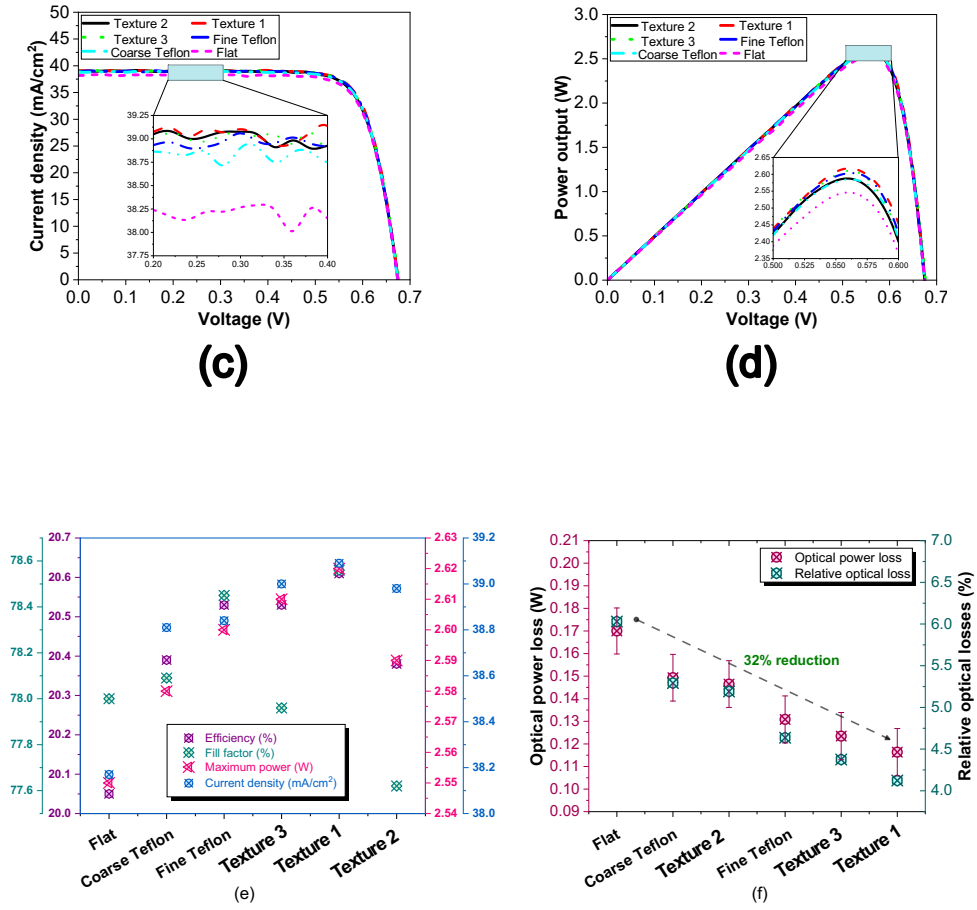

Figure 3.13: Optical and electrical performance of different texture morphologies. (a) Total stack reflection at normal incidence. (b) External quantum efficiency at normal incidence (%). (c) J-V curve. (d) power curve. (e) Four electrical parameters of the cell stack. (f) Comparison of optical power loss with different textures.

Based on the peel test results, the successfully imprinted textures are incorporated into single-cell laminates to assess their optical and electrical properties. Figure 3.13 provides an overview of the overall performance of the textures at normal incidence, considering both optical and electrical aspects. To evaluate the optical performance, Figures 3.13 (a) and (b) depict the total stack reflection and the external quantum efficiency (*EQE*), respectively.

From Figure 3.13 (e), it is evident that the cell stack with texture-1 exhibits a 2.4% increase in short-circuit current density compared to the flat cell stack, and a 0.7% increase compared to the cell stack with the coarse Teflon sheet. This improvement can be attributed to the reduction in average reflectance at the air/front sheet interface, where the reflectance with texture-1 is 2% lower than that of the flat cell stack, and 1.26% lower than that of the coarse cell stack. A more detailed analysis is facilitated by zooming in on the plot,

enabling observation of the trend exhibited by the textures. Notably, texture-1 demonstrates the highest reduction in reflectance. A similar trend is observed in the EQE, where the differences are not substantial, but a comparison between the textures can be made using the magnified version of the plot. In accordance with the predictions derived from the diffuse transmittance plots, texture-1 outperforms the other textures.

Table 3.1 provides quantitative analysis of the average total reflectance in the wavelength range of 300 nm - 1200 nm and the average EQE in the range of 450 nm - 1000 nm. As anticipated, the flat surface exhibits the highest total reflectance, while texture-2 demonstrates the lowest reflectance. Notably, texture-1 outperforms the other textures in terms of average *EQE*.

It is important to acknowledge that the small deviation observed in reflectance measurements, along with the trend observed in the reflectance curve, particularly in the wavelength range of 600 nm - 800 nm where the texture-1 outperforms texture-2, can be attributed to both the precision limitations of the measuring equipment and the overall trend of the reflectance curve. Therefore, considering both the trend of the reflectance curve and the average values provides a more broad understanding of the optical performance, rather than relying solely on a single parameter.

Overall, the combined analysis of reflectance and *EQE* data provides valuable insights into the optical performance of the textured surfaces, aiding in the selection and evaluation of the most promising texture for further investigations.

Table 3.1: Average optical properties

	Texture-1	Texture-3	Texture-2	Fine Teflon	Coarse Teflon	Flat
R_{avg}	9.40	9.39	9.34	9.37	9.52	9.59
EQE_{avg}	92.91	92.87	92.84	92.75	91.78	91.54

Figures 3.13 (c) to (f) provide a concise overview of the overall electrical performance of various texture morphologies. Figure 3.13 (c) and (d) present the J-V and P-V curves, respectively, offering valuable insights into the influence of surface texturing on the front polymer layer. The impact of optical properties on the short-circuit current density (J_{sc}) is evident, emphasizing the importance of maintaining a consistent operating temperature of 25°C for reliable and accurate results.

Zoomed-in plots reveal that texture-1 exhibits the highest J_{sc}, as evident from both the power curve and Figure 3.13 (e). The latter illustrates four essential parameters of the single cell laminate: maximum power, efficiency, fill factor, and current density. Notably, texture-1 outperforms the others across all four parameters, demonstrating its superior electrical performance.

Furthermore, assessing the overall optical losses in the system, as conducted in chapter 2, presents a final aspect of electrical characterization. However, the Fraunhofer smartCalc.CTM software used for this evaluation is not suitable for accounting for the effects of scattering resulting from front surface texturing. Therefore, a combination of computational and experimental results is employed to predict the overall optical losses. To

facilitate this calculation, certain assumptions are made, ensuring an exhaustive analysis of the system.

1. **Assumption 1:** The total interconnection losses remain constant across all the measured samples.

2. **Assumption 2:** The discrepancy between measurements and simulations, as discussed in Chapter 2, needs to be incorporated to account for the error range in the calculations.

Therefore, with these two assumption, the following equation can be used to evaluate the total optical losses in the system.

$$P'_{optical\ loss} = \underbrace{P_{bare\ cell}}_{2.82\,W} - \underbrace{P_{laminated\ cell}}_{Measured\ power} - \underbrace{P'_{interconnection\ loss}}_{0.088\,W} \tag{3.2}$$

Where P' denotes the power loss and P denotes the power generated. Similarly, the total percent optical loss can be evaluated using equation 2.7.

The calculation of overall optical losses and their impact can be observed in Figure 3.13 (f), which illustrates the optical power loss and the percentage of optical losses within the system. It is evident that the inclusion of textured geometries leads to a reduction in overall power loss. Among all the textures tested, texture-1 exhibits the lowest optical losses (4.12%), representing a 32% reduction compared to the flat front sheet (6.03%). This reduction highlights the effectiveness of texture-1 in minimizing optical losses and enhancing the overall performance of the system.

3.4 Phase II: Enhancing Texture Performance: Criteria, selection and validation

3.4.1 Texture criteria

This section emphasizes the potential enhancement of the textures tested as part of Phase I of this chapter. It explores the importance of front surface texturing and investigates the desired performance criteria associated with textures. Additionally, it examines the necessary conditions for implementing these characteristics. Once the requirements are identified, a thoughtful selection of textures is made based on their established performance as documented in existing literature.

Based on the results presented in the previous section, several mandatory properties are identified as necessary requirements for the textures. These properties include: Anti-reflective property, Light trapping, Angle insensitivity.

Analysis of the preceding sections on the performance evaluation of a flat Solarge module stack reveals a notable issue: the high level of reflection at the front air/front sheet interface necessitates significant reduction. Various approaches can be employed to incorporate anti-reflective properties, including single layer AR coating, multi-layer AR coating, gradient refractive index coatings, and structure-based surface AR coatings [71]. However, this work emphasizes the implementation of structure-induced anti-reflectance.

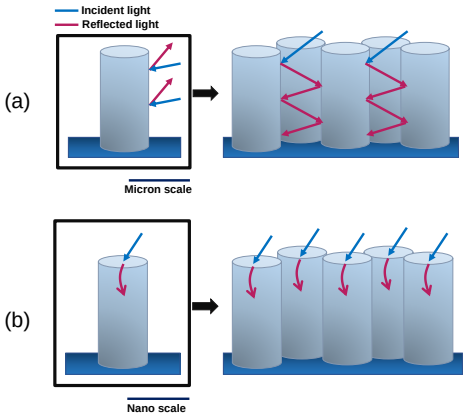

Figure 3.14: Light interaction with textures. (a) Multiple internal reflections through a micro-structure array. (b) Bending of light rays passing through a nano-structure array. Image revised from [71]

Figure 3.14 demonstrates the diverse behavior of light across different scales of the same texture. This distinction arises from light's dual properties, acting both as a ray and a wave. When the lateral dimensions of the textures greatly exceed the wavelength of light (i.e., in the case of micron-scale textures), light predominantly behaves as a ray, and its performance is evaluated using geometric optics. Conversely, when the dimensions of the textures are comparable to or smaller than the wavelength of light (i.e., in sub-micron and nano-scale textures), light interacts with the structure as a wave, necessitating the use of wave optics to understand the texture's behavior [72].

In this thesis, the objective is to simulate bioinspired textures by scaling up their geometrical parameters in the micron scale and evaluating their performance in GenPro4 using ray optics. This section provides an overview of various texture morphologies to assess the Solarge stack's performance with different textures, offering a wide range of options to choose from. Consequently, both texture geometries with sharp angles and textures with blunt corners are simulated, catering specifically to the requirements of the Solarge front sheet.

3.4.2 Texture validation

In order to validate the simulation results for different texture geometries, it is crucial to perform validation at various angles of incidence. For this purpose, texture-2 is chosen for validation due to the availability of its heightmap matrix from the supplier. However, other textures such as texture-1,texture-3, coarse Teflon, and fine Teflon cannot be modeled using GenPro4 due to the unavailability of their respective heightmap matrices. Attempts were made to measure the heightmap matrix using a Dektak surface profilometer, but it was observed that the resulting heightmap did not provide an accurate interpretation of the texture. This is because the surface profilometer measures height differences with respect to the mean base, whereas obtaining detailed 3D landscape requires manual scanning in both the x and y directions which induces human error and does not yield the best 3D map of the required texture. This process becomes complex and impractical for generating a

high-quality heightmap. Consequently, texture-2 is utilized for texture validation.

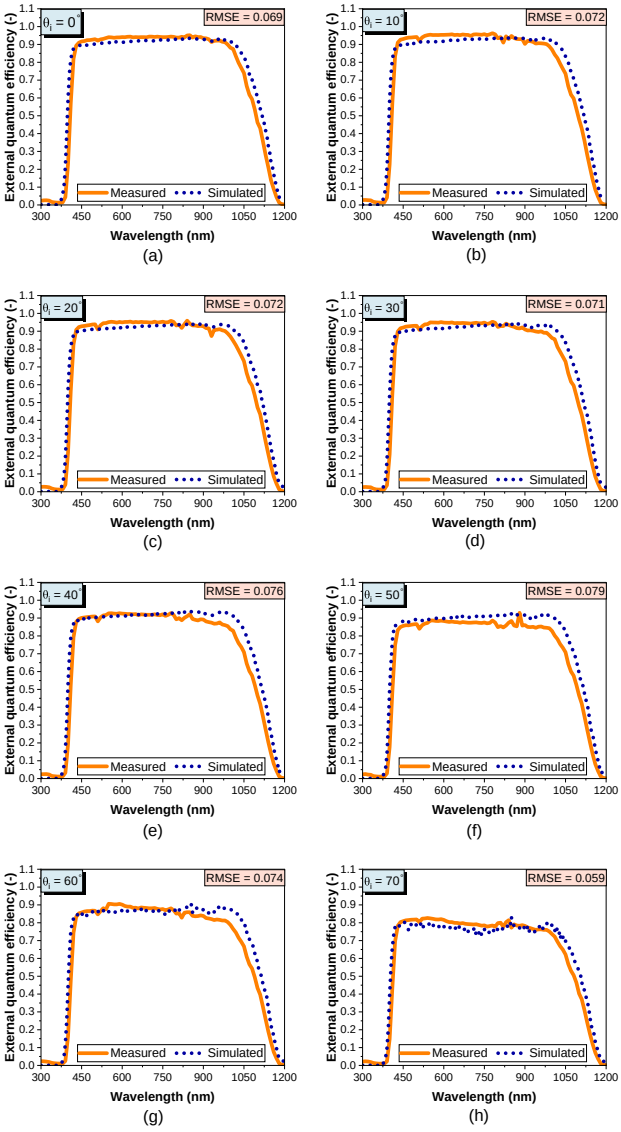

Figure 3.15: Texture validation - Comparison of the external quantum efficiency of texture-2 via measurements and simulation.

Four methods are usually employed to validate the texture simulation results against the measurements, which are as follows:

1. **Validation method 1:** Comparing the angular intensity distribution (AID).
2. **Validation method 2:** Comparing total stack reflection at normal incidence.

3. **Validation method 3:** Comparing the external quantum efficiencies (*EQE*) at varying angles of incidence.

4. **Validation method 4:** Comparing the photocurrent density from simulation and the short current density from measurements.

In this study, three validation methods (2, 3, and 4) are employed to assess the accuracy of the simulations. Unfortunately, Validation 1 cannot be conducted due to the unavailability of appropriate measurement instruments. Consequently, a complete analysis is performed by comparing the external quantum efficiency (EQE) and total stack reflection at normal incidence for the same texture geometry. Additionally, the simulated photocurrent density (J_{ph}) is compared with the measured short circuit current density (J_{sc}). Firstly, the results of validation method 3 is presented in Figure 3.15 (a)-(h). The validation is carried out for eight different angles of incidence, ranging from 0° to 70° in 10° increments. The plots exhibit a favorable agreement between the simulation and measurement data, indicating that the simulations accurately predict the performance of the textures within an acceptable error range. This is further supported by the root mean square error (RMSE) values provided in each plot.

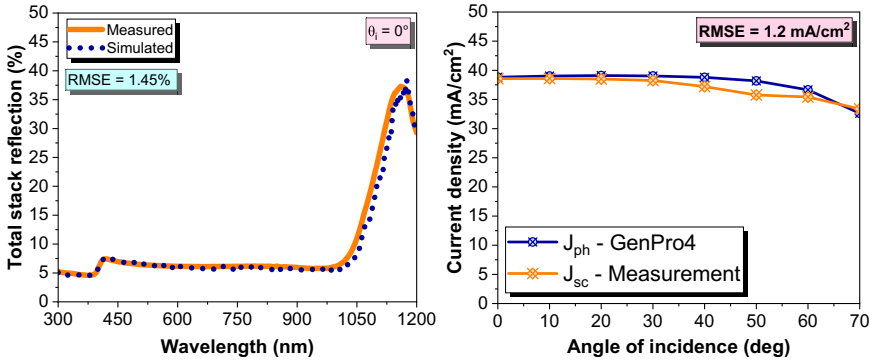

Figure 3.16: Texture validation. (a) Total stack reflection at normal incidence. (b) Comparison of simulated photocurrent density and measured short current density.

In addition to the *EQE* validation, the reliability of the optical model is further demonstrated through validation methods 2 and 4, as depicted in Figure 3.16. Figure 3.16(a) illustrates the comparison of the total stack reflection between the measured and simulated curves for texture-2. Notably, the close agreement between the measured and simulated curves confirms the accuracy of the optical model. Furthermore, Figure 3.16(b) presents the difference between the simulated photocurrent density (J_{ph}) and the measured short circuit current density (J_{sc}). It is observed that the simulated J_{ph} closely aligns with the measured J_{sc}, with a slight discrepancy observed at $\theta_i = 50°$, likely attributed to experimental errors. Overall, the simulated J_{ph} is higher than the measured J_{sc} in accordance with the theoretical expectations. The root mean square error (RMSE) between these two parameters is

1.2 mA/cm^2. However, excluding the abnormality at $\theta_i = 50^\circ$, the RMSE reduces to 0.74 mA/cm^2. Therefore, based on these three validations, it can be concluded that the optical model developed in this thesis projects a simulation which can be reliably compared to the real-time performance of the Solarge cell stack with different textured geometries.

3.4.3 Texture selection

Designing and implementing textures for PV module cover applications poses a challenge in achieving a balance of multifunctional features [40]. To address this challenge, this work adopts an approach that incorporates textures meeting the aforementioned requirements based on available literature. The aim is to ensure that the optical properties align with the desired geometrical characteristics of the textures. Table 3.2 provides an overview of the textures to be analyzed in this study, all of which satisfy the specified requirements.

Table 3.2: Potential texture geometries

LITERATURE BASED		
Surfaces	Texture geometries	Reference
Viola flower petal	Conical	[73, 74]
Motheye	Conical, parabolic	[75, 76]
Rosa el toro	Parabolic cone	[77]
Retroreflector	Corner cube	[78, 79]
Fovea centralis	Inverted cones	[80]
Lotus leaf	hierarchical conical structure	[70]
Default	Pyramidal textures	[81]
THIS WORK		
The crown	Inverted hexagonal parabola	[-]

The Crown texture

The investigation conducted in this thesis involves the modeling and simulation of various textures, as presented in Table 3.2, to assess their impact on the optical properties of the solar cell stack. Alongside the textures derived from existing literature, a custom texture is specifically designed in this study, considering the following priorities:

1. The peel-off test revealed that upright textures are challenging to remove from the polymer front sheet. Consequently, an inverted texture is deemed more suitable for this application.

2. Analysis of the initial texture and surface roughness underscores the difficulty in achieving sharp edges or corners when imprinting textures on a polymer. This challenge arises from the complexity of fabricating a master mold with sharp geometrical textures using paper or Teflon. Hence, a smooth texture without sharp geometric features is considered ideal in the viewpoint of manufacturing the textures.

3. Moreover, the initial texture analysis revealed that imprinting the Solarge front sheet using Teflon sheets is the most suitable method. Therefore, the concept is to preserve the unit shape of the Teflon while modifying the aspect ratio and lattice orientation.

Based on the three significant observations mentioned earlier, a new texture named "CROWN" is designed. The name is derived from the texture's resemblance to a crown, characterized by a hexagonal inverted parabola shape. The CROWN texture shares similarities with the textures found on the Teflon sheet, but with variations in the cross-sectional profile and aspect ratio. This unique design aims to optimize the optical performance of the texture, addressing the specific requirements identified during the evaluation of different texture geometries. The CROWN texture offers a promising approach to enhancing light trapping and reducing front surface reflection in the Solarge cell stack.

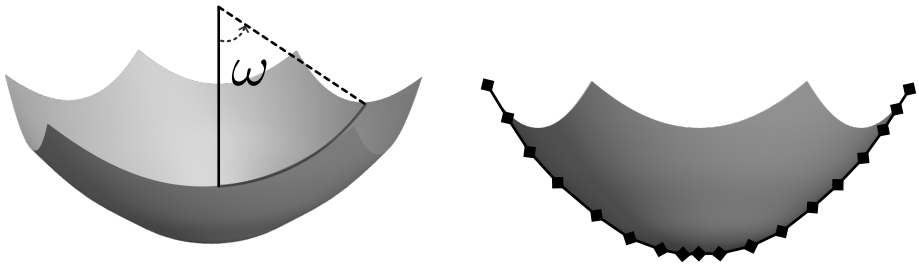

Figure 3.17: Unit geometrical texture of the CROWN texture.

Figure 3.17 provides a clear visualization of the texture's geometric structure. The structure follows a hexagonal inverted parabola with an optimized characteristic angle ($\omega = 50^{\circ}$) where the characteristic angle defines at which height two spheres intersect and leads to steeper sidewalls for larger values [82] . A polynomial equation is fitted to the cross-section of the texture (as shown in the figure with black dotted lines) to interpret the profile of the CROWN texture, yielding the following equation:

$$y\,(\mu m) = 0.0227 \cdot x^4 - 0.2088 \cdot x^3 + 1.4971 \cdot x^2 - 4.674 \cdot x + 6.3249 \tag{3.3}$$

3.5 Phase III: Modelling and performance of textures

This section builds upon the preceding sections and focuses on enhancing the optical and electrical properties of the Solarge stack, surpassing the performance of texture-1, which currently demonstrates the most favorable outcomes.

The main objective of this section is to examine specific bio-mimetic textures and assess their performance by scaling their geometries to the micron scale, as opposed to their natural nanometer regime. Additionally, other textures such as random pyramids, corner cubes, and sinusoidal textures are simulated to explore the influence of sharp angles compared to smooth surfaces on the Solarge cell stack.

To accomplish this, an improved workflow for modeling textures is explored, employing a simplified approach that obviates the need for coding intricate equations to define texture shapes. In order to simulate the optical performance of these textures using GenPro4, it is essential to generate texture geometries that can be represented by a height-map matrix on an XY plane. The generation of this height-map matrix constitutes a critical step in creating custom textures, providing the fundamental basis for subsequent simulations and analysis.

3.5.1 Methodology

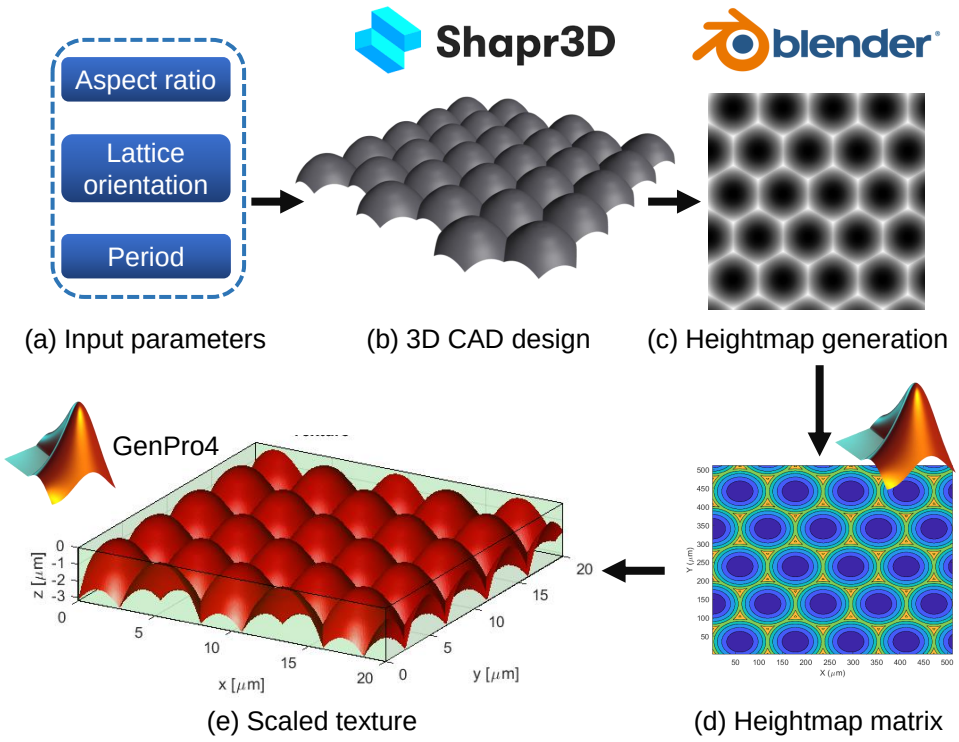

Figure 3.18: Texture modelling workflow. (a) Determining the geometrical input parameter. (b) 3D CAD design of the texture using Shapr3D. (c) Heightmap image using Blender. (d) Heightmap matrix using Matlab. (e) scaled texture geometry in Genpro4.

Figure 3.18 presents a methodology for creating a successful height-map for any texture geometry. The process begins by determining the essential input parameters, including the aspect ratio, lattice orientation, and period of the textures. Using CAD modeling software like Shapr3D, a 3D CAD model of the texture geometry is created as shown in figure 3.18 (b).

The CAD model is then exported to Blender, an open-source software, where it is transformed into a height-map image as shown in figure 3.18 (c). This conversion in-

volves projecting the 3D model onto a 512 $px \times 512$ px pixel-based frame where each pixel represents the height of he texture at that particular point in space.

Next, the height-map image is processed in MATLAB, where it is transformed into a height-map matrix and scaled to the desired dimensions as shown in figure 3.18 (d). This height-map matrix serves as the input for GenPro4, enabling the simulation of the optical performance of the cell stack with the specific texture type as shown in figure 3.18 (e).

By following this methodology, the entire workflow from texture modeling to optical simulation is effectively executed, providing valuable insights into the performance of the Solarge stack with various texture geometries.

3.5.2 Geometrical design and performance

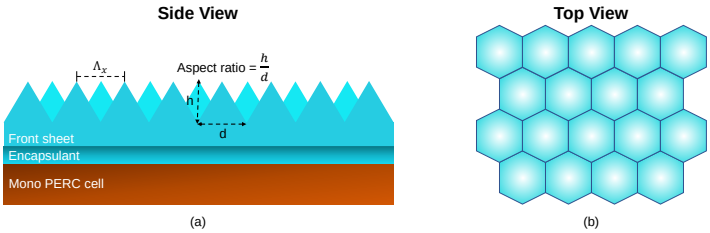

Figure 3.19: Geometrical input parameters

In this study, the geometrical parameters for the textures are primarily derived from research articles, which are referenced in Table 3.2. The chosen period of the textures is scaled based on the placement of unit texture geometries on the hexagonal lattice, while the lattice arrangement is fixed as hexagonal due to its numerous advantages. These advantages include increased light trapping through scattering and redirection, reduced shadowing effects for more uniform exposure to sunlight, and enhanced angular response for efficient light capture from various orientations, ultimately leading to improved solar cell performance. The efficacy of the textures is influenced by the aspect ratio of a unit geometry, with a stronger dependency observed at higher angles of incidence. To evaluate this influence and determine the optimal aspect ratio, this study employs optical simulations at a normal angle of incidence for five different aspect ratios (AR - 0.2, 0.35, 0.5, 0.7, 1) corresponding to the respective geometries. By performing these simulations, the research aims to gain insights into the impact of aspect ratio and make an informed selection of the most effective value for the desired outcome.

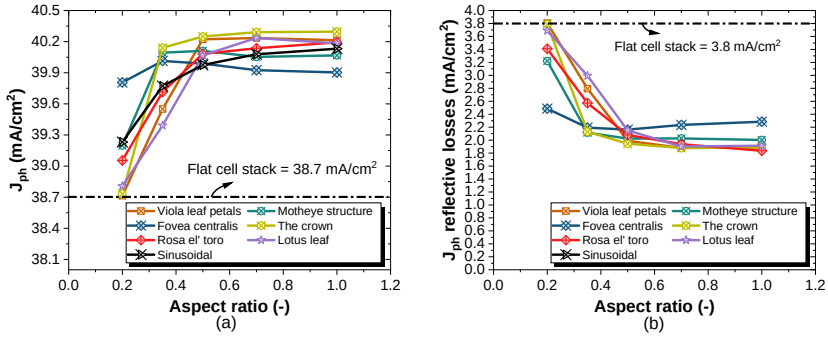

Figure 3.20: Influence of aspect ratio on the optical performance of the cell stack at normal irradiation. (a) Variation of overall photocurrent density with aspect ratio. (b) Loss in the photocurrent density due to reflection as a function of change in aspect ratio.

Figure 3.20 provides an analysis of the performance of biomimetic textures at a normal angle of incidence ($\theta_i = 0$). Figure 3.20 (b), showcases the loss in potential photocurrent density within the cell stack. Notably, even at the lowest aspect ratio, all textures outperform the flat-surfaced front sheet. This can be related to the coarse Teflon texture which has a very low aspect ratio which results to minimal boost in performance. The loss due to reflection stabilizes after a certain aspect ratio, indicating a limited enhancement in the optical path length.

Figure 3.20 (a) offers valuable guidance for selecting aspect ratios, presenting the photocurrent density for all textures. The trend reveals a significant increase in J_{ph} until a specific aspect ratio is reached, beyond which it experiences only marginal growth, suggesting a relatively constant behavior. This analysis aids in the informed selection of aspect ratios for the biomimetic textures, considering the trade-off between enhanced performance and practical implementation.

Table 3.3: Selection of geometrical parameters

	Jph losses (mA/cm^2)					Photocurrent density (mA/cm^2)					Selected Aspect ratio	Period (um)
Aspect ratio	0.2	0.35	0.5	0.7	1	0.2	0.35	0.5	0.7	1	(-)	(-)
Viola leaf petals	3.81	2.80	1.99	1.88	1.89	38.71	39.55	40.22	40.23	40.21	0.7	2.50
Motheye structure	3.22	2.12	2.02	2.03	2.00	39.20	40.09	40.11	40.05	40.07	0.5	1.00
Fovea centralis	2.49	2.19	2.16	2.23	2.28	39.81	40.01	39.99	39.92	39.90	0.35	5.00
The crown	3.79	2.13	1.94	1.88	1.88	38.73	40.14	40.25	40.29	40.30	1.0	4.50
Rosa el' toro	3.41	2.57	2.08	1.94	1.84	39.05	39.71	40.08	40.14	40.19	1.0	4.50
Lotus leaf	3.69	2.99	2.15	1.90	1.91	38.81	39.39	40.07	40.24	40.18	0.7	3.30
Sinusoidal	3.18	2.53	2.23	2.04	1.95	39.23	39.77	39.98	40.08	40.13	1	2.5

The aspect ratio selection methodology, presented in Table 3.3, provides a comprehensive approach. It is important to note that for certain textures, an aspect ratio is chosen despite slightly higher reflective losses due to overall increase in the photocurrent density. In this study, the aspect ratios tested were limited to a maximum of 1 to optimize computational time.

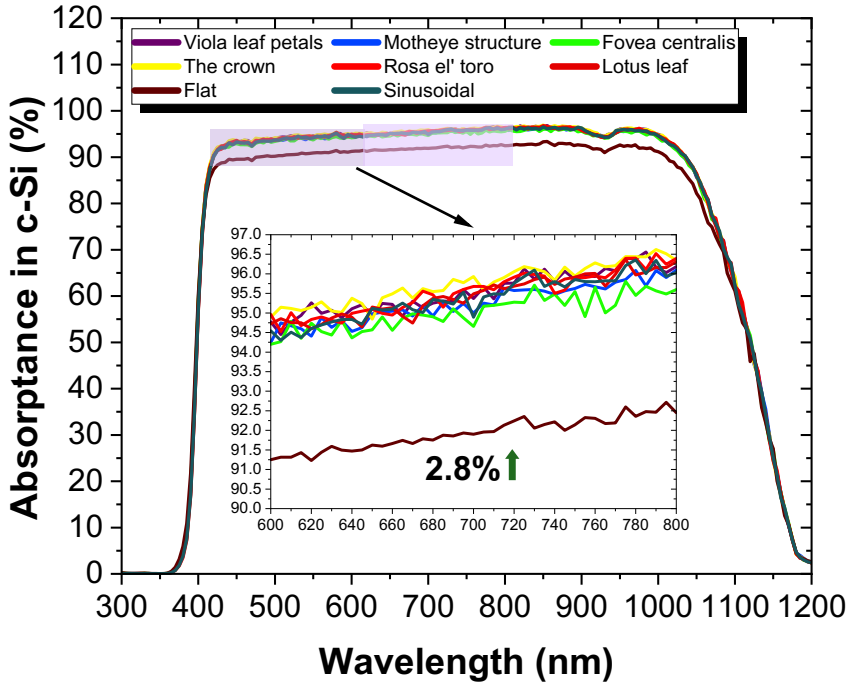

Figure 3.21: External quantum efficiency measured for all textures at various aspect ratios under normal incidence.

Figure 3.21 compares the performance of the cell stack with the selected aspect ratios and different textures to a flat front sheet. It is evident that all the examined textures consistently outperform the flat cell stack across the entire wavelength range. A closer examination of the graph highlights this distinction. On average, the crown texture which shows the highest absorber absorptance at normal incidence amongst all the textures outperform the flat stack by 2.8%.

3.5.3 Optical performance of the textured geometries

This section presents a detailed evaluation of the optical performance of the textures specified in Table 3.3, along with various additional textured geometries, within the context of this thesis. The assessment focuses on two crucial parameters: the overall enhancement in photocurrent density and the improvement in absorptance in the absorber layer. These parameters serve as the primary drivers behind our rigorous evaluation, aiming to provide valuable insights into the effectiveness of the textures.

Furthermore, a thorough examination is conducted to analyze the total air-front sheet reflectance at different angles of incidence for all the simulated textures. This analysis plays a vital role in understanding the reflectance behavior exhibited by the textures and contributes significantly to the understanding of their optical characteristics.

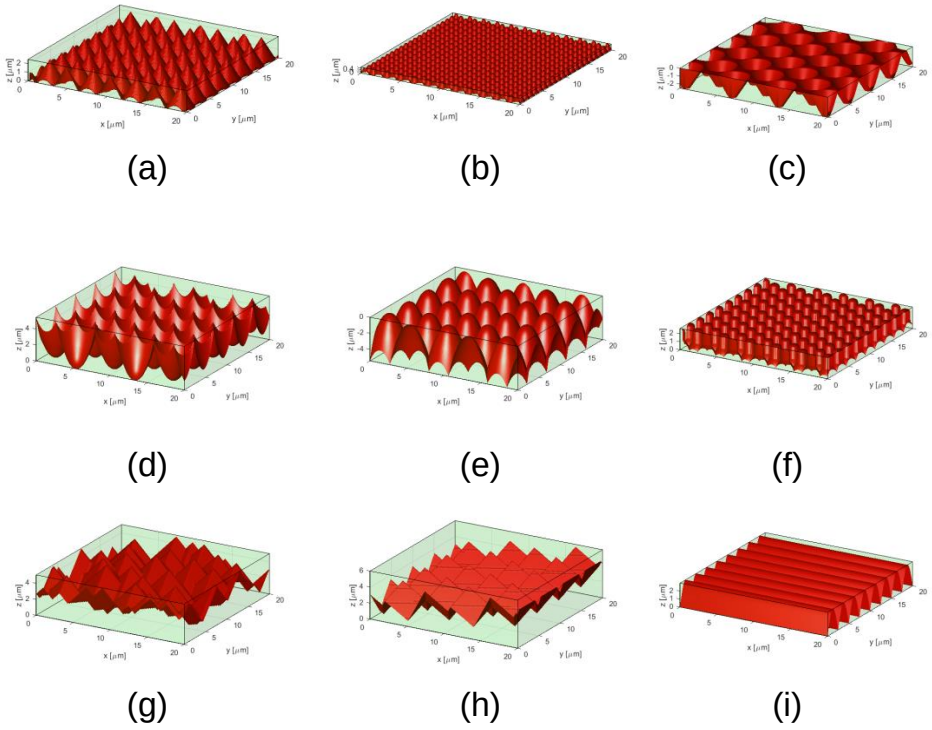

Figure 3.22: Textures. (a) Viola leaf petals. (b) Motheye's structure. (c) Fovea centralis. (d) The crown. (e) Rosa el' toro. (f) Lotus leaf. (g) Random pyramids. (h) The corner cube. (i) Sinusoidal

Figure 3.22 illustrates a collection of simulated textures in this thesis. The primary objective of selecting nine textures is to conduct a comparative study on the optical performance of each textured geometry at different angles of incidence. The main focus is on bio-inspired textures, aiming to investigate the impact of scale modification. Natural textures extracted from the environment exist at the nanometer scale, where light behaves as a wave. This study aims to scale these textures to the micron scale by optimizing the aspect ratio to achieve optimal performance, as demonstrated in Table 3.3. The period is kept the same as it was observed that there is no significant changes in performance with change in the period.

In Figure 3.22 (a), the texture of viola leafs is depicted, resembling a microcone texture with a circular base and a determined height to meet the required aspect ratio. Figure 3.22 (b) shows the motheye texture, closely resembling a circular cone with a blunt tip. Figure 3.22 (c) represents the 3D texture of the Fovea centralis, resembling an inverted frustum with predetermined top and bottom diameters. Figure 3.22 (e) represents the structure of a rose petal, following a parabolic equation $y = \frac{h}{r^2} \cdot x^2$. Figure 3.22 (d) shows the crown texture which follows the equation as mention by 3.3. Figure 3.22 (f) provides an approximate representation of the textures on a lotus leaf based on a scanning electron

microscope (SEM) image from available literature. While not an exact depiction, it offers an overview of the light trapping and anti-reflection properties of the lotus leaf.

Figures 3.22 (g), (h), and (i) depict non-bio-inspired texture geometries. Figure (g) represents a random pyramidal texture widely utilized in academia and industry, featuring a corner angle of 54.7°. Figure (h) showcases the corner cube, consisting of multiple cubes arranged in a stacked matrix with a vertex angle of 90°. Lastly, (i) displays a sinusoidal texture following a simple equation: $y = \sin(x)$.

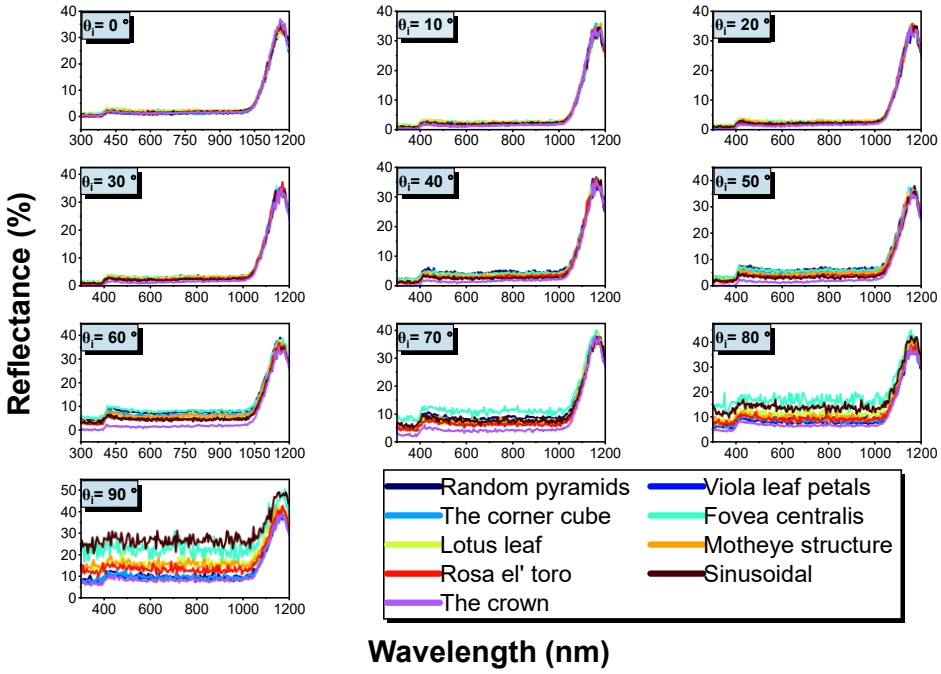

Figure 3.23: Total reflectance of the cell stack with different texture morphologies at difference incident angles.

Figure 3.23 illustrates the variation of the total reflectance for the aforementioned texture morphologies at different angles of incidence within the wavelength range of 300 nm to 1200 nm. These plots highlight the influence of texture geometries on optical performance. Notably, all textures exhibit similar total reflectance characteristics until $\theta_i = 30^\circ$. However, the impact of texture geometries becomes more apparent at higher angles of incidence, specifically in the range of $\theta_i = 60^\circ - 90^\circ$. Therefore, to effectively compare different textured surfaces, it is essential to analyze their performance at higher angles of incidence, enabling a clear choice in terms of performance. While the above plots provide valuable insights into the role of textures, they can be challenging to analyze when comparing the relative performance of individual textures. To gain more information about the front reflection, figure 3.24 can be utilised. Figure 3.24 illustrates the variation in textured reflectance compared to a flat front sheet without any textures. The three plots depict the percentage decrease in average reflectance across three different light regimes.

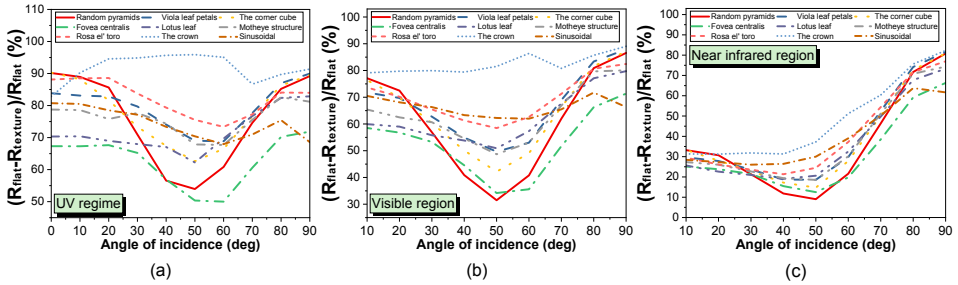

Figure 3.24: The percentage decrease in reflectance observed across various textures in comparison to a flat stack. (a) Relative decrease in the UV regime. (b) Relative decrease in the visible region. (c) Relative decrease in the near infrared region.

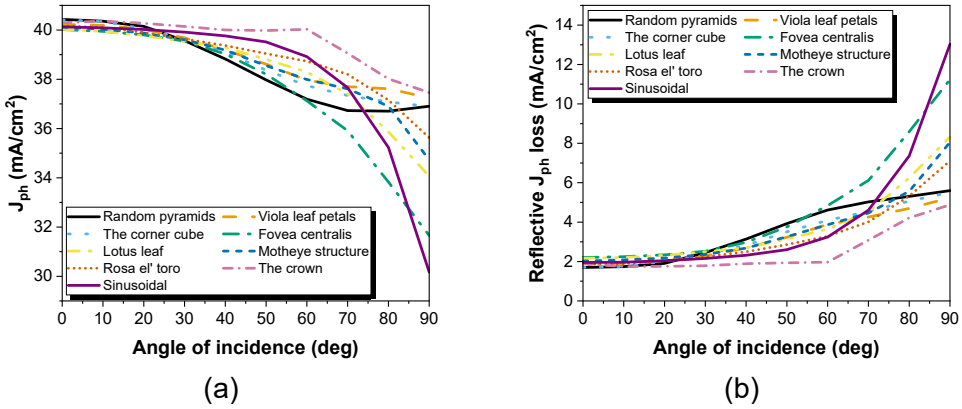

Figure 3.25: (a) Photocurrent density variation with incidence angle for various texture geometries. (b) Influence of incidence angles on photocurrent density loss due to reflection with different texture geometries.

In Figure 3.24 (a), the drop in average reflectance within the UV regime is prominently observed, with the crown texture exhibiting the highest decrease at approximately 90% compared to the other textures. This trend is similarly observed in the other two regimes. Notably, the average reflectance decrease in the near infrared region is comparatively lower than in the other two regimes, suggesting that the textures are more effective in the UV and visible regions, where the reflectance drop can reach up to a maximum of approximately 90%. It can be said that by incorporating the crown texture on the Solarge front sheet, the reflectance in the UV and the visible region can be significantly reduced to yield a higher power output.

After analyzing the impact of different textures on the overall front reflectance of the cell stack, the results are presented in Figure 3.25. Figure 3.25(a) demonstrates the variation of photocurrent density and the corresponding loss in photocurrent density due to front reflection. It is evident that all textures contribute to an increased photocurrent density across various angles of incidence. However, the crown texture stands out by exhibiting angle insensitivity up to 60°. This texture achieves an average photocurrent density of

40.15 mA/cm^2, surpassing the flat front sheet's J_{ph} by 5.65% within the same range of incidence angles. Notably, the crown texture consistently outperforms other textures, as they demonstrate a gradual decrease in J_{ph} with increasing angle of incidence. The crown texture's exceptional characteristic lies in its ability to maintain angle insensitivity for 60% of the incidence angle range. In Figure 3.25 (b), the loss in potential photocurrent density due to front interface reflection is illustrated. At low angles of incidence (up to 20°), the losses for all textures are incomparable. However, a clear distinction emerges at relatively higher angles of incidence, aligning with the reflectance curve trends observed earlier. The crown texture once again exhibits superior performance, followed by the viola leaf petals. The discrepancies in losses between textures are primarily determined by their performance within the $40^\circ - 90^\circ$ angle range.

From figure 3.26 the absorptance in the absorber layer can be seen for different textured geometries. It can be observed from these plots that the difference between different textures are not very significant up until $\theta_i = 30^\circ$. But after this angle, the difference is more noticeable. It can be observed from these plots that the CROWN texture shows the best performance at higher angles of incidence in comparison to other texture geometries.

Based on the analysis of the evaluated textures, it is evident that the crown texture consistently outperforms the other textures. The results consistently indicate its superior optical efficiency, making it a highly promising candidate for further enhancement beyond the capabilities of texture-1. Therefore, the crown texture stands out as a compelling choice for advancement in the Solarge cell stack performance.

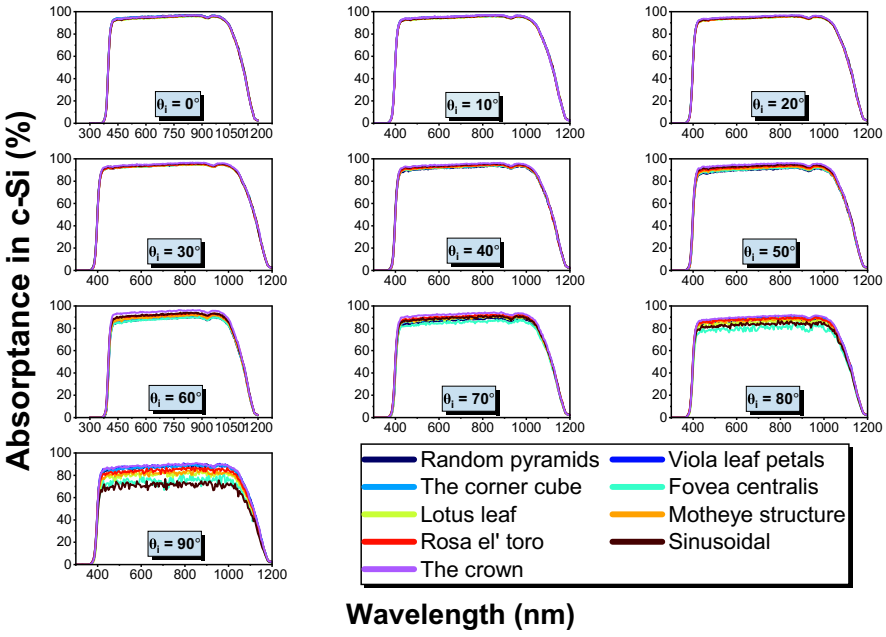

Figure 3.26: Absorber layer absorptance across different angles of incidence for a range of texture geometries.

3.6 Phase IV: Optimization

This section presents a set of optimizations aimed at significantly improving the optical and electrical performance of the Solarge cell stack. The optimizations encompass various aspects, including identifying the most viable texture geometries, exploring variations in the front sheet thickness, and optimizing the backsheet to enhance internal light reflection within the module, as outlined in Table A.1. Subsequently, these optimizations are simulated, and a final single cell laminate is fabricated, incorporating all the recommended improvements. Rigorous optical and electrical characterizations are conducted to evaluate the performance of the optimized cell.

The results obtained from the optimizations serve as a basis for providing conclusive recommendations to Solarge for future research endeavors in this field. These recommendations are carefully derived from a deep understanding of the outcomes obtained throughout the optimization process, aiming to guide and inform future investigations.

3.6.1 Texture recommendation

In this subsection, final recommendations are provided based on a combination of experimental data and validated simulations. Phase II of this chapter involved testing nine different texture geometries using two fabrication methods: release paper and Teflon sheets. The initial texture analysis revealed that texture-1, characterized by a hierarchical morphology, outperformed the other textures. Texture-1 demonstrated a 2% higher power output compared to the coarse Teflon texture recently adopted by Solarge in their modules. Extrapolating to a full-size module with 72 cells, texture-1 would ideally yield an additional 4.75W compared to the coarse Teflon texture. Another noteworthy texture that emerged from Phase III of this chapter is the 'CROWN' texture. Optical analysis demonstrated that it exhibited the highest drop in reflectance compared to a flat front sheet and overall improved absorber absorptance across all incident angles, resembling angle-independent performance.

This section presents a brief comparison between the performance of texture-1 and the Crown texture. However, certain constraints in simulation and experimental measurements dictate the performance criteria used for the comparison:

1. **Constraint 1:** The exact replication of the optical model of texture-1 is not feasible in this thesis, as employing high-end equipment such as an atomic force microscope (AFM) would be excessive for polymer materials. Additionally, constructing and simulating hierarchical textures are beyond the scope of this thesis.

2. **Constraint 2:** Fabricating the Crown texture would require additional time and collaboration with companies like company [A] or company [B] to find a suitable Teflon material capable of hosting such a texture. Given the timeline of this thesis, such collaboration would not yield to possibility of obtaining a scalable roll-to-roll workflow.

To provide Solarge with a valid and practical solution, this thesis combines the best aspects of both textures. Measured values of texture-1 are compared to the simulated values of the Crown texture. Since the simulation is validated using the same set of boundary

conditions as the measured single-cell laminates, a fair comparison can be made between these two texture geometries.

Furthermore, due to the limited availability of certain equipment, this thesis aims to extract as much information as possible using the tools at hand. Therefore, the comparison between the two textures is based on the following parameters:

1. **Total reflectance:** The total reflectance of both textures can be compared at normal incidence angles, given the unavailability of the appropriate equipment (e.g., ARTA) to measure reflectance at different angles of incidence.

2. **External quantum efficiency:** The *EQE* of texture-1 is compared to the absorber layer absorptance of the crown texture at different angles of incidence, providing an overall assessment of their performance.

3. **Current density:** Considering the validation of the texture simulation, where the measured *EQE* matched the simulated values within acceptable deviations, it can be inferred that the current density (J_{ph}) obtained from simulation is approximately equal to the short-circuit current (J_{sc}) measured by the equipment with certain acceptable error range.

Comparison of total reflectance and current density

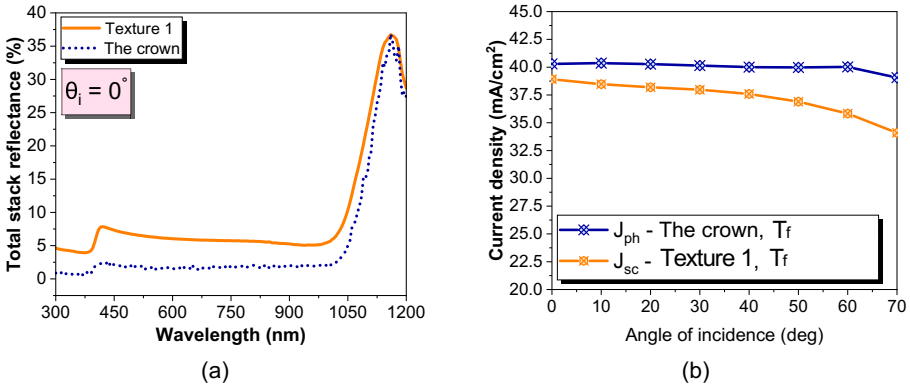

Figure 3.27: (a) Comparison of total stack reflection using texture-1 (measured) and with the crown texture (simulation) at normal incidence of light. (b) Comparison of the simulated photocurrent density of the crown texture and the measured short-circuit current density of texture-1.

From Figure 3.27 (a), it is evident that the total average stack reflection of the crown texture is 4% lower than that of texture 1. This reduction in stack reflection corresponds to an increase in the photocurrent current density by 2.2mA/cm^2 compared to the short circuit current density of texture-1, as shown in Figure 3.27 (b). This improvement can be attributed to the additional photocurrent density (J_{ph}) reaching the solar cell, which would have otherwise been lost due to reflection at the air/front sheet interface.

External quantum efficiency

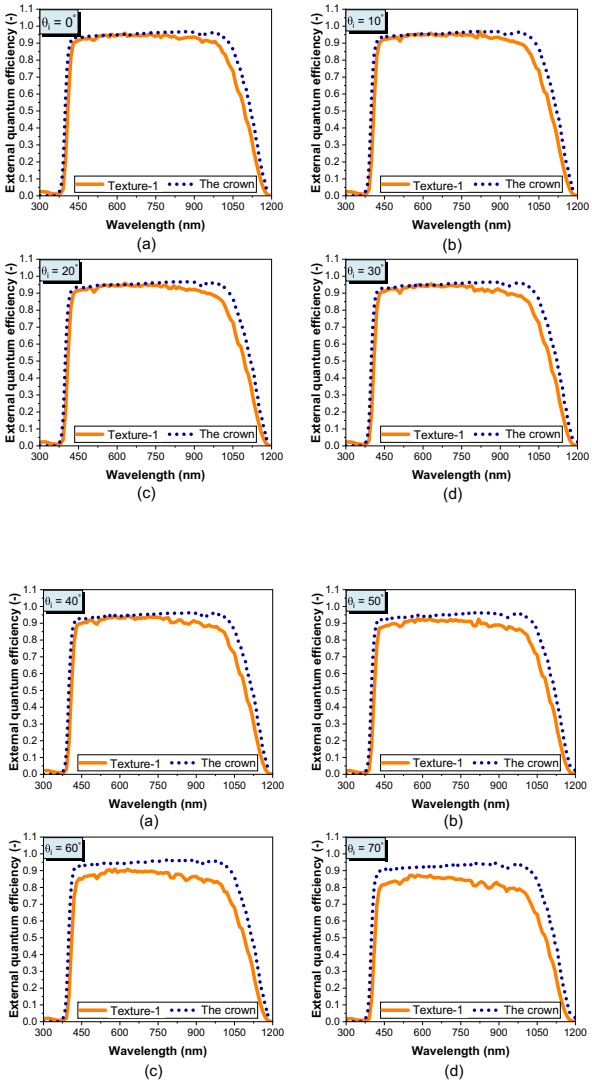

Figure 3.28: Comparison between measured external quantum efficiency (EQE) for texture-1 and simulated absorptance in the absorber layer for the crown texture.

Figure 3.28 presents the external quantum efficiency (*EQE*) for both the crown texture and texture-1 at various angles of incidence. As observed throughout this thesis, the change in *EQE* at lower angles of incidence is minimal compared to the change at larger angles. Notably, the performance of the crown texture stands out at larger angles of incidence, particularly from $\theta_i = 40^\circ$ onwards. This enhanced performance solidifies the crown texture as a strong candidate for future implementation in the Solarge production line.

Therefore, this section provides two texture recommendations to Solarge:

1. **Texture-1:** Texture-1 is the first recommendation to Solarge due to the existing foundation in the fabrication process of the master mold for this texture. Additionally, incorporating a roll-to-roll process for high-volume production at Solarge would be relatively straightforward and manageable.

2. **The Crown:** The Crown texture represents a significant breakthrough for future Solarge modules, offering superior performance at various angles of incidence. Based on the aforementioned comparisons, it has the potential to outperform texture-1. The only delay in implementing this texture is the time required to adapt it to a roll-to-roll process. Collaborations are currently underway, and this texture may be incorporated into Solarge's main high-volume production line in the near future.

These recommendations provide Solarge with viable options to enhance the optical and electrical performance of their solar cell stack, taking into account the feasibility of fabrication processes and the potential for improved efficiency.

3.6.2 Thickness optimisation

In this subsection, an optimization process is conducted to investigate the impact of varying the thickness of the front sheet on the optical and electrical properties of the Solarge cell stack. Front surface texturing is known to enhance light trapping by reducing overall stack reflection, while reducing the front sheet thickness helps mitigate parasitic absorption within the front sheet. The initial focus of this optimization is on the crown texture, which has exhibited superior performance among the tested textures. The goal of this optimization process is to identify an optimal front sheet thickness that maximizes light trapping and minimizes parasitic absorption, thereby enhancing the overall performance of the solar cell stack.

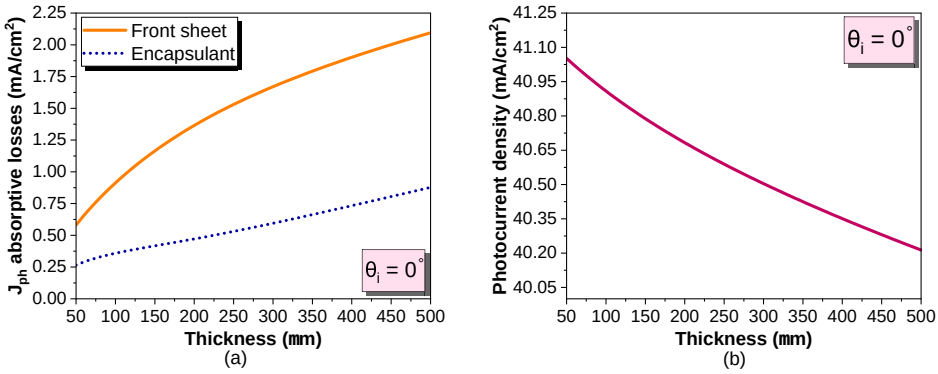

Figure 3.29: Effect of front sheet and encapsulant thickness on the optical performance of the cell stack with the CROWN texture (simulated results). (a) Absorptive photocurrent density losses with varying thickness. (b) Photocurrent density due to changing thickness.

It is worth noting that this optimization process is assumed to be applicable to texture-1 as well as the relative increase in the photocurrent density would be similar with acceptable

differences for all the textures due to the extensive validation steps taken in this thesis. By conducting this analysis, an understanding of the interplay between front sheet thickness and its influence on the optical and electrical properties of both texture-1 and the crown textures can be obtained. This understanding will be instrumental in developing guidelines and recommendations for selecting the optimal front sheet thickness in conjunction with either the crown texture or texture-1, resulting in improved performance and efficiency of the Solarge cell stack.

Figure 3.29 illustrates the relationship between optical losses and the thickness of the front sheet and encapsulant. In Figure 3.29(a), the loss in photocurrent density due to parasitic absorption in the solar cell stack is shown. While the absorptive losses in the encapsulant are relatively minor and unaffected significantly by thickness variations, the front sheet demonstrates more significant changes in absorptive losses with increasing thickness. Consequently, a lower front sheet thickness is desirable to minimize absorptive losses. However, selecting an optimal thickness is challenging due to the front sheet's dual role of supporting textures and withstanding mechanical loads under various weather conditions.

To address these constraints and enhance optical performance without compromising front sheet strength, a thickness of $0.46 \cdot T_f \ (\mu m)$ is chosen as the optimal value. Figure 2.3(b) presents the corresponding variation in generated photocurrent density with front sheet and encapsulant thicknesses. As expected, the photocurrent density decreases with increasing thickness, indicating higher absorptive losses. Therefore, the optimized front sheet thickness of $0.46 \cdot T_f \ (\mu m)$ is selected while maintaining the encapsulant thickness at $T_e \ (\mu m)$.

By striking a balance between optical performance and mechanical strength, this optimized configuration contributes to the improved overall efficiency of the Solarge solar cell stack.

3.6.3 Backsheet optimisation

In this subsection, the optimization of the backsheet in the Solarge solar cell stack is addressed. While the front sheet focuses on enhancing transmittance and reducing reflection, the backsheet plays a crucial role in reducing transmittance and increasing reflectance. By incorporating a highly reflective backsheet, the internal reflection of light within the cell gap is promoted, leading to increased light absorption and improved overall performance of the solar cell stack.

Figure 3.30 provides an overview of the optical performance of the Solarge backsheet. The average values of total reflectance, transmittance, and absorptance can be observed from Table 3.4. It is evident that the backsheet exhibits a significant level of transmittance, allowing 8% of the incident light to pass through. This transmittance leads to a loss of 4.1 mA/cm^2, emphasizing the need to minimize this loss and enhance the internal coupling of light with the backsheet.

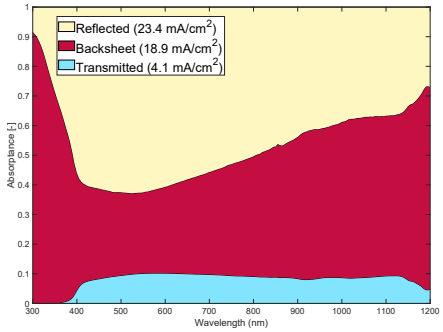

Figure 3.30: Current optical performance of the Solarge backsheet.

Table 3.4: Average values of the optical properties

Parameters	Value (%)
R_{avg}	46.7
T_{avg}	8.0
A_{avg}	45.3

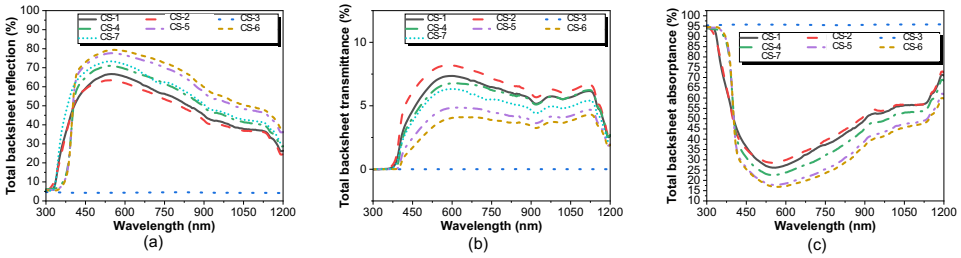

Figure 3.31: Influence of different composite sheets (CS) on the backsheet. (a) Total backsheet reflection. (b) Total backsheet transmittance. (c) Total backsheet absorptance.

Figure 3.31 showcases the optical properties of the backsheet laminated with single sheets of a 'composite material' sourced from company [C]. In this thesis, a total of seven different composite sheets (CS) are investigated to assess their impact on the overall performance of the backsheet. These composite sheets are manufactured using different processes, resulting in variations in pigmentation and coloration of the materials. The primary objective is to minimize transmittance and convert it to reflectance, thereby reducing absorptance.

Table 3.5 provides an overview of the average optical properties for the different composite sheets (CS). Notably, backsheet with the CS-6 stands out with the highest average reflectance of 58.28%, accompanied by a total average transmittance of 3.06%. This transmittance reduction is approximately 61.75% lower compared to the regular backsheet

without any composite sheet. The conversion of transmittance and absorptance to enhanced reflectance makes CS-6 particularly suitable for this application.

By incorporating CS-6 in the backsheet, Solarge can effectively enhance the reflectance properties of the module, reducing the overall optical losses and improving the performance of the cell stack.

Table 3.5: Average optical properties with different composite sheets (CS)

	300nm -1200nm						
Sample	**CS-1**	**CS-2**	**CS-3**	**CS-4**	**CS-5**	**CS-6**	**CS-7**
R_{avg} **(%)**	47.33	45.58	4.36	50.06	56.45	58.28	53.26
T_{avg} **(%)**	5.23	5.89	0.002	5	3.56	3.06	4.47
A_{avg} **(%)**	47.45	48.53	95.64	44.94	39.99	38.66	42.27

3.6.4 Optimised performance

This section integrates the previously mentioned optimizations into the existing cell stack. By utilizing a combination of experimental and computational techniques, a comparative analysis is conducted on the four configurations. This analysis aims to provide a thorough evaluation of the performance enhancements achieved through the recommended optimizations.

To accurately characterize the performance of the cell stacks, both optical and electrical assessments are performed on all the stack configurations. These evaluations enable a real-time assessment of the performance of the cell stacks, providing valuable insights and data for further analysis.

Cell stack information

First and foremost, before delving into the comparative study, it is crucial to understand the optimizations that have been incorporated into the cell stack. Additionally, it is essential to visualize the cell stacks both before and after the optimization process. This understanding and visualization serve as a foundation for the subsequent comparative analysis, enabling a clear assessment of the impact of the optimizations on the cell stack's structure and design.

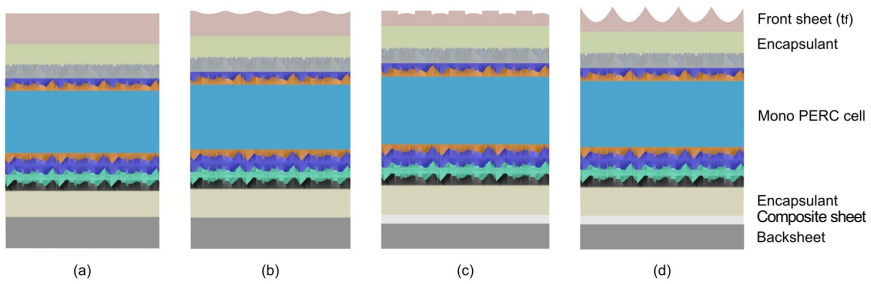

Figure 3.32: Cell stack configurations. (a) Base case with flat front sheet (T_f (μm), with CS-2). (b) Current solarge stack with coarse Teflon textures (T_f (μm), with CS-2). (c) First recommendation with texture-1 ($0.46 \cdot T_f$ (μm), with CS-6 reflector sheet). (d) Ultimate recommendation with the Crown texture ($0.46 \cdot T_f$ (μm), with CS-6 reflector sheet)

Figure 3.32 depicts the four configurations that have been characterized for the final comparison. Detailed information regarding these configurations is provided below:

1. **Base case:** This configuration represents the initial state described at the beginning of this section. It involves a flat front sheet without any textures, with a front sheet thickness of T_f (μm), and contains a backsheet with the CS-2 shown in table 3.5.

2. **Current Solarge case:** This configuration analyzes the current Solarge stack, which features a coarse Teflon texture, a front sheet thickness of T_f (μm), and contains a backsheet with the CS-2 shown in table 3.5.

3. **First recommendation:** This configuration corresponds to the first intermediate recommendation proposed in this thesis. It incorporates texture-1, a thin front sheet with a thickness of $0.46 \cdot T_f$ (μm), and a layer of CS-6 reflector sheet.

4. **Ultimate recommendation:** This configuration represents the ultimate recommendation put forth by this thesis for Solarge. It involves using a thin front sheet with a thickness of $0.46 \cdot T_f$ (μm), incorporating the crown texture, and adding a layer of of CS-6 reflector sheet.

As stated at the beginning of this section, the comparative study is conducted using a combination of experimental and computational approaches. This comparison serves as a fair basis for evaluating both experiments and computations. It is important to note that the optical model used in this thesis has undergone multiple validation processes to ensure that the output of the optical simulation which is recommended to closely align with the real-time performance of the cell stack.

Table 3.6 provides an overview of the results obtained from the comparative study. It is worth mentioning that three out of the four case studies have been experimentally fabricated and tested, including the first recommendation made to Solarge. However, due to constraints in the manufacturing process, the ultimate recommendation has been computationally evaluated. This approach ensures that the proposed optimizations are thoroughly analyzed and validated, giving a prediction which resembles the real-time performance of the cell stack.

Table 3.6: Comparative study layout

Case study	Experimental	Computation	Comments
Base case	✓	✓	Both validation performed as shown in chapter 2
Current Solarge case	✓	X	Obtaining a 3D heightmap with the Dektak profilometer very challenging
First recommendation	✓	X	Obtaining a 3D heightmap with the Dektak profilometer very challenging
Ultimate recommendation	X	✓	Manufacturing this texture is the scope of future work

Optical performance

As followed in all the other sections, this section also starts off with the optical performance of all the case studies evaluated in this section.

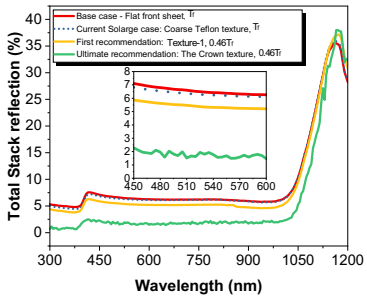

Figure 3.33: Comparison of the measured total stack reflection at normal incidence for the base case, current Solarge case, first recommendation, and simulated stack reflection for the ultimate recommendation.

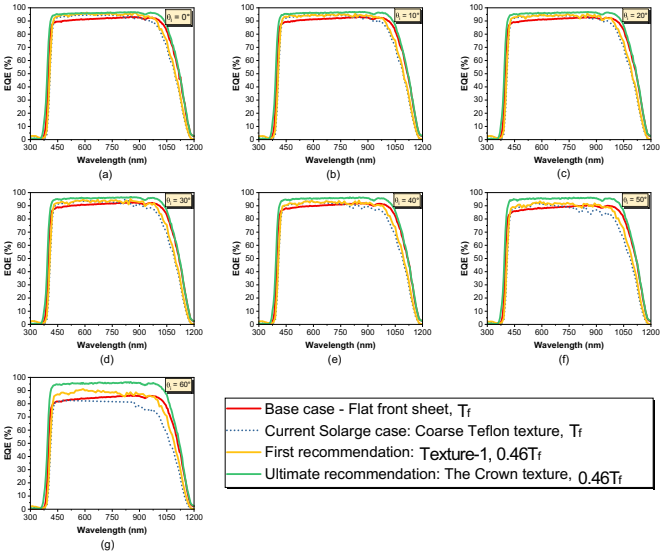

Figure 3.34: Comparison of the measured EQE at normal incidence for the base case, current Solarge case, first recommendation, and simulated absorber absorptance for the ultimate recommendation.

From Figure 3.33, the overall performance of the cell stack is visually represented. It is evident that the optimizations proposed in this chapter have led to significant improvements in the optical performance of the cell stack. Notably, the first recommended configuration for Solarge demonstrates a relative decrease of 7.8% in reflectance compared to the current Solarge case with the coarse Teflon texture. Furthermore, the utilization of the crown texture exhibits a remarkable 42.3% relative decrease in the total stack reflectance compared to the current Solarge stack. These findings highlight that both the recommendations made in this thesis offer superior enhancements over the existing texture morphology employed by Solarge.

Figure 3.34 displays the plot of the external quantum efficiency (*EQE*) for all the case studies, spanning from an incidence angle of 0° to 60°. It is evident that the crown texture

outperforms all other case studies in terms of *EQE*. Notably, at small angles of incidence, the change in *EQE* is not significant. However, this effect becomes more pronounced at higher angles of incidence.

It is important to note that the base case and ultimate recommendation exhibit simulated curves, and a slight mismatch between these curves and measured curves in the range of 1100nm-1200nm can be observed and this could be due to the recombination losses which is not being considered in the optical simulation. This discrepancy can be attributed to experimental errors as well as computational disparities. Nonetheless, the overall analysis provides a clear understanding of the direction that Solarge should pursue.

Although the current Solarge case performs similarly to the first recommendation up to an incidence angle of $\theta_i = 30^{\circ}$, it starts to underperform at higher angles of incidence, occasionally even performing worse than the flat interface, as depicted in Figure 3.34 (f). The trend observed in Figure 3.34 (g) concerning the coarse Teflon texture may include some experimental errors, as the performance decrement appears too drastic. However, the overall trend at high angles of incidence does not align well with the current Solarge stack. Consequently, the recommendations presented in this thesis demonstrate better optical performance overall.

Electrical performance

In this subsection, the electrical performance of the three case studies are evaluated (except the ultimate recommendation comparison of the crown texture) and finally the total optical losses in the system are evaluated.

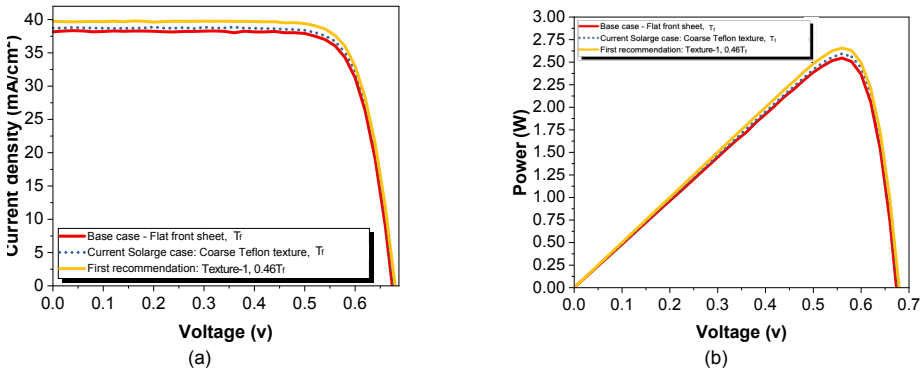

Figure 3.35: Measured electrical performance for the base case, current Solarge case and first recommendation. (a) J-V curve. (b) P-V curve

Figure 3.35 illustrates the electrical performance of the base case, current Solarge case, and the first recommendation. In Figure 3.35 (a), the J-V curve is presented, clearly indicating that the first recommendation outperforms the other two cases, exhibiting an increase in the short circuit current density by 2.65% in comparison to the current Solarge case with the coarse Teflon texture and by 4.2% when compared to the base case. This improvement can be attributed to the enhanced optical performance of the cell stack

achieved through the recommended optimizations (texture, thickness reduction, backsheet reflectance enhancement).

Similarly, in Figure 3.35 (b), the maximum power output of the first recommendation with texture-1 demonstrates the highest value when compared to the current Solarge texture and the flat interface. This finding further emphasizes the superior electrical performance achieved through the implementation of the recommended optimizations.

Overall, these results highlight the significant impact of the proposed optimizations on the electrical performance of the cell stack, leading to increased short circuit current density and improved power output, particularly in the case of the first recommendation with texture-1.

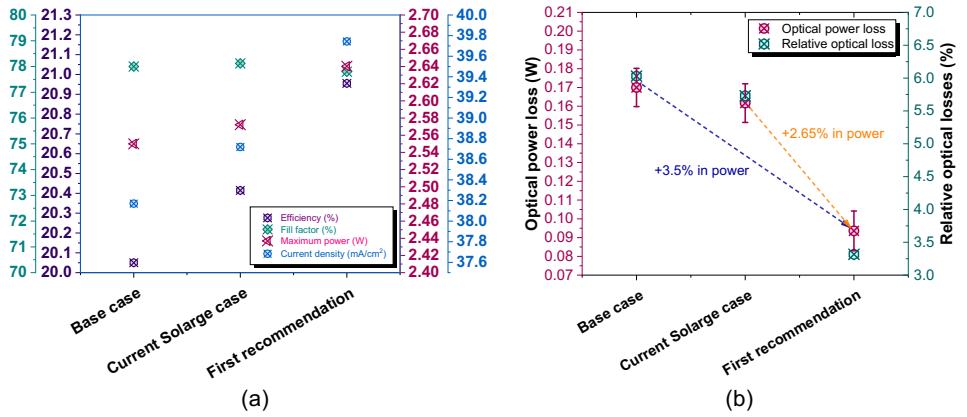

Figure 3.36: Measured electrical performance for the base case, current Solarge case and first recommendation. (a) Four electrical parameters defining the cell stack. (b) Estimation of optical losses and relative optical losses.

Figure 3.36 (a) depicts the variation of electrical parameters for the different case studies evaluated in this chapter. Notably, all four electrical parameters, namely power output, short-circuit current density, fill factor, and efficiency, exhibit enhancements in the first recommendation proposed in this thesis, incorporating texture-1. Specifically, the efficiency of the cell stack has increased from 20.7% in the current Solarge case to 21% with the optimized first recommendation. This represents a relative increase of 1.45% in the overall efficiency of the cell stack. Similar trends can be observed for all the parameters, as visually represented in Figure 3.36 (b), which illustrates the relationship between optical power loss and relative optical losses in the system for the three discussed cases.

The optical power loss is calculated using Equation 2.6. The plot clearly indicates a reduction in optical losses to 3.3% with the first recommendation, compared to the current Solarge stack with 5.8%. This reduction in optical losses corresponds to a relative increase of 2.65% in the power output of the cell stack with the implementation of the first recommended cell structure.

To provide a practical perspective, let us consider a Solarge module consisting of 72 full G1 mono PERC cells. With the current Solarge configuration, a total power output of 370W can be obtained. However, if the proposed first recommendation with texture-1 is implemented, the Solarge modules would be capable of producing 380W, which represents

a 10W increase compared to the current performance. This additional 10W provides a significant advantage for Solarge from a business standpoint, as it directly translates to more revenue. Therefore, the first recommended solution serves as an excellent initial enhancement that Solarge can incorporate into their high-volume production line

Final comparison

Up until now, a comprehensive evaluation and comparison of the optical performance of all four case studies have been conducted. In the next step, the electrical performance of the first three case studies was evaluated and compared, excluding the ultimate recommendation with the crown texture due to the limitations in manufacturing the texture as outlined in this thesis. However, it is still possible to gain an understanding of the performance enhancement potential of the ultimate recommendation by comparing the short-circuit current densities of the current Solarge case, the first recommendation with texture-1, and the photocurrent density of the ultimate recommendation with the crown texture.

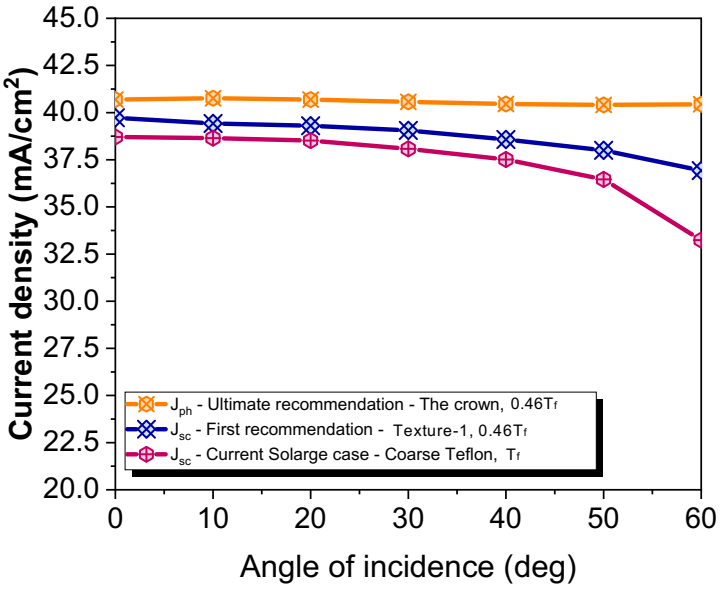

Figure 3.37: Comparison of measured short circuit current density for the current Solarge case and the first recommendation, along with simulated photocurrent density for the ultimate recommendation using the crown texture.

Figure 3.37 illustrates the relationship between the simulated photocurrent density of the crown texture and the measured short-circuit current density of two comparative cases: the current Solarge stack with the coarse Teflon textures and the first recommendation with texture-1. The plot clearly demonstrates that the first recommendation outperforms the current Solarge stack, particularly at higher angles of incidence. This significant improvement is the primary reason for fabricating the optimized stack with texture-1 rather than the coarse Teflon textures.

Moreover, the plot provides valuable insights into the journey towards achieving angular independence. It can be observed that the current Solarge stack experiences a decline in current density starting at $\theta_i = 40^\circ$. Similarly, the first recommendation with texture-1 exhibits a decrease in performance from $\theta_i = 50^\circ$, while the ultimate recommendation with the crown texture begins to show a degradation in performance from $\theta_i = 60^\circ$. With each optimization step, the dip in angular performance is delayed by 10°, resulting in the crown texture maintaining angular independence until $\theta_i = 60^\circ$.

To assess the performance of the ultimate recommendation with the crown texture, the validation of the texture with texture-2 was referred to which revealed that the photocurrent density (J_{ph}) predicted by Genpro4 was, on average, 1.4 mA/cm^2 higher than the actual short-circuit current density (J_{sc}). Hence, by taking this difference into account, it can be said that the crown texture still displays a current density higher than the first recommended texture. Which in turn indicates that the power output using the crown texture would be higher than the power output obtained with the first recommendation.

3.7 Phase V: Business analysis

In this section, a simple business analysis is conducted, considering the four cases discussed previously. It is important to note that this analysis does not encompass all the intricate parameters that would be part of a business plan. Instead, the aim is to provide a rough estimate of the potential profit Solarge could achieve by implementing the recommendations proposed in this thesis.

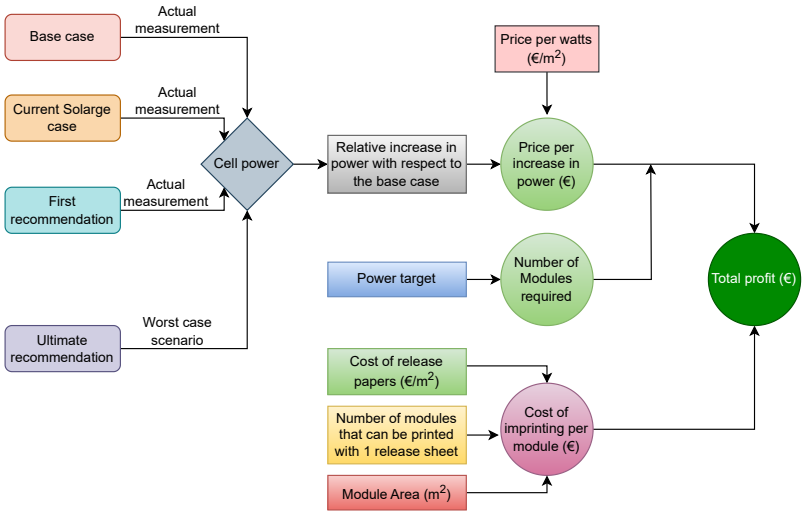

Figure 3.38: Flow process of conducting a simple business analysis

In this section, a simple business analysis is conducted to assess the financial impact of the power increase in different case studies. Figure 3.38 outlines the roadmap for conducting this analysis. The focus is on evaluating the revenue generated by the increase in power and its financial implications for the company.

The analysis considers four case studies: the base case with a flat front sheet, the current Solarge case with the coarse Teflon sheet, the first recommendation with texture-1, and the ultimate recommendation with the crown texture. For the first three case studies, the power output from each configuration is measured. However, the power output for the crown texture is yet to be evaluated, making it the subject of future work. To incorporate the texture in this analysis, a worst-case scenario is considered, assuming that the crown texture produces power that is 0.03% higher than the first recommendation at normal light incidence.

Starting from the base case as the reference point, the relative increase in power is calculated for each case study. The industry standard price per wattpeak of 0.5€/Wp [83, 84] is then multiplied by the relative increase in power to estimate the profit incurred in each case. To evaluate the total extra revenue generated, a power target of 37MW is assumed in order to evaluate the revenue generated by Solarge every year.

In addition, the cost of imprinting is considered to provide a realistic approach to the numbers. The best-case scenario is assumed for the current Solarge case, while the worst-case scenario is considered for the first recommendation with texture-1, following a conservative approach.

Finally, the total profit resulting from the extra increase in power can be evaluated using the following equation:

$$\text{Total profit (€)} = [\text{Price per increase in power (€)} \times \text{Number of modules}] - \text{Cost of imprinting (€)} \tag{3.4}$$

This equation allows for a comprehensive assessment of the financial benefits derived from the increase in power. It is important to note that this business analysis provides a simplified overview and does not account for all the factors involved in a comprehensive financial analysis. However, it serves as a starting point for understanding the potential profitability associated with the power increase in the different case studies.

Table 3.7: Financial analysis

	Base case	Current Solarge case	First recommendation	Ultimate recommendation
Cell Power (W)	2.55	2.57	2.640	2.641
Module Power (W)	366.63	369.85	380.21	380.30
Power increase, $W_{p_{inc}}$ (W)	0.00	3.21	10.36	10.46
Price per wattpeak (€/Wp)	0.5	0.5	0.5	0.5
Price per increase in, $W_{P_{inc}}$ (€)	0	1.61	5.18	5.23
Number of modules (-)	40.00	40.00	40.00	40.00

Method of imprinting	No release paper	Teflon sheet	Release paper	Teflon sheet
Cost of imprinting (€)	-	100	3	100
Number of modules made with one release sheet	-	1000	5	1000
Cost of imprinting per module (€)	-	0.284382	1.706292	0.284382
TOTAL PROFIT (€) per hour	**-**	**52.9**	**139.0**	**197.8**

Table 3.7 provides an overview of the financial analysis conducted for the case studies mentioned in this thesis. The calculation process is straightforward and provides a rough estimate of the profit that Solarge can generate in one hour of production. The estimation is based on the assumption that Solarge can produce 40 modules in one hour. Using this

as a reference, an estimation is made for the revenue generated by the increase in power output of the panels, considering a target power of 110MW.

The table presents the case studies, the relative increase in power achieved, the additional revenue generated per module, and the total additional revenue for the given target power. It also includes the estimated profit based on the assumption of producing 40 modules in one hour. It is important to note that this financial analysis provides a simplified representation of the potential revenue and profit. It serves as a starting point for understanding the financial implications and benefits of the recommended optimizations. Further detailed analysis considering various other factors such as production costs, market demand, and pricing strategies would be required for a comprehensive financial evaluation.

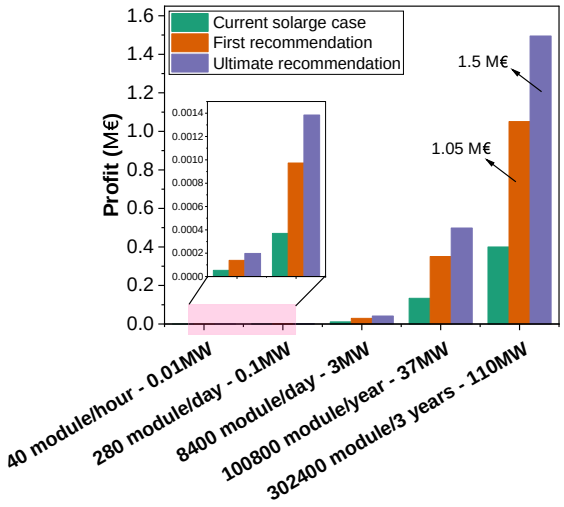

Figure 3.39: Revenue generated for each case study for a power target of 100MW.

Figure 3.39 illustrates the estimated profit generated by the company with different case studies compared to the base case. The plot clearly shows that the first recommendation made in this thesis leads to a profit of approximately 1 million euros. The same plot also includes the case with the ultimate recommendation in the worst-case scenario. It is worth noting that the main difference between the first recommendation and the ultimate recommendation lies in the method of imprinting textures. The first recommendation utilizes the release papers from company [A], which can be costly despite the significant increase in power. On the other hand, the ultimate recommendation proposes the use of the crown texture, an upgraded version of the texture geometry hosted by the Teflon sheets. The assumption made is that if Solarge implements the crown texture and uses Teflon sheets as the host for the textures, even in the worst-case scenario where the power increase is only 0.03% higher than the first recommendation, the company would still generate a profit of around 1.5 million euros for a target power of 110MW. Therefore, future work focused on developing the crown texture using Teflon sheets would be highly beneficial for Solarge. This approach offers the potential for increased profits while minimizing the additional costs associated with the texture imprinting process.

3.8 Conclusion

This chapter aims to address the third and fourth research questions outlined in the first chapter, which pertain to the texturing of the Solarge front sheet and the financial evaluation of implementing such texturing. The following section provide a detailed analysis of each research question:

Addressing the research question

(a) **How can textures be constructed and analyzed on polymer surfaces?** Textures on polymer surfaces can be created through two distinct methods, namely during the lamination process when the polymer is in its glass transition state, or post lamination as part of the cell stack. This thesis focuses specifically on the first method, which involves imprinting the texture on the polymer front sheet using a hot embossing technique. This technique allows for the negative imprint of a master mold onto the polymer surface during the lamination process.

(b) **What are the typical methods used for fabricating these textures?** Various methods can be used for imprinting textures, with consideration given to the peel-off process. Among the available options, Teflon sheets and release papers with specific coatings have proven to be effective for imprinting texture on polymer surfaces. Teflon sheets are ideal for making approximately 1000 modules per sheet, while release papers can be used to imprint texture on at least 5 modules. This thesis focuses on the utilization of Teflon sheets and release papers as the chosen texture implementation methods.

(c) **Which texture is the most practical and efficient?** A total of 19 textures were characterized and analyzed throughout this thesis. Among them, five textures were fabricated and tested experimentally, while one texture was recommended through simulations. Ultimately, two textures were recommended to Solarge, incorporating optimized thickness and backsheet configurations. The first recommendation features texture-1, and the second recommendation entails the crown texture. The optimized stack with texture-1 was successfully fabricated using a $0.46 \cdot T_f$ (μm) front sheet and CS-6 sheet. The crown texture, recommended through simulations, is anticipated to outperform the first recommendation.

Addressing the research question (continued)

(d) **How do these textures perform when exposed to different angles of incident light?** The thesis extensively investigated angle-dependent studies through simulations and experimentation, accurately estimating the performance up to an angle of incidence of $\theta_i = 60^\circ$. The findings indicate that the ultimate recommendation incorporating the crown texture exhibits high potential for angle independence until $\theta_i = 60^\circ$, beyond which a degradation in optical performance is observed.

(e) **How do these textures influence the power output of solar modules?** Electrical characterization was performed for the four case studies presented in this thesis. The results show that the first recommendation, utilizing texture-1, provided a performance boost of 2.65% compared to the current Solarge stack with the coarse Teflon texture. It is predicted that the crown texture will surpass the performance exhibited by the first recommendation.

(f) **In what ways can the company benefit financially from this thesis research?** A simplified financial analysis was conducted to evaluate the potential profitability associated with the four case studies analyzed in this thesis. The results indicate that the first recommendation has the potential to generate a profit of 1 million euros for Solarge, considering the production of 302,400 modules to meet the 100MW target. Even in the worst-case scenario, implementing the crown texture could yield a net profit of approximately 1.5 million euros for Solarge.

4

Summary

This chapter serves as the concluding section of the thesis, summarizing the significant observations and presenting recommendations for future work. The chapter starts by revisiting the objectives set forth in the literature review and addresses the identified research gaps highlighted in Chapter 1. The subsequent chapters are then summarized, highlighting the key findings and contributions of each chapter.

Chapter 2 focuses on characterizing the optical properties of the layers within the Solarge stack. Optical parameters such as refractive index and extinction coefficient are determined using experimental techniques and computational techniques by using the SCOUT and GenPro4 software, enabling the creation of a validated optical model for the Solarge stack. Optical losses within the system are evaluated using the Fraunhofer SmartCalc.CTM software, and the results are validated through the fabrication of a single cell laminate. The chapter concludes by determining the optical loss of the Solarge stack with a flat interface to be 6.03%.

Chapter 3 centers on the texturing of the Solarge front sheet to reduce the optical losses identified in Chapter 2. A roadmap of the chapter is provided, outlining the methodology for characterizing different texture morphologies. The initial texture analysis involves an angle-dependent study of the flat front sheet to assess the optical performance of the Solarge stack. Collaboration with company [A] and company [B], firms specializing in commercial texture production, leads to the selection of several intriguing textures for the current application. The fabrication procedure for imprinting textures using release sheet technology is explained, highlighting the viability of specific release papers with particular coatings. Five different textures are chosen for fabrication and testing, including the coarse Teflon texture, fine Teflon texture, texture-1, texture-2, and texture-3. Thorough optical and electrical characterizations are performed, with texture-1 demonstrating superior performance among the textures.

Surface roughness measurements using a Dektak profilometer reveal that texture-1 possesses a hierarchical morphology, which contributes to its enhanced performance. The third phase of the chapter focuses on designing a custom texture with the potential to outperform texture-1. Motivated by the ease of fabricating textures using Teflon sheets compared to release papers, the crown texture is designed to mimic the coarse Teflon texture

with an aspect ratio modification and hexagonal lattice placement. Simulation results demonstrate that the crown texture outperforms texture-1 and exhibits angle independence up to an angle of incidence of $\theta_i = 60^\circ$. Optimizations are performed, including reducing the front sheet thickness to $0.46 \cdot t_f$ μm and incorporating specific grades of composite sheets obtained from company [C]. The CS-6 reflector sheet is selected to increase the internal reflection of the backsheet, providing an additional power boost. A final single cell laminate incorporating all recommended optimizations is fabricated and characterized optically and electrically, resulting in a significant power increase of 2.65% compared to the current Solarge stack with the coarse Teflon texture. This reduces the overall optical losses in the system to 3.3%.

Finally, a financial analysis is conducted, considering all four case studies presented in the thesis. The first recommendation has the potential to generate a profit of 1 million euros for Solarge, targeting a power output of approximately 100MW. Additionally, a financial analysis using the crown texture, assuming a worst-case scenario with a minimal power boost of only 0.03% compared to the first recommendation, indicates a potential net profit of 1.5 million euros. Consequently, this thesis offers a guide to texturing polymer-based solar cell stacks for industrial applications, providing Solarge with recommendations to significantly improve module performance and generate substantial revenue.

Future Work

The future work, as a continuation of this thesis, encompasses the following aspects:

1. Fabricating the crown texture using Teflon sheets as proposed in this thesis would further enhance the performance of the current first recommendation. Hence further research can be conducted in changing the aspect ratio of the textures hosted by the Teflon sheets.

2. Analyzing and optimizing the impact of soiling on the performance of the recommended textures.

3. Considering the hydrophobic properties of the polymer front sheet observed in due course of this thesis, it is recommended to investigate the wetting properties of the front sheet with the recommended textures presented in this thesis to impart the trends of superhydrophobicity which could ultimately introduce self-cleaning properties.

A

Appendix

A.1 Chapter 1

A.1.1 Power received by Earth

$$P_{\text{sun}} = \varepsilon \sigma A_{\text{sun}} T_{\text{sun}}^4 = 1 \times 5.67 \times 10^{-8} \times 6.07 \times 10^{18} \times 5778^4 = 3.85 \times 10^{26}\ \text{W} \tag{A.1}$$

$$P_{\text{earth}} = \frac{P_{\text{sun}}}{A_{\text{dotted line}}} = \frac{3.85 \times 10^{26}}{4\pi(\text{mean distance})^2} = \frac{3.85 \times 10^{26}}{4\pi(149597870700)^2} = 1370 \left(\frac{\text{W}}{m^2} \right) \tag{A.2}$$

Where,
ε is the emissivity.
σ is the Stefan–Boltzmann constant.
T_{sun} is the temperature of the sun in Kelvin.

A.1.2 Introduction to Rayleigh film and optimal thickness

Example 1: Introducing a Rayleigh film

$$n_{\text{Rayleigh}} = \sqrt{n_{\text{air}} \cdot n_{\text{Si}}} = 1.942$$

Reflectance at each interface is calculated as follows:

$$R_1 = \left(\frac{n_{\text{air}} - n_{\text{Rayleigh}}}{n_{\text{air}} + n_{\text{Rayleigh}}} \right)^2 = \underline{10.25\%} \quad ; \quad R_2 = \left(\frac{n_{\text{Rayleigh}} - n_{\text{Si}}}{n_{\text{Rayleigh}} + n_{\text{Si}}} \right)^2 = \underline{10.24\%}$$

Hence, the total reflectance can be estimated as follows:

$$R_{\text{total}} = R_1 + R_2 = \underline{20.49\%} < 35.51\%$$

A

Example 2: Optimal thickness

Based on the above Rayleigh film, an optimal thickness can be found using the theory as mentioned above for a particular singular wavelength. For demonstration in this example, a wavelength of 750 nm is considered.

$$d_{\text{opt}} = \frac{\lambda}{4 \cdot n_{\text{ARC}}} = \frac{750}{4 \times 1.942} = \underline{96.55 \text{ nm}}$$

A.1.3 Bibliographic landscape

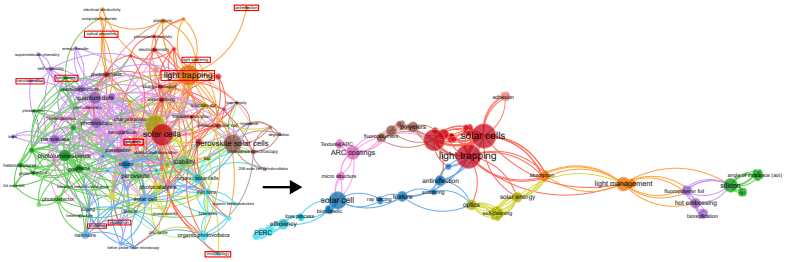

Figure A.1: Bibliometric landscapes. (a) Broader bibliometric network. (b) Narrowed bibliometric network. Data retrieved from https://www.scopus.com/ and image constructed using https://www.vosviewer.com/

A.2 Chapter 2

A.2.1 Detailed manufacturing process

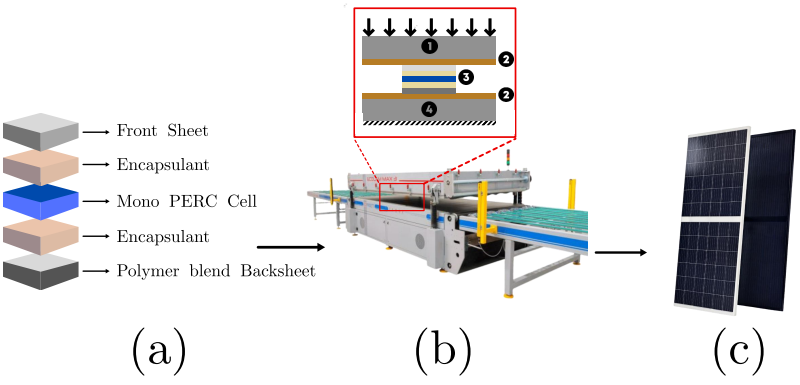

Figure A.2: Manufacturing process. (a) Solarge solar cell stack. (b) Process of Lamination. (c) Solarge polymer module. Image (b) retrieved from https://ecoprogetti.com/product/ecolam-max-3/. Image (c) retrieved from https://solarge.com/en/producten/solarge-solo

A.2.2 Equation to estimate the optical constants

$$R_m = R \cdot \left[\frac{1+(1-2R)\cdot(1-A)^2}{1-(1-A)^2 \cdot R^2} \right] \tag{A.3}$$

$$T_m = \frac{(1-R)^2 \cdot (1-A)}{1-(1-A)^2 \cdot R^2} \tag{A.4}$$

Where,

- R_m is total measured hemispeherical reflectance from spectrophotometer
- T_m is total measured hemispeherical transmittance from spectrophotometer
- **R** is the reflection at each air-sample interface.
- **A** is the fraction of light absorbed per pass.

In order to obtain an expression for the refractive index (n) and the extinction coefficient (k), a stand-alone equation for R and A is required. Hence, equations A.3 and A.4 are solved simultaneously using Matlab to obtain the following equations.

$$R_1 = -\frac{2\,\mathrm{Rm} + \sigma_1 - \mathrm{Rm}^2 + \mathrm{Tm}^2 + 1}{2\,(\mathrm{Rm}-2)} \; ; \; R_2 = -\frac{2\,\mathrm{Rm} - \sigma_1 - \mathrm{Rm}^2 + \mathrm{Tm}^2 + 1}{2\,(\mathrm{Rm}-2)} \tag{A.5}$$

$$A_1 = \frac{2\,\mathrm{Tm} - 2\,\mathrm{Rm} + \sigma_1 + \mathrm{Rm}^2 - \mathrm{Tm}^2 + 1}{2\,\mathrm{Tm}} \; ; \; A_2 = -\frac{2\,\mathrm{Rm} - 2\,\mathrm{Tm} + \sigma_1 - \mathrm{Rm}^2 + \mathrm{Tm}^2 - 1}{2\,\mathrm{Tm}} \tag{A.6}$$

Where,

$$\sigma_1 = \sqrt{\mathrm{Rm}^4 - 4\,\mathrm{Rm}^3 - 2\,\mathrm{Rm}^2\,\mathrm{Tm}^2 + 6\,\mathrm{Rm}^2 + 4\,\mathrm{Rm}\,\mathrm{Tm}^2 - 4\,\mathrm{Rm} + \mathrm{Tm}^4 + 2\,\mathrm{Tm}^2 + 1} \tag{A.7}$$

From equations A.5 and A.6, R_2 and A_2 give an excellent representation of the interface reflections and per pass absorption. Now, using R_2 and A_2, the optical constants can be estimated.

$$n(\lambda) = \frac{1+\sqrt{R_2}}{1-\sqrt{R_2}} \tag{A.8}$$

$$\alpha(\lambda) = \frac{|ln(1-A_2)|}{W} \Rightarrow k(\lambda) = \frac{\alpha(\lambda)\cdot\lambda}{4\cdot\pi} \tag{A.9}$$

In both equations, W represents the thickness of the sample and it is assumed that the ray of light travels perpendicularly to the surface of the sample. However, in practical experimentation using the spectrophotometer, the angle of incidence is 8°. Despite this deviation from the assumption, the impact on the calculation of n from R for randomly polarized light is negligible.

A.2.3 Fraunhofer input parameters

A

Table A.1: loss and gain factors based on material properties and module setup [67]

k-factors	Indication	Significance
k1	Module margin	Inactive area at the module margin
k2	Cell spacing	Inactive area between cells and strings
k3	Cover reflection	Reflection of light at the front interface of the module
k4	Cover absorption	Absorption of light in the front cover
k5	Cover/encapsulant reflection	Reflection of light at the interface between front cover and encapsulation material
k6	Encapsulant absorption	Absorption of light in the encapsulation material
k7	Interconnection shading	Shading of the cell by interconnector ribbons
k8	Cell/encapsulant coupling	Reduced reflection of the cell due to encapsulation (refractive index matching)
k9	Finger coupling	Reflection of light from the cell metallization on the active cell area
k10	Interconnector coupling	Reflection of light from the interconnector ribbons on the active cell area
k11	Cover coupling	Internal reflection of light at the (rear) cover of the module in the cell spacing area
k12	Cell interconnection	Electrical loss in cell interconnector ribbons
k13	String interconnection	Electrical loss in cell string interconnectors
k14	Electrical mismatch	Deviations in electrical cell parameters and from cell binning
k15	Junction box and cabling	Electrical losses in cables and diodes of the junction box
k21	Temperature	Temperature dependency of the solar cell power output
k22	Irradiance intensity	Changes in the level of irradiance
k23	Angular distribution	Changes in the angle of incidence of light
k24	Spectral mismatch	Changes in the spectrum of the incident light

A.2.4 Cell input parameters

Table A.2: Cell input parameters

Input parameters	Full cell	Half-cut cell
Cell selection	Monofacial	Monofacial
Cell type	H-pattern	H-pattern
n-side busbar	Continous	Continous

Continued on next page

Table A.2: Cell input parameters (Continued)

p-side busbar	Contact pads	Contact pads
Length (mm)	158.75	158.75
Width (mm)	158.75	79.38
number of busbar	5	5
efficiency (%)	22.4	22.4
I_{sc} (A)	10.152	5.076
V_{oc} (V)	0.684	0.684
P_{mpp} (W)	5.64	2.82
I_{mpp} (A)	9.665	4.833
V_{mpp} (V)	0.584	0.584
$\alpha_{V_{oc}}$ (%/K)	-0.3	-0.3
$\beta_{I_{sc}}$ (%/K)	0.06	0.06
$\gamma_{P_{mpp}}$ (%/K)	-0.39	-0.39
I_{sc} change (%)	Determined in the next section	
Front parameters		
Total busbar area (mm^2)	449.37	224.68
Number of fingers	116	58
Back parameters		
Total busbar area (mm^2)	390	195
Number of pads per row	5	5

A.2.5 I_{sc} change

This section outlines the precise methodology for determining the factor k8. To estimate k8, it is necessary to calculate the I_{sc} change of the cell stack. The I_{sc} change represents the disparity in I_{sc} values between an encapsulated and unencapsulated solar cell, as illustrated in Figure A.3(a) and (b) respectively. This change encompasses various reflection and absorption losses, encompassing the optical coupling of the solar cell within the encapsulant. To assess the I_{sc} change accurately, a sample with only one layer of encapsulant foil and no front sheet should be employed for the encapsulated measurement.

The disparity in refractive indices between air and encapsulant results in greater reflection of a solar cell when measured against air. However, when the solar cell is encapsulated, the reflection decreases, leading to an increase in the short circuit current. Despite this reduction in reflection, the I_{sc} change from cell to module can still be negative, as the reduced reflection of the cell may be counteracted by additional absorption and reflection caused by the encapsulant. A higher I_{sc} change value signifies a stronger optical coupling.

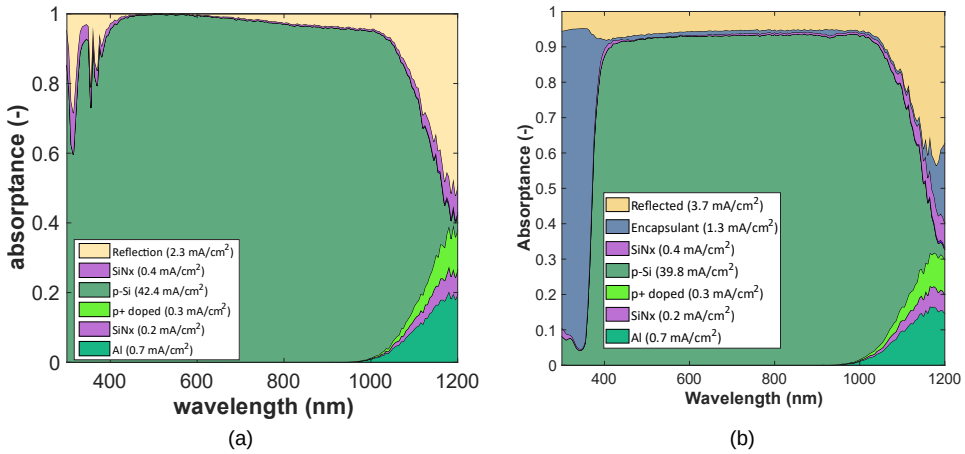

Figure A.3: Determination of I_{sc} using GenPro4 simulations (a) Optical simulation of a bare mono-PERC cell (b) Optical simulation of a mono-PERC cell with one layer of encapsulant on the front side.

To determine the value, the J_{ph} loss resulting from total reflection is employed, utilizing optical simulation as illustrated in Figure A.3(a) and (b). The equation used to estimate this parameter is given by equation A.10

$$\%I_{sc}\ change = \frac{[J_{ph,\,bare} - J_{ph,\,encapsulated}](\frac{mA}{cm^2}) \times A_{cell}(cm^2)}{I_{sc,\,cell}(A) \times 1000} \times 100 \tag{A.10}$$

$$\therefore \%I'_{sc,full-cell} = \frac{(2.3 - 3.7) \times 249.64}{10.152 \times 1000} \times 100 = -\mathbf{3.44}\ \% = \%I'_{sc,half\,cut\,cell} \tag{A.11}$$

A.3 Chapter 3

A.3.1 Computational comparison of different settings for angle dependent studies

This section presents a comparative study conducted using two different settings in the GenPro4 software for angle-dependent studies. The setting labeled as (S.nai) in GenPro4 represents the number of angular intervals used to calculate optical properties at different angles of incidence. In this thesis, two settings were simulated and compared, specifically focusing on the viola leaf petal texture with the upright microcone.

The interpretation of these settings is as follows: For example, if the setting is $S.nai = 18$, it means that 18 sectors are created, with each sector corresponding to a range of 5°. The setting named 'S.iai' denotes the incident light angular interval. If for instance, S.nai = 18 and S.iai = 1, it represents a range of angles from 0° to 5°. However, when S.nai = 90, each value of S.iai represents a single angle instead of a range. Nevertheless, this setting significantly increases computational time and is not ideal.

To compare the two settings, Table A.3 presents the results. The percentage values related to total stack reflectance (R) and absorptance in the absorber layer (A_{c-Si}) indicate

the root mean square error (RMSE), as clearly shown in the table. It can be observed that the maximum difference is only 0.5%. The last column displays the percentage difference in J_{ph} values obtained using the two different settings, which is not equivalent to the RMSE and represents a relative difference comparison. Even in this parameter, the maximum deviation is only 0.5

Therefore, considering the minimal deviation between the settings, the simulations were computed using the 'S.nai = 18' setting. Although the angles simulated represent ranges of 5°, they can be assumed to be singular angles due to the minimal observed deviations.

Table A.3: RMSE of the different setting used to compute angle dependent studies using GenPro4 for the viola leaf petals texture

AOI	R (%)	Absorptance in c-Si (%)	J_{ph} (%)
0	0.49	0.35	0.06
10	0.49	0.35	0.09
20	0.49	0.35	0.17
30	0.49	0.35	0.36
40	0.49	0.35	0.53
50	0.49	0.35	0.50
60	0.49	0.35	0.45
70	0.49	0.35	0.00
80	0.49	0.35	0.23
90	0.49	0.36	0.71

References

[1] NASA. In depth | sun – nasa solar system exploration, 2021.

[2] V. G. Belessiotis and E. Papanicolaou. History of solar energy. In *Comprehensive Renewable Energy*, volume 3, pages 85–102. Elsevier Ltd, 2012.

[3] Jérôme Fatet. Recreating Edmond Becquerel's electrochemical actinometer. Technical report, 2006.

[4] Willoughby Smith. Effect of Light on Selenium During the Passage of An Electric Current. *Nature*, 7, 1873.

[5] P. M. Harman and C. Stewart Gillmor. The Scientific Letters and Papers of James Clerk Maxwell . *American Journal of Physics*, 60(4):382–383, 4 1992.

[6] C.E Fritts. On the fritts selenium cells and batteries. *Journal of the Franklin Institute*, 119(3), 1885.

[7] D. M. Chapin, C. S. Fuller, and G. L. Pearson. A new silicon p-n junction photocell for converting solar radiation into electrical power [3], 1954.

[8] Sayan Kumar Nag, Tarun Kumar Gangopadhyay, and John Paserba. Solar Photovoltaics: A Brief History of Technologies [History]. *IEEE Power and Energy Magazine*, 20(3):77–85, 2022.

[9] A Catalano, R V D'Aiello, J Dresner, B Faughnan, A Firester, J Kane, H Schade, G Schwartz, and A Triano. Attainment of 10% conversion efficiency in amorphous silicon solar cells. In *Conference: 16. IEEE photovoltaics specialists conference, San Diego, CA, USA, 28 Sep 1982*, 1982.

[10] Xing He, Yuta Iwamoto, Toshiro Kaneko, and Toshiaki Kato. Fabrication of near-invisible solar cell with monolayer WS2. *Scientific Reports*, 12(1), 12 2022.

[11] Cesare Silvi. History and future of renewable solar energy. *Development*, 51(3):409–414, 2008.

[12] World Energy Outlook 2022 – Analysis - IEA.

[13] Ao Wang and Yimin Xuan. A detailed study on loss processes in solar cells. *Energy*, 144:490–500, 2 2018.

[14] Ross McCluney. Radiometry and Photometry. *Encyclopedia of Physical Science and Technology*, pages 731–758, 1 2003.

[15] Greenland Ice Sheet. *Nature*, 145(3665):265–321, 1 2021.

[16] D. E. Aspnes and A. A. Studna. Dielectric functions and optical parameters of si, ge, gap, gaas, gasb, inp, inas, and insb from 1.5 to 6.0 ev. *Physical Review B*, 27:985–1009, 1983.

[17] R. Vismara. *Advanced Light Management in Thin-Film Solar Cells*. PhD thesis, Delft University of Technology, Delft, 2020.

[18] Eli Yablonovitch. Statistical ray optics. *JOSA, Vol. 72, Issue 7, pp. 899-907*, 72(7):899–907, 7 1982.

[19] Ecoprogetti. The structure of a photovoltaic module - ecoprogetti - specialist in photovoltaic production process, 2014.

[20] Solarge. Solarge | lightweight pv modules, fast installation and 100recycable, 2023.

[21] F Senel Boydag, Shaval V Mamedov, Vilayet A Alekperov, and Gulcin Kandemir. A study of the optical properties of polypropylene based polymer composite films. Technical report.

[22] F. Ş Boydağ, Sh V. Mamedov, V. A. Alekperov, and Y. Lenger Özcanli. Optical Characterization of Weakly Absorbing PP, PE, and PP/PE Films. *Optics and Spectroscopy (English translation of Optika i Spektroskopiya)*, 95(2):225–229, 8 2003.

[23] D. Akbar and H. Altan. Characterization of polypropylene treated under dual-RF plasma using terahertz time-domain spectroscopy. *Journal of Materials Science*, 48(23):8209–8214, 12 2013.

[24] Vaishali Bhavsar and Deepti Tripathi. Study of refractive index dispersion and optical conductivity of PPy doped PVC films. Technical report, 2016.

[25] E. Manias, A. Touny, L. Wu, K. Strawhecker, B. Lu, and T. C. Chung. Polypropylene/montmorillonite nanocomposites. Review of the synthetic routes and materials properties. *Chemistry of Materials*, 13(10):3516–3523, 2001.

[26] A. N. Sprafke and R. B. Wehrspohn. Light trapping concepts for photon management in solar cells, 2012.

[27] Zheng Tang, Wolfgang Tress, and Olle Inganäs. Light trapping in thin film organic solar cells. *Materials Today*, 17(8):389–396, 10 2014.

[28] Raju Lampande, Gyeong Woo Kim, Mi Jin Park, Byeong Yeob Kang, and Jang Hyuk Kwon. Efficient light harvesting in inverted polymer solar cells using polymeric 2D-microstructures. *Solar Energy Materials and Solar Cells*, 151:162–168, 7 2016.

[29] Benjamin Lipovsek, Janez Krc, and Marko Topic. Microtextured Light-Management Foils and Their Optimization for Planar Organic and Perovskite Solar Cells. *IEEE Journal of Photovoltaics*, 8(3):783–792, 5 2018.

[30] Rebecca Saive. Light trapping in thin silicon solar cells: A review on fundamentals and technologies. *Progress in Photovoltaics: Research and Applications*, 29(10):1125–1137, 10 2021.

[31] Raúl J. Martín-Palma and Akhlesh Lakhtakia. Progress on bioinspired, biomimetic, and bioreplication routes to harvest solar energy, 6 2017.

[32] Elisavet Tatsi and Gianmarco Griffini. Polymeric materials for photon management in photovoltaics. *Solar Energy Materials and Solar Cells*, 196:43–56, 7 2019.

[33] Min Su Kim, · Ju, Heon Lee, · Moon, and Kyu Kwak. Review: Surface Texturing Methods for Solar Cell Efficiency Enhancement. *International Journal of Precision Engineering and Manufacturing*, 21:1389–1398, 2020.

[34] Najiba Soudi, Sama Nanayakkara, Navid M.S. Jahed, and Sheva Naahidi. Rise of nature-inspired solar photovoltaic energy convertors, 9 2020.

[35] S. A. Boden and D. M. Bagnall. Bio-mimetic subwavelength surfaces for near-zero reflection sunrise to sunset. *Conference Record of the 2006 IEEE 4th World Conference on Photovoltaic Energy Conversion, WCPEC-4*, 2:1358–1361, 2006.

[36] Danbi Yoo, Siddhartha Garud, Cham T. Trinh, Daniel Amkreutz, and Christiane Becker. Lotus Leaf Structured Fluoropolymer Foils for Superhydrophobicity and Enhanced Light Management in Photovoltaic Devices. *IEEE Journal of Photovoltaics*, 12(1):97–106, 1 2022.

[37] Daniela Dirnberger, Björn Müller, and Christian Reise. PV module energy rating: Opportunities and limitations. *Progress in Photovoltaics: Research and Applications*, 23(12):1754–1770, 12 2015.

[38] Ino Geisemeyer, Nico Tucher, Bjorn Muller, Heiko Steinkemper, Jochen Hohl-Ebinger, Martin C. Schubert, and Wilhelm Warta. Angle dependence of solar cells and modules: The role of cell texturization. *IEEE Journal of Photovoltaics*, 7(1):19–24, 1 2017.

[39] Tudor E. Scheul, Edris Khorani, Tasmiat Rahman, Martin D.B. Charlton, and Stuart A. Boden. Wavelength and angle resolved reflectance measurements of pyramidal textures for crystalline silicon photovoltaics. *Progress in Photovoltaics: Research and Applications*, 28(12):1248–1257, 12 2020.

[40] Aiman Roslizar, Stephan Dottermusch, Raphael Schmager, Markus Guttmann, Guillaume Gomard, Hendrik Hölscher, Bryce S. Richards, and Ulrich W. Paetzold. Hot-embossed microcone-textured fluoropolymer as self-cleaning and anti-reflective photovoltaic module covers. *Solar Energy Materials and Solar Cells*, 214, 8 2020.

[41] Nizamudeen Cherupurakal, Mohammad Sayem Mozumder, Abdel Hamid I. Mourad, and Shubra Lalwani. Recent advances in superhydrophobic polymers for antireflective self-cleaning solar panels, 11 2021.

[42] Haneen Abuzaid, Mahmoud Awad, and Abdulrahim Shamayleh. Impact of dust accumulation on photovoltaic panels: a review paper. *International Journal of Sustainable Engineering*, 15(1):266–287, 12 2022.

[43] Meena Laad and Babaji Ghule. Fabrication Techniques of Superhydrophobic Coatings: A Comprehensive Review, 8 2022.

[44] Khosrow Maghsoudi, Elham Vazirinasab, Gelareh Momen, and Reza Jafari. Advances in the Fabrication of Superhydrophobic Polymeric Surfaces by Polymer Molding Processes. *Industrial and Engineering Chemistry Research*, 59(20):9343–9363, 5 2020.

[45] Marko Parikka, Jari Lautanen, Jani Tervo, Markku Kuittinen, Terho Kaikuranta, Jari Turunen, Pasi Laakkonen, and Marko Honkanen. Deterministic diffractive diffusers for displays. *Applied Optics, Vol. 40, Issue 14, pp. 2239-2246*, 40(14):2239–2246, 5 2001.

[46] Teng Kai Shih, Chia Fu Chen, Jeng Rong Ho, and Fang Tzu Chuang. Fabrication of PDMS (polydimethylsiloxane) microlens and diffuser using replica molding. *Microelectronic Engineering*, 83(11-12):2499–2503, 11 2006.

[47] Jian-Ren Ciou, Sen-Yeu Yang, Tzu-Chien Huang, Po-Hsun Huang, and Kuo-Huang Hsieh. Fast fabrication of integrated surface-relief and particle-diffusing plastic diffuser by use of a hybrid extrusion roller embossing process. *Optics Express, Vol. 16, Issue 1, pp. 440-447*, 16(1):440–447, 1 2008.

[48] Héctor M. Escamilla, E. Efrén García-Guerrero, Tamara A. Leskova, Eugenio R. Méndez, Andrei V. Shchegrov, and Alexei A. Maradudin. Photofabrication of random achromatic optical diffusers for uniform illumination. *Applied Optics, Vol. 40, Issue 7, pp. 1098-1108*, 40(7):1098–1108, 3 2001.

[49] Marina A. González Lazo, Rémy Teuscher, Yves Leterrier, Jan Anders E. Månson, Caroline Calderone, Aïcha Hessler-Wyser, Philippe Couty, Yvan Ziegler, and Diego Fischer. UV-nanoimprint lithography and large area roll-to-roll texturization with hyperbranched polymer nanocomposites for light-trapping applications. *Solar Energy Materials and Solar Cells*, 103:147–156, 8 2012.

[50] Sun Jingyao, Wu Daming, Liu Ying, Yang Zhenzhou, and Gou Pengsheng. Rapid fabrication of micro structure on polypropylene by plate to plate isothermal hot embossing method. *Polymer Engineering and Science*, 58(6):952–960, 6 2018.

[51] Thomas E. Kimerling, Weidan Liu, Byung H. Kim, and Donggang Yao. Rapid hot embossing of polymer microfeatures. *Microsystem Technologies*, 12(8):730–735, 7 2006.

[52] Liang-Ting Jiang, Tzu-Chien Huang, Chien-Ren Chiu, Chih-Yuan Chang, and Sen-Yeu Yang. Fabrication of plastic microlens arrays using hybrid extrusion rolling embossing with a metallic cylinder mold fabricated using dry film resist. Technical report, 2007.

[53] Shih Jung Liu, Yu Chin Huang, Sen Yeu Yang, and Kuo Huang Hsieh. Rapid fabrication of surface-relief plastic diffusers by ultrasonic embossing. *Optics and Laser Technology*, 42(5):794–798, 7 2010.

[54] Dan Xie, Honghai Zhang, Xiayun Shu, and Junfeng Xiao. Fabrication of polymer microlens array with pneumatically diaphragm-driven drop-on-demand inkjet technology. Technical report, 2012.

[55] Heon Lee, Sunghoon Hong, Kiyeon Yang, and Kyungwoo Choi. Fabrication of nanosized resist patterns on flexible plastic film using thermal curing nano-imprint lithography. *Microelectronic Engineering*, 83(2):323–327, 2 2006.

[56] Kang Soo Han, Ju Hyeon Shin, Woo Young Yoon, and Heon Lee. Enhanced performance of solar cells with anti-reflection layer fabricated by nano-imprint lithography. In *Solar Energy Materials and Solar Cells*, volume 95, pages 288–291, 1 2011.

[57] Ho Jun Jeon, Carl G. Simon, and Geun Hyung Kim. A mini-review: Cell response to microscale, nanoscale, and hierarchical patterning of surface structure, 10 2014.

[58] Joongon Son and Geunhyung Kim. Three-Dimensional Plotter Technology for Fabricating Polymeric Scaffolds with Micro-grooved Surfaces. *http://dx.doi.org/10.1163/156856208X399954*, 20(14):2089–2101, 10 2012.

[59] A. Pruna, J. Ramiro, and L. Belforte. Preliminary study on different technological tools and polymeric materials towards superhydrophobic surfaces for automotive applications. *Journal of Physics and Chemistry of Solids*, 74(11):1640–1645, 11 2013.

[60] ASTM. Standard guide for determination of thickness of plastic film test specimens, 2021.

[61] W. Theiss. Scout technical manual, 2012.

[62] Rudi Santbergen, Tomomi Meguro, Takashi Suezaki, Gensuke Koizumi, Kenji Yamamoto, and Miro Zeman. Genpro4 optical model for solar cell simulation and its application to multijunction solar cells. *IEEE Journal of Photovoltaics*, 7:919–926, 5 2017.

[63] J.A. Woollam. J.a. woollam ellipsometry, 2023.

[64] Asma Shamim, Muhammad Noman, Muhammad Zubair, Adnan Daud Khan, and Saim Saher. A facile approach to determine the unknown refractive index (n) and extinction coefficient (k) of novel encapsulant materials used in back contact pv modules. *Applied Physics A: Materials Science and Processing*, 124:1–6, 8 2018.

[65] Indra Subedi, Timothy J. Silverman, Michael G. Deceglie, and Nikolas J. Podraza. PERC silicon PV infrared to ultraviolet optical model. *Solar Energy Materials and Solar Cells*, 215:110655, 9 2020.

[66] Simeon C. Baker-Finch, Keith R. McIntosh, Di Yan, Kean Chern Fong, and Teng C. Kho. Near-infrared free carrier absorption in heavily doped silicon. *Journal of Applied Physics*, 116(6), 8 2014.

[67] Fraunhofer ISE. SmartCalc.CTM - Powerful Cell-To-Module Analysis, 2023.

[68] John A. Duffie and William A. Beckman. *Solar Engineering of Thermal Processes*. John Wiley & Sons, Inc., Hoboken, NJ, USA, 4 2013.

[69] Nils Reiners, Ulf Blieske, and Susanne Siebentritt. Investigation on the angle and spectral dependence of the internal and the external quantum efficiency of crystalline silicon solar cells and modules. *IEEE Journal of Photovoltaics*, 8(6):1738–1747, 11 2018.

[70] Danbi Yoo, Siddhartha Garud, Cham T. Trinh, Daniel Amkreutz, and Christiane Becker. Lotus leaf structured fluoropolymer foils for superhydrophobicity and enhanced light management in photovoltaic devices. *IEEE Journal of Photovoltaics*, 12:97–106, 1 2022.

[71] Zhiwu Han, Zhibin Jiao, Shichao Niu, and Luquan Ren. Ascendant bioinspired antireflective materials: Opportunities and challenges coexist, 6 2019.

[72] R ; Meguro, T ; Suezaki, T ; Koizumi, G ; Yamamoto, and K Zeman. Genpro4 optical model for solar cell simulation and its application to multijunction solar cells. *IEEE Journal of Photovoltaics*, 7:919, 2017.

[73] Stephan Dottermusch, Raphael Schmager, Efthymios Klampaftis, Stefan Paetel, Oliver Kiowski, Kaining Ding, Bryce S. Richards, and Ulrich W. Paetzold. Micro-cone textures for improved light in-coupling and retroreflection-inspired light trapping at the front surface of solar modules. *Progress in Photovoltaics: Research and Applications*, 27:593–602, 7 2019.

[74] Aiman Roslizar, Stephan Dottermusch, Raphael Schmager, Markus Guttmann, Guillaume Gomard, Hendrik Hölscher, Bryce S. Richards, and Ulrich W. Paetzold. Hot-embossed microcone-textured fluoropolymer as self-cleaning and anti-reflective photovoltaic module covers. *Solar Energy Materials and Solar Cells*, 214:110582, 8 2020.

[75] Noboru Yamada, Oanh Ngo Kim, Toru Tokimitsu, Yusuke Nakai, and Hideki Masuda. Optimization of anti-reflection moth-eye structures for use in crystalline silicon solar cells. *Progress in Photovoltaics: Research and Applications*, 19:134–140, 3 2011.

[76] Shuping Xie, Xinjun Wan, Bo Yang, Wei Zhang, Xiaoxiao Wei, and Songlin Zhuang. Design and fabrication of wafer-level microlens array with moth-eye antireflective nanostructures. *Nanomaterials 2019, Vol. 9, Page 747*, 9:747, 5 2019.

[77] Kan Li, Rengmao Wu, Yi Ruan, Liuqing Zhang, and Hongyu Zhen. Numerical analysis of the angular insensitive photovoltaic light harvesting with the biomimetic scattering film inspired by the rose petal epidermal topography. *Solar Energy*, 170:800–806, 8 2018.

[78] Carolin Ulbrich, Andreas Gerber, Ko Hermans, Andreas Lambertz, and Uwe Rau. Analysis of short circuit current gains by an anti-reflective textured cover on silicon thin film solar cells. *Progress in Photovoltaics: Research and Applications*, 21:1672–1681, 12 2013.

[79] Serkan Esiner, Tom Bus, Martijn M. Wienk, Ko Hermans, and René A.J. Janssen. Quantification and validation of the efficiency enhancement reached by application of a retroreflective light trapping texture on a polymer solar cell. *Advanced Energy Materials*, 3:1013–1017, 8 2013.

[80] Gil Shalev, Sebastian W. Schmitt, Heidemarie Embrechts, Gerald Brönstrup, and Silke Christiansen. Enhanced photovoltaics inspired by the fovea centralis. *Scientific Reports 2015 5:1*, 5:1–7, 2 2015.

[81] Abdulwahab Alasfour, Zhengshan J. Yu, William Weigand, David Quispe, and Zachary C. Holman. Sub-micrometer random-pyramid texturing of silicon solar wafers with excellent surface passivation and low reflectance. *Solar Energy Materials and Solar Cells*, 218:110761, 12 2020.

[82] Nico Tucher, Björn Müller, Peter Jakob, Johannes Eisenlohr, Oliver Höhn, Hubert Hauser, Jan Christoph Goldschmidt, Martin Hermle, and Benedikt Bläsi. Optical performance of the honeycomb texture – a cell and module level analysis using the optos formalism. *Solar Energy Materials and Solar Cells*, 173:66–71, 2017.

[83] Brittany L Smith, Michael Woodhouse, Kelsey A W Horowitz, Timothy J Silverman, Jarett Zuboy, and Robert M Margolis. Photovoltaic (pv) module technologies: 2020 benchmark costs and technology evolution framework results. 2020.

[84] InfoLink Consulting. Spot price, https://www.infolink-group.com/spot-price/.

Acknowledgments

I am filled with immense happiness as I take a moment to acknowledge and express my deepest gratitude to the remarkable individuals who have provided unwavering support at various junctions of my master's journey.

First and foremost, I want to extend my heartfelt appreciation to Prof. T R Seetharam. Your guidance, teachings, and unwavering belief in me have been invaluable. It is because of your recommendation and support that I stand here today, pursuing my master's. Every conversation with you has been enlightening, and your unique perspectives have shaped my understanding of scientific research. Thank you for everything, from my bachelor's to my master's - your mentorship has been a true blessing.

During the course of my master's thesis, there were three influential people who played a pivotal role: Dr. ir. Rudi Santbergen, Menno Van Den Donker, and Lukas Simurka. I am profoundly grateful for their exceptional mentorship. Prof. Rudi, our conversations have always yielded positive outcomes, strengthening the trajectory of this thesis. Your academic and moral support have been truly remarkable, and I express my sincere thanks for believing in me. Menno and Lukas, I cannot thank you enough for granting me the freedom to explore multiple ideas, even when some didn't work out as planned. Your unwavering support has been instrumental in achieving the results I have today.

To the Solarge team, Jeroen, Natalia, Kristof, I extend my heartfelt thanks for your immense help throughout my eight-month thesis.

To the TU Delft team, Stefaan, Yilong, Federica, and Bernardus, I would like to thank you for all the help and support you have provided during the course of my thesis. Your support and insights have been invaluable in shaping the outcome of my research. The collaborative discussions have led to the right results, and I am grateful for the opportunity to work with such a talented and supportive team.

I would like to dedicate a special mention to my dear friend Alonzo, who I often refer to as the "disappointing friend". Alonzo, I want to express my sincere gratitude for being a true friend and confidant throughout this entire journey. Your presence has been a source of comfort and support during those moments when I needed someone to talk to and vent my frustrations. Your patience in listening to me and offering a sympathetic ear is truly appreciated. Our weekly three-hour journeys to Weert have been filled with laughter, memorable conversations, and shared experiences. I genuinely value the friendship we have cultivated over these months, and I am hopeful that our bond will continue to grow stronger in the years to come. Thank you for being an integral part of my journey and for

your unwavering friendship.

I would like to express my heartfelt gratitude to my roommates, Sanky and Ayman. Living together with both of you has been a source of joy and laughter throughout this journey. Our conversations have covered a wide range of topics, providing much-needed moments of relaxation and taking my mind off the thesis when I needed it the most. Sanky, I want to give you a special thanks for lending me your laptop during a crucial time in my thesis. Your generosity and support were truly invaluable, and I sincerely appreciate it.

Jeeju, I cannot express my gratitude enough for your unwavering support and guidance over the past two years. Every conversation with you instills a sense of positivity and confidence within me. Your unwavering support, regardless of the circumstances, means the world to me. I may sometimes bother you with too many questions, but your patience and guidance have been a source of strength for me. Thank you for always being there for me.

No acknowledgement would be complete without mentioning my incredible mom and dad. Your hard work, sincerity, and dedication are the very reasons I am able to write this thesis today. You have never stopped me from following my dreams and passions, and I am forever grateful for your constant support. Although I may have spoken to you less since I came to the Netherlands for my master's, please know that I have thought of both of you every minute of the day. I dedicate this thesis to you, as it would not have been possible without your unwavering belief in me.

Finally, I express my deepest gratitude to God. My prayers may sometimes sound like a child's pleas to their parents, but your presence has always been a source of solace and strength. Your guidance and blessings have been with me throughout this journey, and I will continue to place my faith in you. "OM SAI RAM".

Sathya
Delft, July 2023